

Characterization of non-trivial spin texture and  
anomalous electronic transport properties in  
Mn-based Heusler systems

*By*

Sk Jamaluddin

Enrolment No: PHYS11201804003

National Institute of Science Education and Research,  
Bhubaneswar

*A thesis submitted to the  
Board of Studies in Physical Sciences*

*In partial fulfillment of requirements  
for the Degree of*

DOCTOR OF PHILOSOPHY

*of*

HOMI BHABHA NATIONAL INSTITUTE



September, 2023

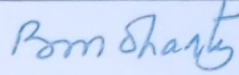


# Homi Bhabha National Institute<sup>1</sup>

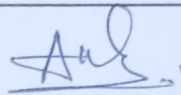
## Recommendations of the Viva Voce Committee

As members of the Viva Voce Committee, we certify that we have read the dissertation prepared by Sk Jamaluddin entitled "*Characterization of non-trivial spin texture and anomalous electronic transport properties in Mn-based Heusler systems*" and recommend that it may be accepted as fulfilling the thesis requirement for the award of Degree of Doctor of Philosophy.

Chairman – Prof. Bedangadas Mohanty



Guide / Convener – Dr. Ajaya Kumar Nayak



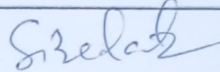
Co-guide -

Examiner – Prof. Sunil Nair

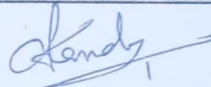


Digitally signed by Sunil Nair  
DN: cn=Sunil Nair, o=IISER Pune, ou=Physics,  
email=sunil@iiserpune.ac.in, c=IN  
Date: 2024.02.12 16:36:38 +05'30'

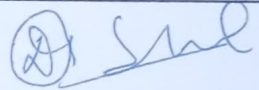
Member 1- Prof. Subhankar Bedanta



Member 2- Dr. Ashis Kumar Nandy



Member 3- Dr. Debakanta Samal



Final approval and acceptance of this thesis is contingent upon the candidate's submission of the final copies of the thesis to HBNI.

I/We hereby certify that I/we have read this thesis prepared under my/our direction and recommend that it may be accepted as fulfilling the thesis requirement.

Date: 12/02/2024

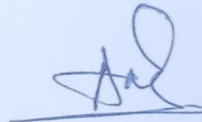
Place: NISER

Signature

Co-guide (if any)

Signature

Guide



<sup>1</sup>This page is to be included only for final submission after successful completion of viva voce.

## STATEMENT BY AUTHOR

This dissertation has been submitted in partial fulfillment of requirements for an advanced degree at Homi Bhabha National Institute (HBNI) and is deposited in the Library to be made available to borrowers under rules of the HBNI.

Brief quotations from this dissertation are allowable without special permission, provided that accurate acknowledgement of source is made. Requests for permission for extended quotation from or reproduction of this manuscript in whole or in part may be granted by the Competent Authority of HBNI when in his or her judgment the proposed use of the material is in the interests of scholarship. In all other instances, however, permission must be obtained from the author.

Sk Jamaluddin  
12.02.2024

Sk Jamaluddin

## DECLARATION

I, hereby declare that the investigation presented in the thesis has been carried out by me. The work is original and has not been submitted earlier as a whole or in part for a degree / diploma at this or any other Institution / University.

Sk Jamaluddin

12.02.2024

Sk Jamaluddin

## CERTIFICATION ON ACADEMIC INTEGRITY

1. I **Sk Jamaluddin**, HBNI Enrolment No. **PHYS11201804003**, hereby undertake that the Thesis, titled "*Characterization of non-trivial spin texture and anomalous electronic transport properties in Mn-based Heusler systems*" is prepared by me and is the original work undertaken by me and free of any plagiarism. That the document has been duly checked through a plagiarism detection tool and the document is plagiarism free.

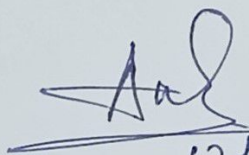
3. I am aware and undertake that if plagiarism is detected in my thesis at any stage in the future, suitable penalty will be imposed as applicable as per the guidelines of the Institute/UGC.

Sk Jamaluddin  
12/02/24

Signature of the Student with date

**Endorsed by the Thesis Supervisor:**

I certify that the thesis written by the Researcher is plagiarism free as mentioned above by the student.

  
12/02/2024

Signature of the Thesis Supervisor with date

Name: Dr. Ajaya Kumar Nayak

Designation: Associate Professor

Department/ Centre: School of Physical Sciences

Name of the CI/ OCC: National Institute of Science Education and Research, Bhubaneswar



## List of Publications arising from the thesis

### Journal

#### • Published

1. “Robust Antiskyrmion Phase in Bulk Tetragonal Mn–Pt(Pd)–Sn Heusler System Probed by Magnetic Entropy Change and AC-Susceptibility Measurements”  
**Sk Jamaluddin**, Subhendu K. Manna, Bimalesh Giri, P. V. Prakash Madduri, Stuart S. P. Parkin, and Ajaya K. Nayak, *Adv. Funct. Mater.* **29**, 1901776 (2019).
2. “Extrinsic to intrinsic mechanism crossover of anomalous Hall effect in the Ir-doped MnPtSn Heusler system”,  
**Sk Jamaluddin**, Roumita Roy, Amitabh Das, Sudipta Kanungo, and Ajaya K. Nayak, *Phys. Rev. B* **106**, 184424 (2022).
3. “Decoupling topological antiskyrmion and non-topological magnetic phases in  $D_{2d}$  symmetric Mn–Ni–Ga single crystalline device”  
**Sk Jamaluddin**, Subir Sen, Dola Chakrabartty, and Ajaya K. Nayak”, *Appl. Phys. Lett.* **123**, 192404 (2023).

### Conferences

1. Poster presentation at Annual Conference on QUANTUM CONDENSED MATTER (QMAT)-2023, National Institute of Science Education and Research (NISER), Bhubaneswar, India.
2. Poster presentation at International Conference on Strongly Correlated Electron Systems (SCES)-2023, Incheon, South Korea.
3. Oral presentation at Frontiers in Materials for Technological Applications (FIMTA)-2022, Institute of Minerals and Materials Technology (IMMT), Bhubaneswar, India.
4. Poster presentation at “Symposium on Magnetism and Spintronics (SMS)-2021, National Institute of Science Education and Research (NISER), Bhubaneswar, India.
5. Poster presentation at Bring the Nano World Together (BTNT)-2019, National Institute of Science Education and Research (NISER), Bhubaneswar, India.
6. Poster presentation at International Conference on Magnetic Materials and Applications (ICMAGMA)-2018, National Institute of Science Education and Research (NISER), Bhubaneswar.

- Other Publications

1. "Tunable room temperature magnetic skyrmions in centrosymmetric kagome magnet  $Mn_4Ga_2Sn$ ",  
Dola Chakrabartty, **Sk Jamaluddin**, Subhendu K. Manna and Ajaya K. Nayak, Communications Physics **5**, 189 (2022).

- Submitted to arXiv

1. "Higher order exchange driven noncoplanar magnetic state and large anomalous Hall effects in electron doped kagome magnet  $Mn_3Sn$ ",  
Charanpreet Singh, **Sk Jamaluddin**, Ashis K. Nandy, Masashi Tokunaga, Maxim Avdeev, and Ajaya K. Nayak, arXiv:2211.12722.
2. "Spin order dependent skyrmion stabilization in MnFeCoGe hexagonal magnets",  
Dola Chakrabartty, Mihir Sahoo, Amit Kumar, **Sk Jamaluddin**, Bimalesh Giri, Hitesh Chhabra, Kalpataru Pradhan, and Ajaya K Nayak, arXiv:2311.15823."

Sk Jamaluddin

12.02.2024

Sk Jamaluddin

# DEDICATIONS

*Dedicated to*

My

Parents

Sk Samsuddin

Nasiba Bibi

.....

My Wife

Mehejabin Khatun

## ACKNOWLEDGEMENTS

First, I would like to express my gratitude to my supervisor Dr. Ajaya Kumar Nayak to give me the opportunity to work in this field. I am thankful for his guidance, valuable suggestions and constant encouragement during my Ph.D tenure. His continuous observations and support are of immense help to me. I am deeply thankful to him for his valuable input and guidance in improving my knowledge. I also thank him for the amount of time he has spent for me during the work.

I would like to thank the chairman of my thesis monitoring committee Prof. Bedangadas Mohanty, for his continuous encouragement, suggestions, and evaluation of my work. His comments during the annual evaluation seminar always inspired me to combine fundamental knowledge with the practical aspect. I would also like to thank other doctoral committee members, Prof. Subhankar Bedanta and Dr. Ashis Kumar Nandy, for the continuous evaluation and suggestion throughout my Ph.D work. I want to thank Dr. Debakanta Samal from IOP Bhubaneswar for evaluating of my work as an external doctoral committee member. Their inquiries and doubts prompted me to learn more about the subject, which invariably improved my understanding of the topic.

I also thank to School Of Physical Sciences and Center for Interdisciplinary Science (CIS), NISER for providing me with all the necessary facilities and academic environment required for the work.

I am immensely grateful to Dr. Sudipta Kanungo faculty of IIT Goa and his Ph.D student Roumita Roy for their support in theoretical calculations. I would also like to thank Dr. Amitabh Das from BARC, Mumbai for carrying out the Neutron diffraction measurements.

I am very thankful to my lab members Dr. Shubendu Kumar Manna, Dr. Charanpreet Singh, Dr. Subir Sen, Dr. Bimalesh Giri and Dola Chakrabarty for their unconditional help during the experiments and discussions. I wish to thank my friends, Tanim Firdoshi, Rashmi Rekha Sahoo, Sujit Garain, Anupa Kumari, and Prabhakar for their support in my academic as well as in my personal life.

I acknowledge the financial support provided by NISER during my Ph.D.

I am very grateful to my grandmother, parents, and family members for their blessing, moral support, unconditional love, and sacrifice, which gave me the strength to complete my Ph.D.

# Contents

<b>Title page</b>	<b>i</b>
<b>SUMMARY</b>	<b>xiv</b>
<b>List of Figures</b>	<b>xx</b>
<b>1 Introduction</b>	<b>3</b>
1.1 Fundamental magnetic interactions . . . . .	5
1.1.1 Exchange interaction . . . . .	5
1.1.2 Dzyaloshinskii - Moriya interaction (DMI) . . . . .	6
1.1.3 Magnetic anisotropy . . . . .	8
1.1.4 Dipolar interaction . . . . .	9
1.1.5 Zeeman energy . . . . .	10
1.2 Non-collinear spin texture . . . . .	10
1.3 Magnetic Skyrmions . . . . .	12
1.3.1 Stabilization mechanism of different topologically equivalent Skyrmionic textures . . . . .	14
1.4 Experimental observation of Skyrmion/Antiskyrmion . . . . .	16
1.4.1 Observation of Skyrmion . . . . .	16
1.4.2 Observation of Antiskyrmion . . . . .	20
1.5 Magnetocaloric effect . . . . .	21
1.6 Electronic transport properties in magnetic systems . . . . .	24
1.6.1 Anomalous Hall effect . . . . .	25

1.6.2	Topological Hall effect . . . . .	33
1.7	Heusler compounds . . . . .	37
1.7.1	Structural properties . . . . .	38
1.7.2	Magnetic properties of Heusler compounds . . . . .	41
1.7.3	Heusler compounds in Spintronics . . . . .	43
1.8	Outline of the Thesis . . . . .	44
<b>2</b>	<b>Experimental techniques</b>	<b>45</b>
2.1	Sample preparation . . . . .	45
2.2	Structural characterizations . . . . .	47
2.2.1	X-ray Diffraction (XRD) . . . . .	47
2.2.2	Scanning Electron Microscopy (SEM) . . . . .	48
2.2.3	Transmission Electron Microscopy (TEM) . . . . .	49
2.3	Magnetic characterizations . . . . .	50
2.3.1	Vibrating Sample Magnetometer (VSM) . . . . .	51
2.3.2	Superconducting Quantum Interference Device (SQUID) . . . . .	51
2.3.3	AC Susceptibility measurement . . . . .	52
2.3.4	Neutron Diffraction . . . . .	54
2.4	Site-specific device and TEM sample fabrication . . . . .	54
2.4.1	Electron Backscatter Diffraction (EBSD) . . . . .	55
2.4.2	Focused Ion Beam (FIB) . . . . .	56
2.4.3	Electron Beam Lithography (EBL) . . . . .	61
2.5	Electronic transport measurements . . . . .	62
<b>3</b>	<b>Antiskyrmion phase in Mn-Pt-Sn Heusler alloy</b>	<b>65</b>
3.1	Sample preparation . . . . .	66
3.2	Characterizations . . . . .	66
3.2.1	Structural characterization (XRD) . . . . .	66
3.2.2	SEM and EDS studies . . . . .	68
3.2.3	Magnetic characterizations . . . . .	68
3.3	Magnetic entropy measurements . . . . .	72

---

3.4	AC Susceptibility study . . . . .	74
3.5	Phase diagram of Antiskyrmion state . . . . .	77
3.6	Summary . . . . .	78
<b>4</b>	<b>Antiskyrmion phase in Mn-Ni-Ga Heusler alloy</b>	<b>81</b>
4.1	Structural and magnetic properties of $\text{Mn}_{2+x}\text{Ni}_{1-x}\text{Ga}$ . . . . .	82
4.2	Geometry of Hall devices . . . . .	84
4.3	Longitudinal resistivity of out-of-plane and in-plane devices . . . . .	86
4.4	Topological Hall effect in the out-of-plane orientation . . . . .	88
4.5	Hall resistivity in the in-plane Hall device geometry . . . . .	92
4.6	Reproducibility of the experimental results . . . . .	100
4.7	Micromagnetic simulations . . . . .	102
4.8	Summary . . . . .	103
<b>5</b>	<b>Anomalous Hall effect in Mn-Pt-Sn Heusler alloy</b>	<b>105</b>
5.1	Sample preparation . . . . .	107
5.2	Characterizations . . . . .	107
5.2.1	Structural and compositional characterization . . . . .	107
5.2.2	Magnetic studies . . . . .	109
5.2.3	Neutron diffraction study . . . . .	113
5.3	Electronic transport properties . . . . .	117
5.3.1	Hall resistivity . . . . .	118
5.3.2	Scaling of anomalous Hall effect . . . . .	118
5.4	Summary . . . . .	125
<b>6</b>	<b>Summary and Future Aspects</b>	<b>127</b>

## SUMMARY

The development of futuristic spintronics devices depends on the understanding of the collective phenomena of spins, their correlation with the conduction electrons, and their evolution under external perturbations. In recent times, the two most intriguing phenomena, (1) non-trivial topological spin texture and (2) anomalous electronic transport properties, have shown promising potential toward the realization of modern spintronics devices. In particular, the non-trivial spin textures magnetic skyrmions/antiskyrmions are proposed to be the building blocks in high-density data storage devices, quantum computing, neuromorphic computation, and logic devices. On the other hand, the Hall effect phenomenon is the electrical footprint of the distinct magnetic state, which has its own role in integrated spintronics devices.

The objective of this work is the characterization of non-trivial spin textures, such as magnetic antiskyrmions and studies on the anomalous electronic transport properties in Mn-based Heusler materials. The use of Mn-based Heusler alloy is advantageous in the sense that these compounds show rich magnetic and electronic phenomena, including high Curie temperature with tunable magnetic properties, large spin-orbit coupling, diverse electronic properties, and recently discovered non-collinear magnetic state. All these distinct properties of Mn-based Heusler compounds makes them an excellent platform for studying different magnetic phenomena.

In the first part of the thesis, the thermal and magnetic responses of antiskyrmions are used to map the antiskyrmion phase in a bulk Heusler alloy. Polycrystalline samples  $\text{Mn}_{1.4}\text{PtSn}$ ,  $\text{Mn}_{1.4}\text{Pt}_{0.9}\text{Pd}_{0.1}\text{Sn}$ , and  $\text{Mn}_{1.1}\text{PtSn}$  are synthesized using an arc-melt furnace. The Rietveld refinement of the powder XRD patterns confirms the phase purity of all the samples. The  $\text{Mn}_{1.4}\text{PtSn}$ , and  $\text{Mn}_{1.4}\text{Pt}_{0.9}\text{Pd}_{0.1}\text{Sn}$

crystallize in the tetragonal structure, whereas,  $\text{Mn}_{1.1}\text{PtSn}$  crystallizes in a cubic structure. It is worth mentioning that the tetragonal crystal structure favors the Dzyaloshinskii-Moriya Interaction (DMI), which vanishes in the high symmetric cubic structure. Hence the antiskyrmion phase is expected to be stabilized only in the case of  $\text{Mn}_{1.4}\text{PtSn}$  and  $\text{Mn}_{1.4}\text{Pt}_{0.9}\text{Pd}_{0.1}\text{Sn}$  samples. The Curie temperature of  $\text{Mn}_{1.4}\text{PtSn}$ ,  $\text{Mn}_{1.4}\text{Pt}_{0.9}\text{Pd}_{0.1}\text{Sn}$ , and  $\text{Mn}_{1.1}\text{PtSn}$  compounds are 395 K, 375 K, and 335 K, respectively. At low temperatures, a spin reorientation transition is observed for  $\text{Mn}_{1.4}\text{PtSn}$  and  $\text{Mn}_{1.4}\text{Pt}_{0.9}\text{Pd}_{0.1}\text{Sn}$ , whereas no such transition is found for  $\text{Mn}_{1.1}\text{PtSn}$ . The identification of the antiskyrmion phase is carried out using magnetocaloric effect (MCE) and AC susceptibility measurements. The MCE is the change in temperature or magnetic entropy of a magnetic material under an applied magnetic field. During the phase transition from a paramagnetic phase (disorder) to a ferromagnetic phase (order), the total magnetic entropy decreases, leading to a negative magnetic entropy change. The antiskyrmion phase is more disordered compared to the helical phase. Hence the magnetic entropy change during the phase transition from helical to antiskyrmion phase will end up with a positive magnetic entropy change. Using Maxwell's thermodynamic relation, the change in magnetic entropy is calculated by measuring the isothermal magnetization at various temperatures. Near the Curie temperature a negative magnetic entropy change has been observed. As the temperature decreases, the change in magnetic entropy for  $\text{Mn}_{1.4}\text{PtSn}$ ,  $\text{Mn}_{1.4}\text{Pt}_{0.9}\text{Pd}_{0.1}\text{Sn}$  samples start to show a positive value. The positive entropy change is the signature of the presence of the antiskyrmion phase in these samples. Below the spin reorientation temperature, the change in magnetic entropy again becomes negative. This is because, below the spin reorientation temperature, antiskyrmions do not stabilize, as found in the previous real space imaging study using Lorentz Transmission Electron Microscopy measurements (LTEM). [1] The magnetic entropy change for the  $\text{Mn}_{1.1}\text{PtSn}$  sample shows only negative val-

ues for all temperature-field ranges. This is expected as the antiskyrmion phase is not stabilized in this compound. Further, field-dependent AC susceptibility measurements are carried out to probe the antiskyrmion phase. The field-dependent AC susceptibility  $\chi(H)$  measurements show a peak/hump kind of anomaly within the antiskyrmion phase region for both  $\text{Mn}_{1.4}\text{PtSn}$ , and  $\text{Mn}_{1.4}\text{Pt}_{0.9}\text{Pd}_{0.1}\text{Sn}$  systems. Below the spin reorientation transition, no such anomaly is observed in these samples. The peak/hump anomaly is present both at low and high field regions that indicate the nucleation and annihilation of antiskyrmions, respectively. For the case of  $\text{Mn}_{1.1}\text{PtSn}$ , no such feature is observed in  $\chi(H)$  measurements for the whole temperature range from 2 K to 300 K. Utilizing the magnetic entropy change and AC susceptibility measurements, the temperature-field ( $H - T$ ) phase diagram of the antiskyrmion phase for  $\text{Mn}_{1.4}\text{PtSn}$ ,  $\text{Mn}_{1.4}\text{Pt}_{0.9}\text{Pd}_{0.1}\text{Sn}$  samples are constructed. The  $H - T$  phase diagrams show the presence of antiskyrmions over a wide temperature-field range starting from the spin reorientation temperature to the Curie temperature. The phase diagrams constructed using MCE and AC susceptibility measurements are identical to the phase diagram created using the Lorentz transmission electron microscopy (LTEM) study. The study of the antiskyrmion phase using MCE and AC susceptibility is an efficient tool for rapid identification of skyrmion/antiskyrmion phase.

In the second part, the stability and the phase evolution of the antiskyrmion phase are studied by topological Hall effect measurement in a single crystalline device of Mn-Ni-Ga Heusler alloy. The topological Hall effect arises during the movement of conduction electrons through smoothly varying local magnetization of skyrmion/antiskyrmion spin texture. During the motion, the conduction electrons adiabatically couple with the local magnetization and gain a real space Berry phase. The acquired Berry phase applies a fictitious magnetic field on the electron and deflects it in the transverse direction leading to an extra contribution to

the Hall voltage. The topological Hall effect is the electrical signature of magnetic skyrmions/antiskyrmions. In previous report, the antiskyrmion phase was proposed in the polycrystalline  $\text{Mn}_{2+x}\text{Ni}_{1-x}\text{Ga}$  system utilizing the topological Hall effect and AC susceptibility measurements [2, 3]. The major disadvantage of polycrystalline samples is the presence of several grains separated by the grain boundary. Different grains make unequal contributions to the Hall signal and thereby suppressing the overall topological Hall effect due to the antiskyrmion phase. Furthermore, it is observed that the stability of the skyrmion phase under an oblique field varies from system to system. Experimentally, it is found that in a thin lamella, a small in-plane field is necessary to stabilize the antiskyrmion phase [1]. Therefore, it is essential from the fundamental prospect and of relevance for the application point of view to investigate the stability/phase evolution of antiskyrmions under a tilted magnetic field. This type of study needs a single crystalline specimen. In this regard, micron size devices from a single crystalline grain is fabricated using a focused ion beam (FIB). First, a desired single crystalline grain is identified using Electron Back Scattered Diffraction (EBSD) technique. Devices with two different orientations are fabricated; the first one is the out-of-plane device in which the surface is perpendicular to the  $c$ -axis, and the second one is the in-plane device where the surface is perpendicular to the  $ab$  plane. The antiskyrmion phase in these tetragonal materials stabilizes when the magnetic field is applied along the  $c$ -axis. The Selected Area Electron Diffraction (SAED) patterns confirm that the out-of-plane device is oriented along  $[001]$ , and the in-plane device is along  $[010]$  directions. In the in-plane direction, the SAED pattern shows the presence of twin grains, often observed in these materials. The field-dependent Hall resistivity measurements are carried out for the out-of-plane device by applying the field along the  $c$ -axis and the current along  $ab$ . In the Hall resistivity, a dip-like anomaly is observed at the low field region, which is the signature of the topological Hall effect. The observa-

tion of the topological Hall effect confirms the presence of the antiskyrmion phase. Further, the stability and phase evolution of the antiskyrmion phase is investigated under the tilted magnetic field. The tilted field is applied by rotating the sample with respect to [001]. The intensity of the topological Hall signal remains the same up to a tilting angle of  $30^\circ$ . Further increasing the tilting angle, the intensity of the topological feature starts to decrease and disappear at an angle of  $80^\circ$ . The decrease in the topological Hall signature with a tilting angle is due to the annihilation of antiskyrmions. To understand the experimental observation, micro-magnetic simulations (OOMMF) are performed using the experimental parameters. The simulations are accomplished with different in-plane field components corresponding to the tilting angle from the out-of-plane direction (i.e., [001]). The simulation results show that by increasing the tilting angle, the antiskyrmion density reduces, which in turn decreases the topological Hall effect. The presence of antiskyrmion phase up to a large tilting angle is due to the nature of anisotropic DMI, which provides extra resistance against the in-plane field component. The simulation results show some distorted antiskyrmions are still present at a large tilting angle which is due to the nature of anisotropic DMI. For the in-plane device, an aberrant hump kind of feature is observed in the Hall resistivity. The minor loop measurements show that the presence of a hump depends on the field sweeping history. If the hump arises due to the presence of a topological object, then it should not depend on the field history. This confirms that the origin of the hump is due to the superposition of two anomalous Hall loops. The two anomalous loops are extracted from the Hall measurements. The origin of two anomalous Hall loops is due to the presence of twin domains in this direction which is found in TEM microstructure analysis.

The third part of the thesis is dedicated to investigating the anomalous Hall effect (AHE) in the  $\text{MnPt}_{1-x}\text{Ir}_x\text{Sn}$  Heusler alloys. It is believed that the AHE in magnetic systems scales with magnetization. Recent discovery of large AHE in certain

ferromagnetic and antiferromagnetic systems highlight the role of band topology in the emergence of AHE. The anomalous Hall effect (AHE) is caused by two different mechanisms: the intrinsic mechanism and the extrinsic mechanism. The intrinsic mechanism is independent of scattering, while the extrinsic mechanism depends on scattering. Tuning the AHE and manipulating these different mechanisms are important both in terms of fundamental understanding and practical applications. For this purpose, polycrystalline samples of  $\text{MnPt}_{1-x}\text{Ir}_x\text{Sn}$  (with  $x=0, 0.1, 0.2, 0.3, 0.5$ ) are prepared using the arc melt furnace. The room temperature X-ray diffraction (XRD) measurements reveal that all the samples crystallize in a single-phase cubic crystal structure. The Curie temperature ( $T_c$ ) and the saturation magnetization  $M_s$  decreases with increasing the Ir concentration. The reduction of the magnetic moment in the Ir-doped samples is understood using the powder neutron diffraction (ND) measurements. The Rietveld refinement of room temperature ND data for  $\text{MnPt}_{0.5}\text{Ir}_{0.5}\text{Sn}$  reveals the presence of atomic disorder between Mn/Ir atoms. The atomic disorder present in the Ir-doped samples causes the reduction in the magnetic moment. The field-dependent Hall resistivity is measured for all the compounds at different temperatures. The Hall resistivity measurements show an increase of AHE, whereas the magnetic moment decreases with increasing Ir concentration. The microscopic origin of the AHE is investigated using the scaling relation and power law study. The different contributions to the anomalous Hall effect are separated utilizing the scaling relation. It is found that with increasing the Ir percentage, the extrinsic contribution decreases while the intrinsic contribution enhances. The increase in the intrinsic contribution enhances the overall Hall effect. Further, from the power law fitting, the scaling factor is deduced. The scaling factor increases from 1 to 1.93 as the Ir percentage increases. Overall a crossover of extrinsic to intrinsic mechanisms is observed with chemical engineering.



# List of Figures

1.1	Schematic illustration of bulk Dzyaloshinskii-Moriya Interaction (DMI). The DMI originates from the interaction between two spins ( $S_1$ and $S_2$ ) in the presence of a neighboring atom with large spin-orbit coupling. The DM vector is normal to the plane containing $S_1$ and $S_2$ atoms. . . . .	7
1.2	Schematic of spin arrangement in (a) Helical spin texture and (b) Cycloid spin texture. . . . .	11
1.3	Spin configuration of different magnetic skyrmion textures. (a) Bloch Skyrmion (b) Neel Skyrmion (c) Antiskyrmion. Right panel shows the helical (black dashed area) and cycloidal state (red dashed area).	13
1.4	Schematic illustration of DM vectors and their resulting spin configurations. (a)-(b) Orientation of bulk DM vector and corresponding Bloch skyrmion, respectively. (c)-(d) Interface DM vector and corresponding Neel skyrmion, respectively. (e)-(f) Anisotropic DM vector and antiskyrmion spin structure. The lower panels in (b, d, f) show the spin modulations present in different spin textures. . . . .	17
1.5	First experimental observation of magnetic skyrmion in MnSi. (a) The intensity profile of the magnetic skyrmions phase taken using Small Angle Neutron Scattering (SANS). (b) Temperature-field phase diagram of MnSi. [25]. . . . .	18

1.6	Real-space observation of magnetic skyrmion lattice. (a) At low field, helical and skyrmion states are present. (b) At a high field, skyrmion lattice emerges. (c) With increasing the field ferromagnetic state starts to emerge. (d) Temperature-field phase diagram of $\text{Fe}_{0.5}\text{Co}_{0.5}\text{Si}$ [65]. . . . .	19
1.7	Observation of antiskyrmion. (a) LTEM contrast of an antiskyrmion. (b) LTEM image of antiskyrmion lattice. (c) Temperature- Field phase diagram of $\text{Mn}_{1.4}\text{PtSn}$ constructed using LTEM measurements. [1] . . . . .	20
1.8	Schematic representation of Magnetocaloric effect under the magnetic field application. The application of a magnetic field under the isothermal process gives rise to magnetic entropy changes and in the adiabatic process the temperature of the substance changes. . . . .	23
1.9	Schematic illustration of intrinsic deflection. . . . .	27
1.10	Schematic illustration of skew Scattering. The opposite spins are scattered asymmetrically at the impurity side. . . . .	28
1.11	Schematic illustration of side jump scattering. The up and down spin electrons shift their trajectories in opposite directions at the impurity side. . . . .	29
1.12	Scaling relation of AHE of Fe thin films.(a) Black squares are experimental data and red line is the linear fitting using the relation $\frac{\rho_{AH}}{\rho_{xx}}$ vs $\rho_{xx}$ (old scaling). (c) Linear fitting for the relation $\rho_{AH}$ vs $\rho_{xx}^2$ (new scaling) [92]. . . . .	31
1.13	Anomalous Hall effect in $\text{Co}_3\text{Sn}_2\text{S}_2$ . (a) Field-dependent Hall resistivity at several temperatures. (b) Field-dependent magnetization at various temperatures. (c) Plot of $\log\rho_{xy}^A$ vs $\log\rho_{xy}$ . (d) Plot of $\frac{\rho_{xy}^A}{M\rho_{xx}}$ vs $\rho_{xx}$ [82]. . . . .	32

1.14	Observation of skew scattering dominant AHE in Co-doped Fe bulk system. (a) Temperature-dependent normal conductivity ( $\sigma_{xx}$ ). (b) Temperature-dependent Hall conductivity ( $\sigma_{xy}^A$ ). [86]. . . . .	32
1.15	Topological Hall resistivity in the skyrmion phase of MnSi [97]. . . . .	34
1.16	(a)-(d) Field-variation of Hall resistivity at several temperatures at an applied tilted magnetic field. Thick lines represent the experimental data and the thin lines represent the fitting. [98]. . . . .	35
1.17	Topological Hall resistivity of Mn-Ni-Ga Heusler compound. (a)-(b) Field variation of topological Hall resistivity ( $\rho_{xy}^T$ ) for Mn <sub>2</sub> NiGa and Mn <sub>2,1</sub> NiGa <sub>0,9</sub> , respectively (d)-(e) Temperature-field phase diagram of Mn <sub>2</sub> NiGa and Mn <sub>2,1</sub> NiGa <sub>0,9</sub> . (e)-(f) Field variation of topological Hall resistivity ( $\rho_{xy}^T$ ) for Mn <sub>2+x</sub> Ni <sub>1-x</sub> Ga (with x= 0.1,0.3) [2, 3]. . . . .	36
1.18	Periodic table of elements and the colored elements form Heusler alloy. [101] . . . . .	38
1.19	Heusler structure. (a) Half Heusler. (b) Regular full Heusler. (c) Inverse Heusler. . . . .	39
1.20	Transformation of cubic Heusler compound to its corresponding tetragonal structure. (a)-(b) Regular Heusler to tetragonal structure of space group I4/mmm. (c)-(d) Inverse cubic Heusler to the tetragonal structure of space group I $\bar{4}$ m2. . . . .	40
1.21	(a) Schematic of twin crystal structure. (b) Microstructure of twin domains and Selected Area Electron Diffraction (SAED) pattern [116]. (c) Illustration of the magnetic domain in the presence of twin crystals. (d) Image of magnetic (black and white region) and twin domain. The Black and white arrows show the orientation of the magnetic moment [119]. . . . .	42

2.1	Arc-melting furnace used to melt the high-purity elements for synthesizing polycrystalline samples. The components of the furnace are indicated by arrows. . . . .	46
2.2	Schematic of X-ray diffraction scattered from a set of lattice planes.	48
2.3	Schematic of scanning electron microscope (SEM) . . . . .	49
2.4	(a) Illustration of TEM diffraction. (b) Selected Area Electron Diffraction (SAED) pattern. . . . .	50
2.5	Schematic of Vibrating Sample Magnetometer (VSM) with the attachment of SQUID. (The schematic diagram is taken from Quantum Design user's manual) . . . . .	52
2.6	(a) Schematic of FIB system with EBSD detector setup. (b) EBSD mapping of inverse pole figure of a polycrystalline material. Lower panel shows the Kikuchi patterns and color wheel. . . . .	55
2.7	(a) Image of Focused Ion Beam (FIB) system (Crossbeam 340, Zeiss) installed in the School of Physical Sciences, NISER, Bhubaneswar. . . . .	57
2.8	Flow chart of Hall device fabrication. (a) Two big trenches are milled using $Ga^+$ ions to prepare a chunk. (b)-(c) $54^\circ$ and $0^\circ$ SEM view of thin lamella, respectively. (d) L shape cut to free the lamella from two sides. (e) Lift off the lamella using micromanipulator. (f) Si/SiO <sub>2</sub> substrate with predefined gold electrodes. (g) Lamella is mounted on the substrate. (h) False color SEM image of final Hall device with Hall terminals connected to gold electrodes using tungsten deposition.	59
2.9	TEM sample preparation procedure. (a) A protective layer of Pt is deposited. (b) Two sides of the protective layer region are milled. (c) Micromanipulator is attached with the lamella. (d) The lamella is fixed in a Cu grid. (e)-(f) $54^\circ$ and $0^\circ$ SEM view of the polished electron transparent lamella, respectively. . . . .	60

2.10	Different steps of preparing metal electrodes using Electron beam lithography and metal deposition. . . . .	62
2.11	Image of Physical properties measurement system (PPMS, Quantum Design) used to measure the transport properties. The rotator probe and sample puck are shown. . . . .	63
2.12	Schematic of resistivity measurements. (a) Four probe method for longitudinal resistivity measurements. (b) Transverse resistivity measurements using four probe method. (c) Five probe method for transverse resistivity measurements. (d) Electrical connections between the samples and the current/voltage leads of sample carrier. . . . .	64
3.1	Rietveld refinement of powder x-ray diffraction (XRD) of the polycrystalline samples, (a) $\text{Mn}_{1.4}\text{PtSn}$ , (b) $\text{Mn}_{1.4}\text{Pt}_{0.9}\text{Pd}_{0.1}\text{Sn}$ , and (c) $\text{Mn}_{1.1}\text{PtSn}$ . . . . .	67
3.2	(a) Tetragonal crystal structure $\text{Mn}_{1.4}\text{PtSn}$ having space group $\bar{I}4_2m$ (No 121). (b) Crystal structure of $\text{Mn}_{1.1}\text{PtSn}$ with space group $F\bar{4}3m$ (No 216). . . . .	68
3.3	Scanning electron microscopy (SEM) images for (a) $\text{Mn}_{1.4}\text{PtSn}$ , (b) $\text{Mn}_{1.4}\text{Pt}_{0.9}\text{Pd}_{0.1}\text{Sn}$ , and (c) $\text{Mn}_{1.1}\text{PtSn}$ . . . . .	69
3.4	Magnetization measurements. Temperature variation of zero field-cooled (ZFC, open symbols) and field-cooled (FC, close symbols) DC magnetization curve measured with an applied field of 0.1 T for (a) $\text{Mn}_{1.4}\text{PtSn}$ , (b) $\text{Mn}_{1.4}\text{Pt}_{0.9}\text{Pd}_{0.1}\text{Sn}$ , and (c) $\text{Mn}_{1.1}\text{PtSn}$ . Inset depicts the first derivative of DC magnetization with temperature. Field variation of magnetization loop at 2 K (black curve) and 300 K (red curve) for (d) $\text{Mn}_{1.4}\text{PtSn}$ , (e) $\text{Mn}_{1.4}\text{Pt}_{0.9}\text{Pd}_{0.1}\text{Sn}$ and (f) $\text{Mn}_{1.1}\text{PtSn}$ . . . . .	71

- 3.5 Isothermal magnetization curves as a function of the magnetic field at different temperatures for (a)  $\text{Mn}_{1.4}\text{PtSn}$ , (b)  $\text{Mn}_{1.4}\text{Pt}_{0.9}\text{Pd}_{0.1}\text{Sn}$ , and (c)  $\text{Mn}_{1.1}\text{PtSn}$ . The temperature range and the temperature interval ( $\Delta T$ ) are indicated in the figure. Change of magnetic entropy  $\Delta S_M$  as a function of temperature in a field range from 0.02 T to 1 T for (d)  $\text{Mn}_{1.4}\text{PtSn}$ , (e)  $\text{Mn}_{1.4}\text{Pt}_{0.9}\text{Pd}_{0.1}\text{Sn}$ , and (f)  $\text{Mn}_{1.1}\text{PtSn}$ . 3D illustration of positive magnetic entropy change  $\Delta S_M$  for (g)  $\text{Mn}_{1.4}\text{PtSn}$  and (h)  $\text{Mn}_{1.4}\text{Pt}_{0.9}\text{Pd}_{0.1}\text{Sn}$ . . . . . 73
- 3.6 (a)- (g) Magnetic field variation of real part of AC susceptibility [ $\chi'$  (H)] at different temperatures for the  $\text{Mn}_{1.4}\text{PtSn}$ . The measurement temperatures are indicated in the figure. The black arrow depicts the anomaly peak/hump kind of feature. . . . . 75
- 3.7 (a) - (f) Magnetic field variation of real part of AC susceptibility [ $\chi'$  (H)] at different temperatures for  $\text{Mn}_{1.4}\text{Pt}_{0.9}\text{Pd}_{0.1}\text{Sn}$ . (g)-(h) Magnetic field variation of real part of AC susceptibility [ $\chi'$  (H)] for  $\text{Mn}_{1.1}\text{PtSn}$ . The measurement temperatures are indicated in the figure. The Black arrows depict the anomaly peak/hump kind of feature. . . . . 76
- 3.8 (a)-(b) Temperature - field ( $H - T$ ) phase diagram of antiskyrmion phase constructed using the magnetic entropy change for  $\text{Mn}_{1.4}\text{PtSn}$  and  $\text{Mn}_{1.4}\text{Pt}_{0.9}\text{Pd}_{0.1}\text{Sn}$ , respectively. Negative and positive magnetic entropy changes are ( $\Delta S_M$ ) shown in the color bar. (c)-(d) Temperature-field ( $H - T$ ) phase diagram of antiskyrmion phase derives from field-dependent AC susceptibility measurements for  $\text{Mn}_{1.4}\text{PtSn}$  and  $\text{Mn}_{1.4}\text{Pt}_{0.9}\text{Pd}_{0.1}\text{Sn}$ , respectively. . . . . 78

- 4.1 Tetragonal crystal structure of  $\text{Mn}_2\text{NiGa}$  with space group  $I\bar{4}m2$  (No. 119). MnI, MnII, Ni, and Ga atoms are represented by the red, blue, orange, and green atoms, respectively. . . . . 83
- 4.2 Orientation of Hall devices. (a) Electron Backscatter Diffraction (EBSD) pattern of polycrystalline  $\text{Mn}_{2.13}\text{Ni}_{0.87}\text{Ga}$ . The orientation of the green color region is  $[100]$ . (b) SEM image of the single crystalline grain ( $[100]$ ) from where the Hall bars (from areas 1 and 3) and TEM specimens (from areas 2 and 4) are prepared. (c)-(d) False-color SEM images of the out-of-plane and the in-plane devices, respectively. The crystallographic directions, current, and voltage connections are shown in the figure. The light yellow regions are the gold electrodes. (e) Selected Area Electron Diffraction (SAED) pattern collected for the sample specimen prepared from area-2 with out-of-plane orientation. (f) SAED pattern collected for the in-plane orientation with TEM sample prepared from area-4. Inset under the red dashed area shows the magnifying view of  $(00\bar{8})$  spot. . . . . 85
- 4.3 Temperature variation of longitudinal resistivity for (a) out-of-plane  $[\rho_{xx}(T)]$  and (b) in-plane  $[\rho_{zz}(T)]$  devices. Field-dependent longitudinal resistivity for (c) out-of-plane  $[\rho_{xx}(H)]$  and (d) in-plane  $[\rho_{zz}(H)]$  devices. . . . . 87
- 4.4 (a)-(f) Field variation of Hall resistivity  $[\rho_{xy}(H)]$  for the out-of-plane device at different temperatures. The field is applied along the c-axis ( $H//c$ ), and current is applied along the  $ab$  plane ( $I//ab$ ). . . . . 89

- 
- 4.5 (a)-(f) Hall resistivity  $[\rho_{xy}]$  as a function of magnetic field at different tilting angles with respect to the  $c$ -axis. Inset in (a) shows the schematic of the direction of magnetic field with respect to the  $c$ -axis. The current is applied along the  $ab$  plane. The inclination angle  $\theta$  is the angle between the  $c$ -axis and the magnetic field direction. . . . . 90
- 4.6 Antiskyrmion phase with the variation of tilting angle with respect to the  $c$ -axis derived from the Hall resistivity measurements. . . . . 92
- 4.7 (a)-(f) Field variation of Hall resistivity for the in-plane device at different temperatures. The magnetic field is applied along the  $ab$  plane ( $H//ab$ ), and the current is applied along the  $c$ -axis ( $I // c$ ). . . . . 93
- 4.8 Room temperature minor loop Hall resistivity  $[\rho_{zy}]$  measurements. (a) Measurement started at +5 T and stopped at -2 T (red curve), then came back to +5 T (green curve). (b) Measurement started at -5 T and stopped at +2 T (red curve), then came back to -5 T (green curve). (c) Measurement started at +5 T and stopped at -3.2 T (red curve), then came back to +5 T (green curve). Arrows depict the direction of the field sweep. . . . . 95
- 4.9 (a) Decomposition procedure of two anomalous Hall loops. Red (solid dark yellow) curve is the Hall resistivity data measured from +5 T to -5 T (-5 T to +5 T). Dashed dark yellow line is the shifted data of the solid dark yellow curve. Blue curve is the minor loop measurements with +5 T to -2 T. (b) Decomposed two anomalous Hall loops. . . . . 96
- 4.10 (a)-(f) Hall resistivity  $[\rho_{zy}]$  for the in-plane device with the variation of tilted magnetic field. Inset of (a) shows the schematic of the measurement configuration. The current is applied along the  $c$ -axis. The inclination angle  $\theta$  is the angle between the  $ab$  plane and the applied magnetic field. . . . . 98

4.11	Microstructural analysis. (a) Microstructure of in-plane oriented lamella taken using TEM. The black arrow shows the nano-twin bundles. (b) TEM image of the out-of-plane oriented lamella. (c) Schematic of twin domains. Yellow and dark yellow regions represent the twin crystal domains. Black and Yellow arrows represent the magnetic moment. The magnetic moments form $90^\circ$ domains in the adjacent twin variants and $180^\circ$ domains in a single variant. (d) Effect on the magnetic moment by applying out-of-plane field component ( $H_z$ ). At large out-of-plane field only single magnetic domain forms. . . . .	99
4.12	Field variation of Hall resistivity for the (a) out-of-plane [ $\rho_{xy}$ ] and (b) in-plane [ $\rho_{zy}$ ] device. Insets show the corresponding devices fabricated from a different region. . . . .	100
4.13	Micromagnetic simulations. (a) Schematic of field configuration in the presence of an inclined magnetic field. $\theta$ denotes the angle between the magnetic field and the normal direction. $H_z$ and $H_x$ are the out-of-plane and in-plane field components, respectively. (b)-(i) Spin textures from the micromagnetic simulation results under the application of different tilted magnetic fields. The angle of inclination is mentioned in the figure. The color bar shows the out-of-plane magnetization. . . . .	101
5.1	Rietveld refinement of room temperature powder XRD patterns for $\text{MnPt}_{1-x}\text{Ir}_x\text{Sn}$ with $x=0, 0.1, 0.2, 0.3, 0.5$ . . . . .	108
5.2	(a)-(e) Scanning electron microscopy images of $\text{MnPt}_{1-x}\text{Ir}_x\text{Sn}$ , with $x=0, 0.1, 0.2, 0.3, 0.5$ . . . . .	109

5.3	Temperature variation of zero field-cooled (ZFC) and field-cooled (FC) magnetization curve for $\text{MnPt}_{1-x}\text{Ir}_x\text{Sn}$ , with $x= 0, 0.1, 0.2, 0.3, 0.5$ . The applied field is 1 KOe. (f) Plot of Curie temperature ( $T_C$ ) with Ir concentration. . . . .	111
5.4	Magnetic hysteresis loops measured at 5 K for $\text{MnPt}_{1-x}\text{Ir}_x\text{Sn}$ , with $x= 0, 0.1, 0.2, 0.3, 0.5$ . (f) Variation of saturation magnetization ( $M_S$ ) with Ir concentration. . . . .	112
5.5	Structural Rietveld refinement of powder neutron diffraction data for $\text{MnPt}_{0.5}\text{Ir}_{0.5}\text{Sn}$ recorded at 300 K with different atomic disorders between Mn/Ir atom. (a)-(e) Rietveld refinement of powder ND pattern with 0 %, 5 %, 10 %, 15 % and 20 % atomic disorder, respectively. The region between $34^\circ$ to $36^\circ$ , is clipped due to contributions from the cryostat. . . . .	114
5.6	(a) Crystal structure of $\text{MnPtSn}$ . (b) Crystal structure of $\text{MnPt}_{0.5}\text{Ir}_{0.5}\text{Sn}$ with 10 % atomic disorder between Mn/Ir atoms. . . . .	115
5.7	(a) Rietveld refinement of powder neutron diffraction (ND) patterns for $\text{MnPtSn}$ collected at 2 K. (b) Rietveld refinement of powder ND pattern for $\text{MnPt}_{0.5}\text{Ir}_{0.5}\text{Sn}$ collected at 2 K, with 10 % atomic disorder. . . . .	116
5.8	Temperature variation of longitudinal resistivity $\rho_{xx}(T)$ for $\text{MnPt}_{1-x}\text{Ir}_x\text{Sn}$ , with $x= 0, 0.1, 0.2, 0.3, 0.5$ . . . . .	117
5.9	(a-e) The Hall resistivity as a function of magnetic field at different temperatures for $\text{MnPt}_{1-x}\text{Ir}_x\text{Sn}$ , with $x= 0, 0.1, 0.2, 0.3, 0.5$ . (f) Plot of anomalous Hall resistivity ( $\rho_{xy}^A$ ) with Ir concentration at 5K . . . .	119

- 5.10 (a) Anomalous Hall resistivity ( $\rho_{xy}^A$ , magenta curve) and saturation magnetization at 5 K with Ir concentration. (b) Variation of anomalous Hall conductivity ( $\sigma_{xy}^A$ ) with Ir concentration at 5 K. (c) Plot of anomalous Hall angle (AHA) as a function of Ir percentage at 5 K. . . . . 120
- 5.11 Scaling relation. (a-e) Plot of anomalous Hall resistivity ( $\rho_{xy}^A$ ) with square of longitudinal resistivity ( $\rho_{xx}^2$ ) for  $\text{MnPt}_{1-x}\text{Ir}_x\text{Sn}$ , with  $x=0, 0.1, 0.2, 0.3, 0.5$ . The circular data points are the experimental data and the solid line is the linear fitting. Horizontal top axes illustrate the corresponding measurement temperatures. (f) The variation of extrinsic ‘a’ (square points) and intrinsic ‘b’ parameter (triangle points) with Ir concentration. . . . . 121
- 5.12 Power law fitting. (a)-(e) Plot of  $\log(\rho_{xy}^A)$  vs  $\log(\rho_{xx})$  for  $\text{MnPt}_{1-x}\text{Ir}_x\text{Sn}$ , with  $x=0, 0.1, 0.2, 0.3, 0.5$ . The circular points are the experimental data, and the solid line is the linear fitting. Horizontal top axes illustrate the corresponding measurement temperatures. (f) Variation of scaling factor  $\alpha$  with Ir concentration. . . . . 123
- 5.13 Different contributions of anomalous Hall effect as a function of Ir concentration for  $\text{MnPt}_{1-x}\text{Ir}_x\text{Sn}$ , with  $x=0, 0.1, 0.2, 0.3, 0.5$ . Left triangles represent the intrinsic contribution, right triangles represent the skew scattering contribution, and diamond symbols are used for the side jump contribution. . . . . 124



# Chapter 1

## Introduction

The field of *Spintronics* emerges as a promising alternative to overcome some of the limitations of traditional charge-based devices, e.g., high power consumption, elevated operating voltage, limitation in size reduction to achieve high density, and slow processing time [4, 5]. In contrast to electronic devices, spintronics devices possess the potential to create high storage density, non-volatile memory with low power consumption, fast processing, high endurance, and effective read and write capabilities [6, 7, 8, 9, 10, 11, 12, 13]. The fundamental concept of spintronics is to utilize the spin degree of freedom along with the charge of the electrons. The field of spintronics got a major boost after the discovery of Giant Magneto Resistance (GMR) in 1988-1989 [14, 15]. The basic principle of the GMR is the resistance change depending on the relative orientation of the magnetization of two ferromagnetic layers separated by a non-magnetic thin spacer. The parallel alignment of the magnetic moments in the two magnetic layers leads to lower resistance, whereas the anti-parallel alignment gives higher resistance to the electrical flow. The commercial application of the GMR phenomenon was started in the form of spin valves in magnetic hard disk drives (HDD) [16, 17]. In 1995, the groundbreaking discovery of room temperature tunneling magnetoresistance (TMR) in magnetic tunnel junction (MTJ) device made a major advancement in the spintronics field [18, 19]. In MTJ, a thin insulating layer sandwiched between two magnetic layers, deter-

mines the electrical resistivity states. Depending on the relative orientation of the magnetic moments in the magnetic layers, the tunneling electrons experience higher (antiparticle alignment) or lower resistance (parallel alignment). These high and low resistance states are used as 1 and 0 bits, respectively, in magnetic random access memory (MRAM) devices. The success of HDD and MRAM devices motivates the spintronics community to develop devices for different applications based on various phenomena related to the spin degree of freedom observed in magnetic materials [20, 21, 22]. Although HDDs and MRAMs have achieved notable success, there are still major concerns regarding their processing speed and production cost. The limitations of HDDs and MRAMs can be addressed by using alternative magnetic memory concepts, e.g., *racetrack memory*, a proposed technology developed by Stuart Parkin et al. [23, 24]. In this proposed memory device, the domains of opposite magnetization separated by domain walls are used to store the data. The spin-polarized current can move the domain walls (DWs) in back and forth direction to intersect the reading and writing head. However, a large current density is required to move the DWs. Recently, it is proposed that the difficulties associated with domain wall motion can be overcome by the use of non-trivial spin textures, such as magnetic skyrmions/antiskyrmions as a magnetic bits.

Magnetic skyrmions/antiskyrmions are topologically protected magnetic objects with vortex type of spin texture [25, 26, 27]. Individual skyrmions/antiskyrmions are assigned to a particular integer number called a topological number or skyrmion number. This integer number allows them to behave like a particle and can be moved with less deepening current density compared to DWs [28, 29, 30]. The topological nature of the skyrmions/antiskyrmions protects them from external perturbations and can avoid the pinning center during their motion. Hence, these non-trivial magnetic objects are promising candidates for the realization of future generation memory and logic devices.

For the successful integration of magnetic skyrmions in spintronics devices, it is important to investigate their behavior under different external conditions. At the same time, it is necessary to study different electron transport phenomena, such

as the anomalous Hall effect (AHE) and topological Hall effect (THE), that occur during the motion of electrons through these topological magnetic states. These transport phenomena are the electrical manifestation of different magnetic states. For example, the THE is the electrical footprint of non-trivial spin textures that can be used to characterize these spin textures as a reading element in memory devices [31]. On the other hand, AHE reveals the complex interplay between the underlying electric and magnetic properties of the system. The AHE is useful for the generation of dissipation-less transverse current and has the potential for the advancement of spintronics devices, such as memory applications, logic devices, and switching devices [32, 33]. In some recent theoretical work, it is proposed that the AHE can play a crucial role for the generation of spin transfer torque (STT) [34, 35] and spin torque [36, 37], which can be used to move the skyrmion/antiskyrmion. These aspects of AHE make it an important ingredient for future spintronics devices. Therefore, the characterization of non-trivial spin textures and the study of anomalous electronic transport properties provide a limitless opportunity for the realization of modern cutting-edge spintronics devices.

In the following, a brief introduction is given to different magnetic interactions that are primarily responsible for the stabilization of magnetic structures used in the present thesis. The description of non-trivial spin textures and anomalous electronic transport properties, along with a short literature review is also presented. Finally, various aspects of Heusler materials used for the present thesis are included.

## 1.1 Fundamental magnetic interactions

### 1.1.1 Exchange interaction

The exchange interaction is the predominant interaction observed in almost all magnetic systems. It is a quantum mechanical effect and stems from the combination of Coulomb interaction and Pauli's exclusion principle. A successful explanation of long-range magnetic ordering is possible using the concept of exchange interaction.

The exchange energy between two neighboring spins is expressed as,

$$H = -2JS_1 \cdot S_2 \quad (1.1)$$

where  $J$  is the exchange integral. This is the Heisenberg exchange interaction for two neighboring spins, and for many body systems, the Hamiltonian of exchange energy between the  $i$ -th and  $j$ -th spins can be written as,

$$H = - \sum J_{ij} S_i \cdot S_j \quad (1.2)$$

where  $J_{ij}$  represents the exchange constant between  $i$ -th and  $j$ -th spins. Factor 2 is included inside the summation with double counting. For neighboring spins,  $J_{ij}$  is taken as constant  $J$  and 0 otherwise. The sign of exchange constant  $J$  determines the arrangement of neighboring spins. The positive  $J$  value favors a parallel alignment, i.e., ferromagnetic (FM) arrangement, and the negative  $J$  value supports antiparallel alignment, i.e., antiferromagnetic (AFM) arrangement.

### 1.1.2 Dzyaloshinskii - Moriya interaction (DMI)

Certain magnetic systems lacking inversion symmetry and with considerable spin-orbit coupling (SOC) possess an asymmetric interaction called Dzyaloshinskii-Moriya Interaction (DMI). The Hamiltonian of this interaction is expressed as

$$H_{DM} = -D_{ij} \cdot (S_i \times S_j) \quad (1.3)$$

where  $D_{ij}$  is the Dzyaloshinskii-Moriya (DM) vector. The schematic of DMI between two spins  $S_1$  and  $S_2$  in the presence of a heavy atom with large spin-orbit coupling (SOC) is shown in Fig. 1.1. The resultant DMI is perpendicular to the plane containing the  $S_1$ ,  $S_2$ , and the heavy atoms. The total energy is minimum when the spins  $S_i$  and  $S_j$  align perpendicular to each other. Unlike the exchange interaction, DMI favors the perpendicular alignment of neighboring spins. This

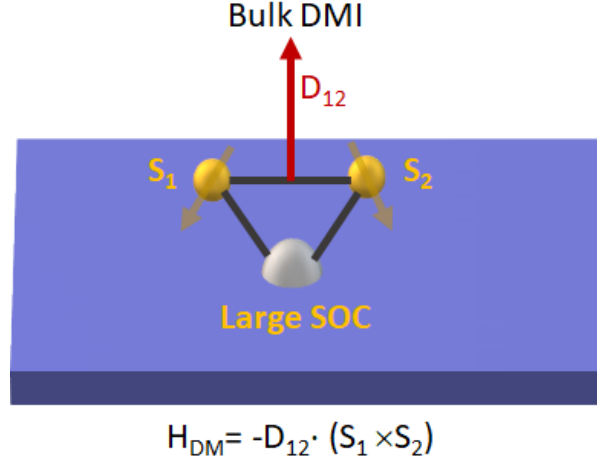


Figure 1.1: Schematic illustration of bulk Dzyaloshinskii-Moriya Interaction (DMI). The DMI originates from the interaction between two spins ( $S_1$  and  $S_2$ ) in the presence of a neighboring atom with large spin-orbit coupling. The DM vector is normal to the plane containing  $S_1$  and  $S_2$  atoms.

interaction was first proposed by Igor Dzyaloshinskii in 1958 [38] to explain the presence of ferromagnetic components in the antiferromagnetic compound  $\alpha$ - $\text{Fe}_2\text{O}_3$ . The presence of this interaction gives some unique magnetic states, i.e., in the case of  $\alpha$ - $\text{Fe}_2\text{O}_3$ , the exchange interaction tries to align the neighboring spins antiparallel to each other, while the DMI prefers a perpendicular alignment between the spins. As a result, a canted magnetic structure is stabilized in  $\alpha$ - $\text{Fe}_2\text{O}_3$ . Later, in 1960, Toru Moriya [39] proposed the microscopic theory of this interaction. The strength of DMI depends on the value of SOC, which is at least one order less in magnitude than that of exchange interaction. In his original paper, Moriya gives certain rules known as Moriya rules that describe the direction of the DM vector acting between two spins. Considering two spins are sitting at sites A and B, and C is the point bisecting the line AB, these rules are described as.

- (i)  $D = 0$  if an inversion symmetry is present at point C.
- (ii)  $D \perp AB$  if there exists a mirror plane that is perpendicular to AB and passes through the point C.
- (iii) If the mirror plane includes the points A and B, then D will be normal to mirror

plane.

(iv) When there exists a two-fold rotation axis that is normal to AB and passing through C, then the direction D will be  $\perp$  to two-fold axis.

(v) For  $n$  ( $n \geq 2$ ) fold axis along AB, the direction of D will be  $D \parallel AB$ .

Recently, the DMI receives much attention because of observing several non-collinear spin textures, such as helical modulation, cycloidal state, conical spin configuration, and magnetic skyrmion. The stabilization mechanism of these spin textures are understood in terms of different competing interactions, including DMI.

### 1.1.3 Magnetic anisotropy

The preferential alignment of magnetic moments in certain directions is known as magnetic anisotropy, which arises due to the presence of spin-orbit coupling (SOC). The electron orbitals are connected with the crystal axis, and the interaction between orbitals with the spin makes preferential alignment of the moments along a particular crystallographic axis. The strength of the magnetic anisotropy energy is much smaller than the exchange interaction, but the anisotropy decides the direction of the magnetization. This is because the exchange interaction is isotropic, which tries to align the moment in all directions. Anisotropy makes it easier to magnetize a magnetic material along a certain direction, called the easy axis of magnetization. Similarly, it requires a large energy to magnetize in a direction known as the hard axis. The direction of the easy and hard axes varies from system to system. For example, in the case of bcc Fe, [100] is the easy axis, while [111] is the hard axis. For fcc Ni, the easy axis is along [111], while [100] is hard axis [40]. The anisotropic magneto-crystalline energy for cubic crystal systems is expressed as

$$E_{anisotropy}^{Cubic} = K_0 + K_1(\alpha_x^2\alpha_y^2 + \alpha_y^2\alpha_z^2 + \alpha_z^2\alpha_x^2) + K_2\alpha_x^2\alpha_y^2\alpha_z^2 + \dots \quad (1.4)$$

where  $K_1, K_2, K_3$  are the anisotropy constants and  $\alpha_x, \alpha_y,$  and  $\alpha_x$  are the cosine angles of magnetization with the crystallographic axes a, b, c. In the case of tetragonal

and hexagonal crystal structures, the anisotropic energy is written as

$$E_{anisotropy} = K_0 + K_1 \sin^2\theta + K_2 \sin^4\theta + \dots \quad (1.5)$$

where  $\theta$  denotes the angle between the magnetization and c-axis. Depending on the values of the anisotropy constant the easy axis can vary from system to system. For positive values of  $K_1$  and  $K_2$ , the anisotropy energy will be minimum for  $\theta = 0$ . This means the easy axis will be along the c-axis, i.e., along [001]. This is called uniaxial anisotropy, as the anisotropy axis is along one direction. For the negative value of  $K$ 's the energy will be minimum for  $\sin\theta = 1$ , which means the easy axis will be along the basal plane, and [001] will be the hard axis. For the mixture of negative and positive values of the anisotropy constants, there will be a continuous rotation of the easy axis from the c-axis to the basal plane.

#### 1.1.4 Dipolar interaction

Like the electric dipoles, all the magnetic dipoles interact through dipolar interaction. The interactions discussed in the above sections are short-range in nature, whereas the dipolar interaction is a long-range interaction. The dipolar energy of two dipoles with dipole moments  $m_1$  and  $m_2$  is expressed as

$$E_{Dipole} = -\frac{\mu_o}{4\pi} \left[ -\frac{3(\vec{m}_1 \cdot \vec{r}_1)(\vec{m}_2 \cdot \vec{r}_2)}{r^5} + \frac{\vec{m}_1 \cdot \vec{m}_2}{r^3} \right]. \quad (1.6)$$

Here  $r_i$  is the distance between the two dipoles. The dipole interaction is very weak in comparison to other interactions. The dipolar energy is minimum if the dipoles lie along the same plane.

### 1.1.5 Zeeman energy

The magnetic moment  $\mu$  interacts with the external magnetic field  $H$  and is known as the Zeeman interaction. The Zeeman energy is expressed as

$$E_{Zeeman} = -\mu S_i \cdot H \quad (1.7)$$

The Zeeman interaction tries to align the magnetic moment along the external field direction.

## 1.2 Non-collinear spin texture

Depending on the presence of various interactions in magnetic materials, different types of spin arrangements are possible. For convenience, one can make two categories to discuss the several spin textures present in magnetic systems. The first one is the collinear spin textures, and the second one is the non-collinear state. Three types of collinear spin arrangements, such as ferromagnetic, ferrimagnetic, and antiferromagnetic are found.

Apart from the collinear spin textures, certain types of non-collinear spin states are also observed in several magnetic systems. In most of the cases, the non-collinear magnetic structures emerge due to the presence of competing interactions. In recent times, these spin arrangements have been the center of attraction due to their captivating and intriguing properties. In the following, a discussion related to some of the important non-collinear spin textures is presented.

### Helical spin structure

In helical spin textures, the spins rotate in a plane normal to the direction of the propagation vector. The spin configuration in a helical spin structure is shown in Fig. 1.2 (a). Helical spin texture forms due to the competition of different magnetic interactions, such as the exchange interaction and DM interaction. In case the helical

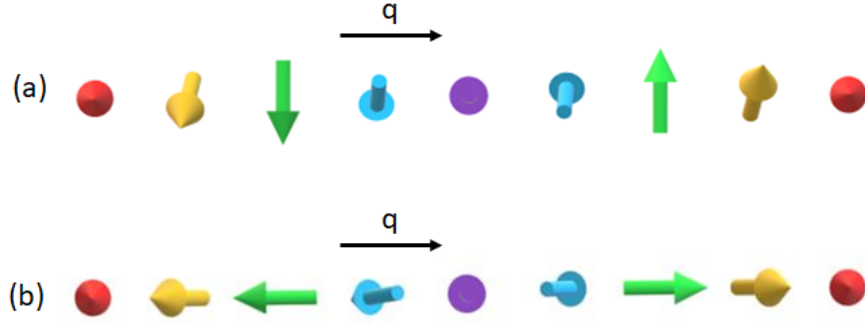


Figure 1.2: Schematic of spin arrangement in (a) Helical spin texture and (b) Cycloid spin texture.

modulation is stabilized by competing DMI and exchange interaction, the angle of rotation of the magnetic moments depends on the ratio of exchange integral  $J$  and DM vector  $D$ . The DM vector  $D$  determine the propagation direction of the helical structure. The helical modulation of the magnetic moments has been observed in several materials [25, 26, 27, 41, 42, 43, 44].

### Cycloid spin structure

In addition to the helical spin texture, another kind of spin modulation, named cycloid spin structure, is also observed as a ground state in certain magnetic materials with particular crystal symmetry. Figure 1.2 (b) shows the schematic diagram of the cycloid spin texture, in which the spins rotate in a plane parallel to the propagation direction. Competing magnetic interactions, such as exchange and DM interaction, give rise to this spin texture. This type of spin texture is generally found in multi-layer systems with interfacial DMI [45, 46, 47, 48, 49]. In some bulk materials such as  $\text{GaV}_4\text{S}_8$  [50],  $\text{MnPtGa}$  [51], and in  $\text{Cr}_{1+\delta}\text{Te}_2$  [52], cycloid spin texture has been observed.

### Conical spin structure

The conical spin texture can be stabilized under the application of magnetic field in the helical ground state. In general, the conical spin configuration is not a ground state. In this case, the spins make an angle with the propagation direction, and

the tilting angle depends on the applied magnetic field. The conical spin texture is observed in several magnetic systems such as  $\text{LaMn}_2\text{X}_2$  ( $\text{X}=\text{Ge},\text{Si}$ ) [53],  $\text{MnSi}$  [25],  $\text{FeGe}$  [27],  $\text{Cu}_2\text{OSeO}_3$  [54], etc.

### 1.3 Magnetic Skyrmions

Over the last decade, among all the non-collinear magnetic structures, skyrmions have attracted significant attention of the spintronics community. The concept of Skyrmion was initially proposed in high-energy physics by Tony Skyrme [55] to explain the chiral model of Hadrons in nuclear physics. These skyrmions are topologically protected as they possess a topological integer number that can not be altered by a continuous change of a field configuration. Later, Bogdanov et al. [56] proposed that the concept of magnetic skyrmions can be realized in chiral magnets with particular symmetry. These spin configurations can be topologically protected with integer topological numbers and behave like a particle. In his work, he predict that the skyrmion type of spin texture can be stabilized in a system with crystal symmetry such as  $C_n$ ,  $C_{nv}$ ,  $D_n$ ,  $D_{2d}$ , and  $S_4$ . In 2009, magnetic skyrmions were experimentally discovered in  $\text{MnSi}$  using Small Angle Neutron Scattering (SANS) [25]. Afterward, in 2010 magnetic skyrmions were visualized directly in real space using Lorentz Transmission Electron Microscopy (LTEM) in  $\text{Fe}_{0.5}\text{Co}_{0.5}\text{Si}$  thin lamella [26].

Magnetic Skyrmions are particle-like topologically protected vortex type of incommensurate spin configuration with a fixed topological integer number  $Q = \pm 1$ . The topological number  $Q$  or skyrmion number  $N_{sk}$  is expressed as

$$N_{sk} = \int n_{sk} dx dy = \frac{1}{4\pi} \int \int \mathbf{m} \cdot \left( \frac{\partial \mathbf{m}}{\partial x} \times \frac{\partial \mathbf{m}}{\partial y} \right) dx dy \quad (1.8)$$

where  $n_{sk} = \frac{1}{4\pi} \mathbf{m} \cdot \left( \frac{\partial \mathbf{m}}{\partial x} \times \frac{\partial \mathbf{m}}{\partial y} \right)$  is the topological charge density and  $m(r)$  is the magnetization density. The Skyrmion number  $N_{sk}$  is defined as the number of times the spin configuration can wrap a unit sphere. Figure 1.3 depicts the spin texture

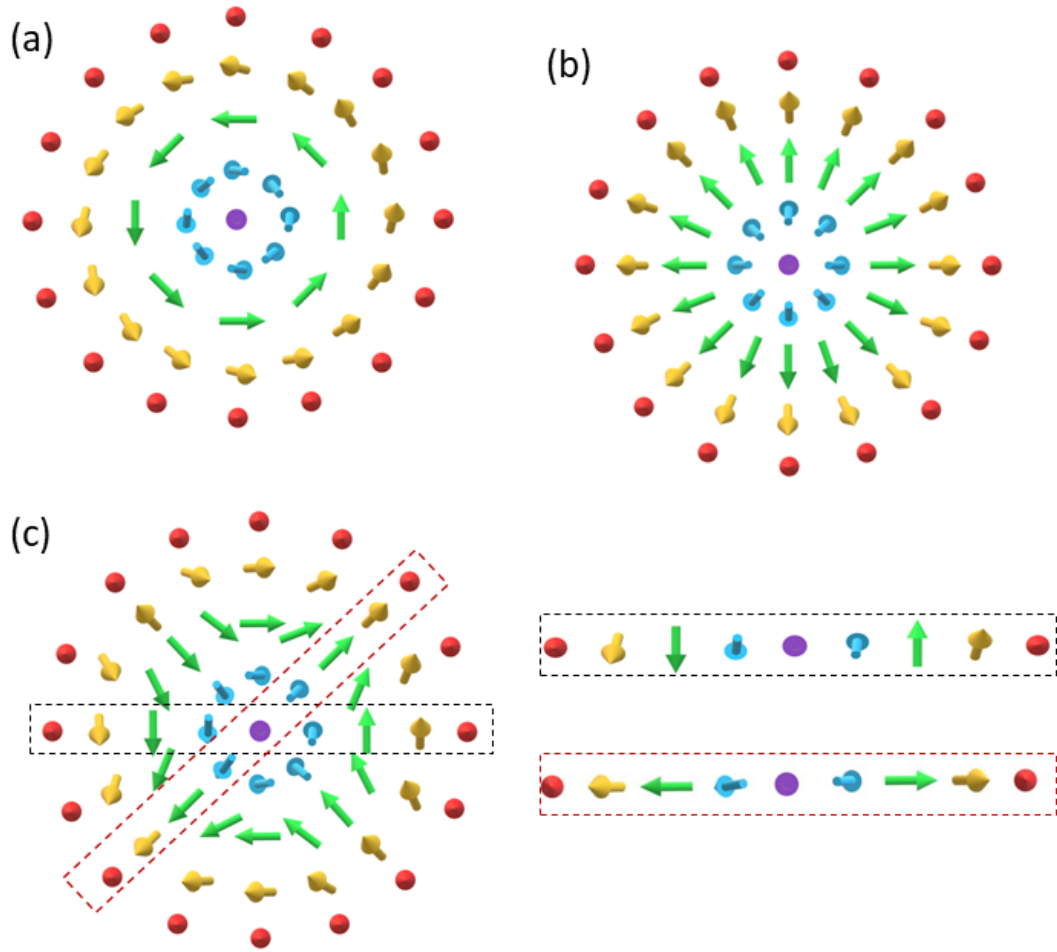


Figure 1.3: Spin configuration of different magnetic skyrmion textures. (a) Bloch Skyrmion (b) Neel Skyrmion (c) Antiskyrmion. Right panel shows the helical (black dashed area) and cycloidal state (red dashed area).

of magnetic skyrmions. In the skyrmion structure, the magnetic moment at the core is pointing in a downward direction. As one moves from the center, the spins are rotated and at the periphery, the spins are pointing in the upward direction. Depending on the sense of spin rotation, known as helicity, various kind of skyrmions are possible [shown in Fig. 1.3]. These are (1) Bloch skyrmion [1.3 (a)], in which the spins rotate like helical spin texture [25, 27, 54], (2) Neel skyrmion [1.3 (b)], wherein the spins exhibit a cycloid spin modulation [47, 49, 50, 51] and (3) antiskyrmion [1.3 (c)], where both helical and cycloid spin rotation are present [marked by red and black dashed boxes in Fig. 1.3 (c)] [1, 57]. The helicity for Bloch skyrmion is  $\pm\frac{\pi}{2}$ , for Neel Skyrmion it is 0 or  $\pi$ , and the antiskyrmion can have arbitrary helicity.

[58].

### 1.3.1 Stabilization mechanism of different topologically equivalent Skyrmionic textures

The competition of exchange interaction, DMI, and magnetic anisotropy are responsible for stabilizing the magnetic skyrmion in the presence of an external magnetic field. In general, the competition of these interactions gives rise to a spin spiral state, which breaks into skyrmions/antiskyrmions in the presence of a magnetic field. The anisotropy energy plays an important role in deciding the propagation direction. In B20 crystal, several helical propagation directions exist due to the cubic crystal symmetry [25, 59]. In  $D_{2d}$  materials such as  $\text{Mn}_{1.4}\text{Pt(Pd)Sn}$  system, the helical propagations are found only in [100] and [010] directions [60, 61]. The application of a magnetic field along [001] direction breaks the helical states to give antiskyrmion lattice [1, 62, 63].

Although the non-collinear spin textures can be stabilized in the presence of several interactions, particularly in the case of non-centrosymmetric systems, the DMI is responsible for stabilizing different types of skyrmions with fixed chirality. The symmetry of the crystal structure governs the different forms of DMI, which stabilizes various types of topologically equivalent spin textures [64]. The orientations of DM vector  $D_{ij}$  depends on how the inversion symmetry is broken. Distinct crystal symmetries give rise to varying forms of the DM vector, which, in turn, stabilize diverse spin textures. The following section discusses different forms of DMI that stabilize skyrmionic spin textures.

#### Stabilization of Bloch skyrmion with bulk DMI

In the case of magnetic materials with B20 symmetry, such as MnSi and FeGe, the inversion symmetry is broken intrinsically. The DMI for the B20 symmetry based

system can be expressed as

$$H_{bulk} = \int D(m_y \frac{\partial m_z}{\partial x} - m_z \frac{\partial m_y}{\partial x} + m_z \frac{\partial m_x}{\partial y} - m_x \frac{\partial m_z}{\partial y} + m_x \frac{\partial m_y}{\partial z} - m_y \frac{\partial m_x}{\partial z}) dV. \quad (1.9)$$

The orientation of the bulk DM vector and the corresponding Bloch skyrmion are shown in Figs. 1.4 (a) and (b). Here  $D_x$  and  $D_y$  is the DM vector along x and y direction, respectively. The  $D_x$  and  $D_y$  vector lies parallel or antiparallel to the distance vector  $R_{ij}$ . The symmetry of the crystal favors isotropic DMI, i.e.,  $|D_x| = |D_y|$  that stabilizes Bloch skyrmion.

### Stabilization of Neel skyrmion with interfacial DMI

In multi-layer systems, at the interface of a magnetic layer and a heavy metal layer, the inversion symmetry is broken automatically, resulting in a finite DMI in the system. The DMI energy is expressed as

$$H_{Interface} = \int D(m_x \frac{\partial m_z}{\partial x} - m_z \frac{\partial m_x}{\partial x} + m_y \frac{\partial m_z}{\partial y} - m_z \frac{\partial m_y}{\partial y}) dV. \quad (1.10)$$

This type of DMI stabilizes Neel skyrmions. The schematic of the DM vector and corresponding spin texture of Neel skyrmion are shown in Figs. 1.4 (c) and (d). The DM vector  $D_x$  and  $D_y$  lie perpendicular to the vector  $R_{ij}$ , and the magnitude of DM vector is equal (i.e.  $|D_x| = |D_y|$ ).

### Stabilization of antiskyrmion with anisotropic DMI

In addition to isotropic (i.e  $|D_x| = |D_y|$ ) DMI, anisotropic DMI  $|D_x| = -|D_y|$  is observed in  $D_{2d}$  and  $S_4$  symmetry crystal systems [1, 62]. The DMI energy for this case can be expressed as

$$H_{aniso} = \int D(m_x \frac{\partial m_z}{\partial x} - m_z \frac{\partial m_x}{\partial x} - m_y \frac{\partial m_z}{\partial y} + m_z \frac{\partial m_y}{\partial y}) dV. \quad (1.11)$$

The schematic of the DM vector and the corresponding antiskyrmion spin texture is shown in Figs. 1.4 (e) and (f). The DM vector  $D_x$  is perpendicular to the vector  $R_{ij}$  and rotates anticlockwise with respect to  $R_{ij}$ . In contrast,  $D_y$  is perpendicular to the vector  $R_{ij}$  and rotates clockwise with respect to  $R_{ij}$ .

This opposite sign of the DM vector originates due to the special symmetry of the system with the presence of non-magnetic atoms above and below the magnetic atomic layers. The anisotropic nature of DMI forms different chirality in different crystallographic directions, as marked by the red and black dashed boxes in Fig. 1.4 (f). In  $D_{2d}$  symmetric materials, the helical modulation propagates along  $[100]$  and  $[010]$  directions [black dashed area], while the cycloid modulation propagates along  $[110]$  and  $[\bar{1}\bar{1}0]$  directions [red dashed area].

## 1.4 Experimental observation of Skyrmion/Antiskyrmion

### 1.4.1 Observation of Skyrmion

The experimental observation of magnetic skyrmions has been realized using different microscopic probes both in momentum and real space. In 2009, small-angle neutron scattering experiment (SANS) experiment was utilized for the observation of magnetic skyrmions in the B20 crystal MnSi [25]. The SANS experiment provides the modulation of magnetization in momentum space, where six intensity spots were observed, which indicate the modulation of magnetization along three directions that confirms the formation of skyrmion lattice [Fig. 1.5 (a)]. The formation of skyrmion texture is understood by the superposition of three single  $\vec{Q}$  helices. These three helices propagate in a plane perpendicular to the direction of the external field, and the  $\vec{Q}$  vector makes an angle  $120^\circ$  with each other. Hence the skyrmion texture can be interpreted as a three Q state, which is different compared to the single Q helical or conical spin texture. The skyrmion phase in the case of MnSi is found in a narrow temperature-field region near the magnetic ordering temperature ( $T_C$ ). The phase diagram of MnSi is shown in Fig. 1.5 (b). The low-field helical spin texture

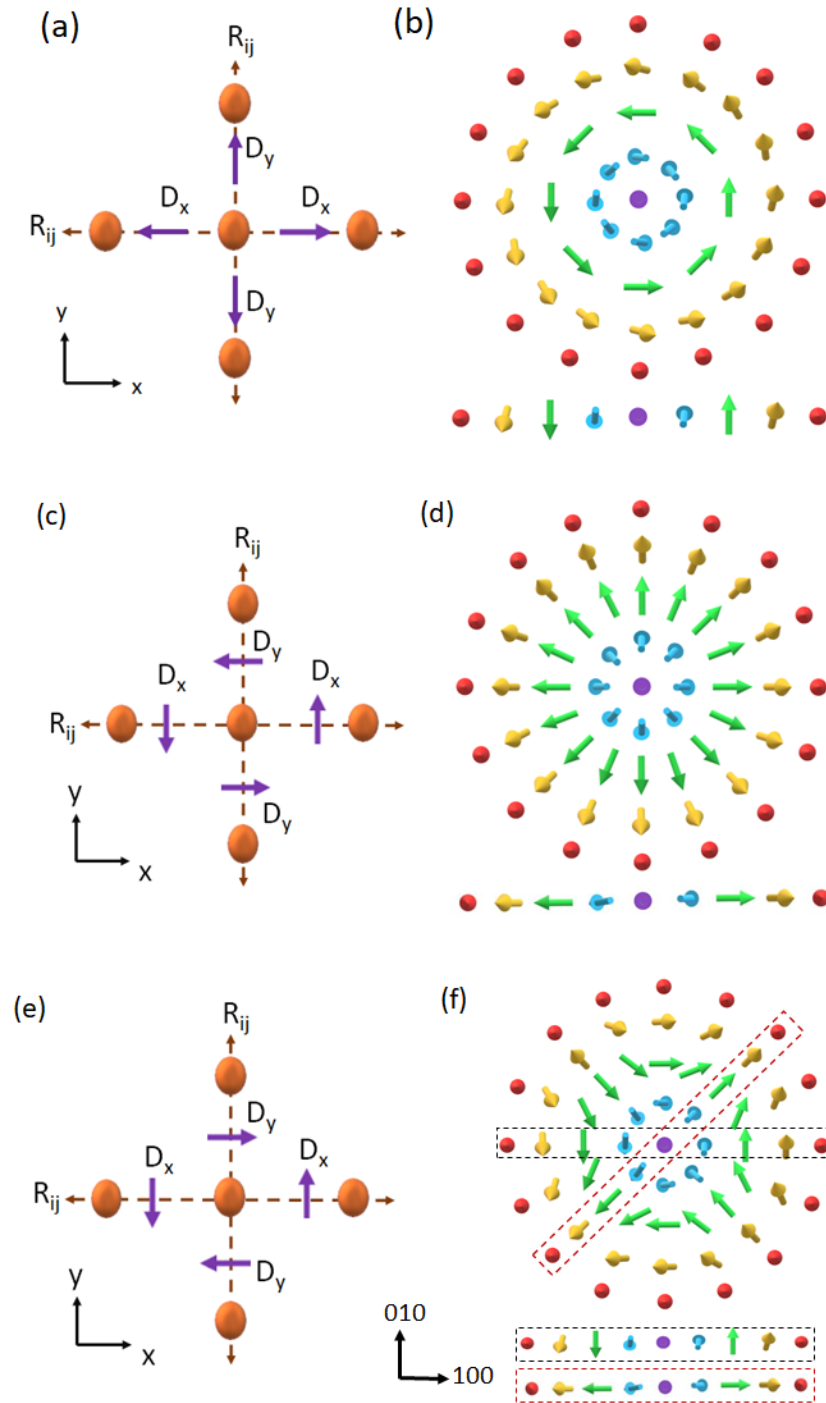


Figure 1.4: Schematic illustration of DM vectors and their resulting spin configurations. (a)-(b) Orientation of bulk DM vector and corresponding Bloch skyrmion, respectively. (c)-(d) Interface DM vector and corresponding Neel skyrmion, respectively. (e)-(f) Anisotropic DM vector and antiskyrmion spin structure. The lower panels in (b, d, f) show the spin modulations present in different spin textures.

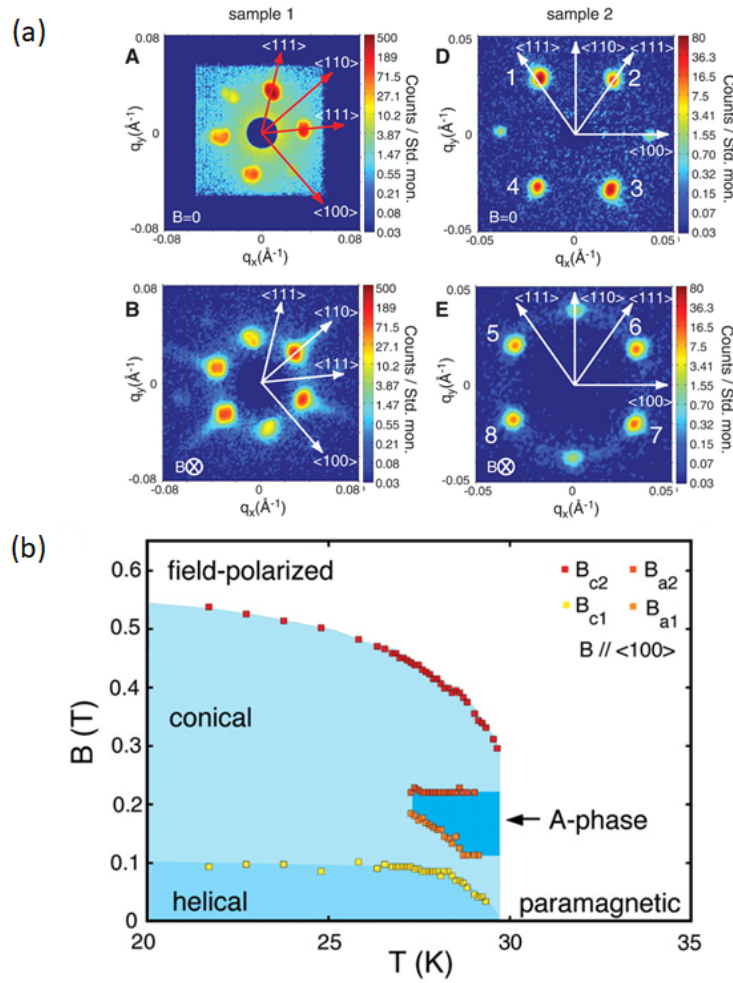


Figure 1.5: First experimental observation of magnetic skyrmion in MnSi. (a) The intensity profile of the magnetic skyrmions phase taken using Small Angle Neutron Scattering (SANS). (b) Temperature-field phase diagram of MnSi. [25].

transforms into magnetic skyrmions with the application of higher magnetic fields, indicated by the A phase. Further, increasing the magnetic field stabilizes the conical and field-polarized states. After a year of this pioneering discovery of magnetic skyrmions in MnSi, a research group from Japan directly visualizes the magnetic skyrmions in another B20 symmetry crystal system  $\text{Fe}_{0.5}\text{Co}_{0.5}\text{Si}$  utilizing real-space technique Lorentz Transmission Electron Microscopy (LTEM) [65]. Figure 1.6 (a) shows the LTEM images of both helical and skyrmion phases at lower fields. As the field increases, only the skyrmion lattice gets stabilized [Fig. 1.6 (b)]. A further increase in the field starts annihilating the skyrmions, before the field-polarized

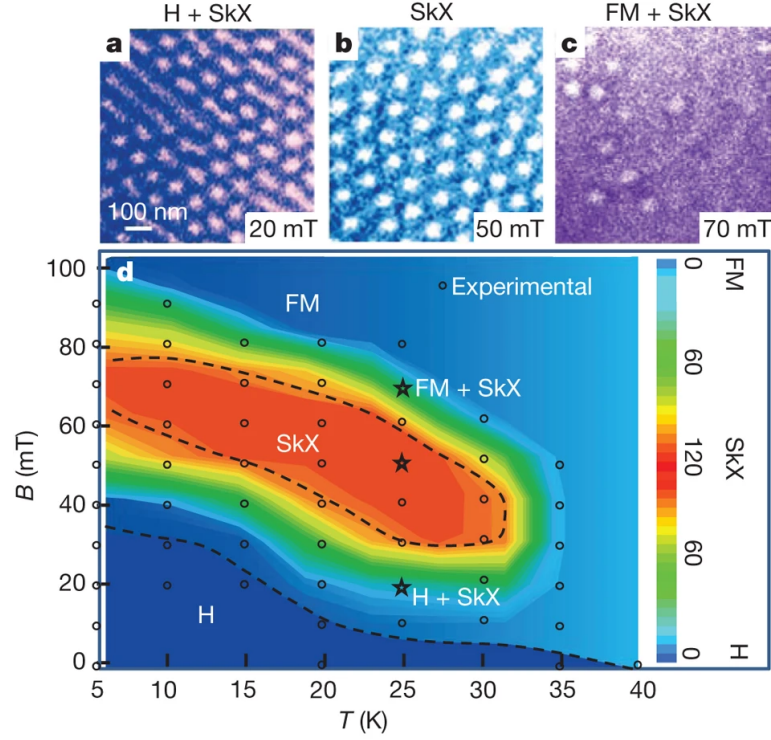


Figure 1.6: Real-space observation of magnetic skyrmion lattice. (a) At low field, helical and skyrmion states are present. (b) At a high field, skyrmion lattice emerges. (c) With increasing the field ferromagnetic state starts to emerge. (d) Temperature-field phase diagram of  $\text{Fe}_{0.5}\text{Co}_{0.5}\text{Si}$  [65].

state starts to appear [Fig. 1.6 (c)]. Figure 1.6 (d) shows the phase diagram of  $\text{Fe}_{0.5}\text{Co}_{0.5}\text{Si}$  drawn from the LTEM measurements. In this system, the skyrmion phase exists in a much wider temperature-field range compared to  $\text{MnSi}$ . In continuation, the magnetic skyrmion phase is observed in several non-centrosymmetric materials, such as in  $\text{FeGe}$  [27],  $\text{MnGe}$  [66],  $\text{Cu}_2\text{OSeO}_3$  [54], and  $\text{Co}_8\text{Zn}_9\text{Mn}_3$  [67].

Apart from the observation of Bloch skyrmions in several bulk materials, Neel skyrmions are also found in multi-layer systems. In heterostructure systems, the induced DMI due to the broken inversion symmetry at the interface stabilizes the Neel skyrmions. The existence of Neel skyrmions are found for the first time in the  $\text{Fe}/\text{Ir}$  system using scanning tunneling electron microscopy (STEM) [47]. Subsequently, Neel skyrmions are observed in several other heterostructure systems, e.g.  $\text{PdFe}/\text{Ir}$  [48],  $\text{Ta}/\text{CoFeB}/\text{TaO}_x$  [68],  $\text{Ir}/\text{Fe}/\text{Co}/\text{Pt}$  [69],  $\text{Co}/\text{Pd}$  [70],  $\text{Fe}/\text{Ni}/\text{Cu}/\text{Ni}/\text{Cu}$  [71]. Some bulk materials such as  $\text{GaV}_4\text{S}_8$  [50],  $\text{MnPtGa}$  [51], and in  $\text{Cr}_{1+\delta}\text{Te}_2$  [52] also

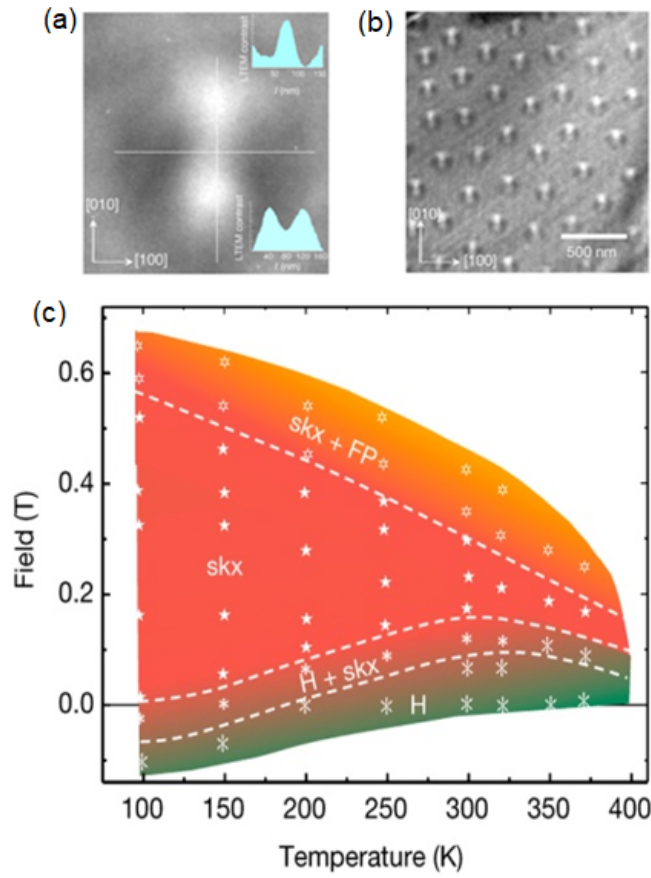


Figure 1.7: Observation of antiskyrmion. (a) LTEM contrast of an antiskyrmion. (b) LTEM image of antiskyrmion lattice. (c) Temperature- Field phase diagram of  $\text{Mn}_{1.4}\text{PtSn}$  constructed using LTEM measurements. [1]

hosts Neel skyrmions.

### 1.4.2 Observation of Antiskyrmion

In addition to the Bloch and Neel types of skyrmions, various other distinct types of topological spin textures are also predicted. In 2017, the existence of an antiskyrmion lattice was realized in the  $D_{2d}$  symmetric crystal  $\text{Mn}_{1.4}\text{Pt}(\text{Pd})\text{Sn}$  system using LTEM technique [shown in Fig. 1.7] [1]. The  $\text{Mn}_{1.4}\text{Pt}(\text{Pd})\text{Sn}$  system crystallizes in a tetragonal structure with space group  $\bar{I}42m$ . The Curie temperatures for  $\text{Mn}_{1.4}\text{PtSn}$  and  $\text{Mn}_{1.4}\text{Pt}_{0.9}\text{Pd}_{0.1}\text{Sn}$  are found to be about 395 K and 375 K, respectively. At low temperatures (at 155 K for  $\text{Mn}_{1.4}\text{PtSn}$  and at 130 K for

$\text{Mn}_{1.4}\text{Pt}_{0.9}\text{Pd}_{0.1}\text{Sn}$ ), a spin reorientation transition is observed. The  $D_{2d}$  crystal symmetry and large spin-orbit coupling (SOC) induced anisotropic DMI favors antiskyrmion formation in this system. The competing exchange interaction and DMI stabilize helical spin textures as the ground state. When the magnetic field is applied along [001] direction, the helical spin textures transform into antiskyrmions. The LTEM contrast of a single antiskyrmion and antiskyrmion lattice are shown in Figs. 1.7 (a)-(b). Unlike the B20 materials, in this case, the antiskyrmion phase stabilizes over a wide temperature-field range. Notably, the antiskyrmion phase exists above the room temperature up to 390 K, as shown in the  $H - T$  phase diagram Fig.1.7(c). The field range of the antiskyrmion phase becomes narrower at higher temperatures. The size of the antiskyrmion is found to be around 150 nm and remains the same over the temperature range. Later, the antiskyrmion phase is also found in another  $D_{2d}$  symmetric material  $\text{Mn}_2\text{Rh}_{0.95}\text{Ir}_{0.05}\text{Sn}$  [62], and in  $S_4$  symmetric material  $\text{Fe}_{1.9}\text{Ni}_{0.9}\text{Pd}_{0.2}\text{P}$  [57].

## 1.5 Magnetocaloric effect

The magnetocaloric effect (MCE) is a well-known phenomenon for its potential use in the magnetic refrigeration process. Two non-identical magnetic states with a different arrangement of spin textures can show different magnetic entropy. The change in magnetic entropy by going from one magnetic state to the other can be used to probe the magnetic state itself. For the present study, the measurement of MCE is being used for the identification of helical and antiskyrmion phases, which will be shown in Chapter 3. In the following, a brief introduction about the magnetocaloric effect is given.

The change in the temperature or magnetic entropy of a magnetic specimen under the application of a magnetic field is known as the magnetocaloric effect (MCE) [72, 73]. All magnetic materials show the magnetocaloric effect, and its intensity varies from system to system. The coupling between spin and the lattice gives rise to this effect. When a magnetic material is exposed to a magnetic field, its

spin degree of freedom is affected. This results in a change in the magnetic entropy. The entropy of a ferromagnetic substance has mainly three contributions, lattice entropy ( $S_l$ ), magnetic entropy  $S_M$  and electronic entropy  $S_e$ . The total entropy can be expressed as

$$S = S_e + S_M + S_l \quad (1.12)$$

The MCE is quantified as the change in magnetic entropy or temperature during two physical processes. The two physical processes of MCE are shown in Fig. 1.8. At constant temperature (isothermal process), when a magnetic field is applied, the randomly oriented spins are aligned along the field direction, making an ordered state. This ordered state has less magnetic entropy in comparison to the previous disorder state, leading to a decrease in both the magnetic entropy and the total entropy of the substance. In adiabatic conditions, the application of a magnetic field will align the spins along the field direction. This will decrease the magnetic entropy, but the total entropy remains the same due to the adiabatic condition. As a result of this, the temperature will increase. Experimentally two quantities can be measured to quantify the MCE, the first one is the change in temperature ( $T_{ad}$ ) under adiabatic conditions, and the second one is the change in magnetic entropy ( $S_M$ ) under isothermal conditions. The free energy of a magnetic system can be expressed as

$$F = U - TS - HM \quad (1.13)$$

where  $F$  represents the free energy,  $U$  is the internal energy,  $T$  is the temperature,  $S$  denotes the entropy,  $H$  and  $M$  represent the applied field and magnetization, respectively. The total differential of  $F$  can be written as

$$dF = dU - TdS - SdT - MdH - HdM. \quad (1.14)$$

Using the thermodynamic relation  $TdS = dU - HdM$  the  $dF$  will be

$$dF = -SdT - MdH. \quad (1.15)$$

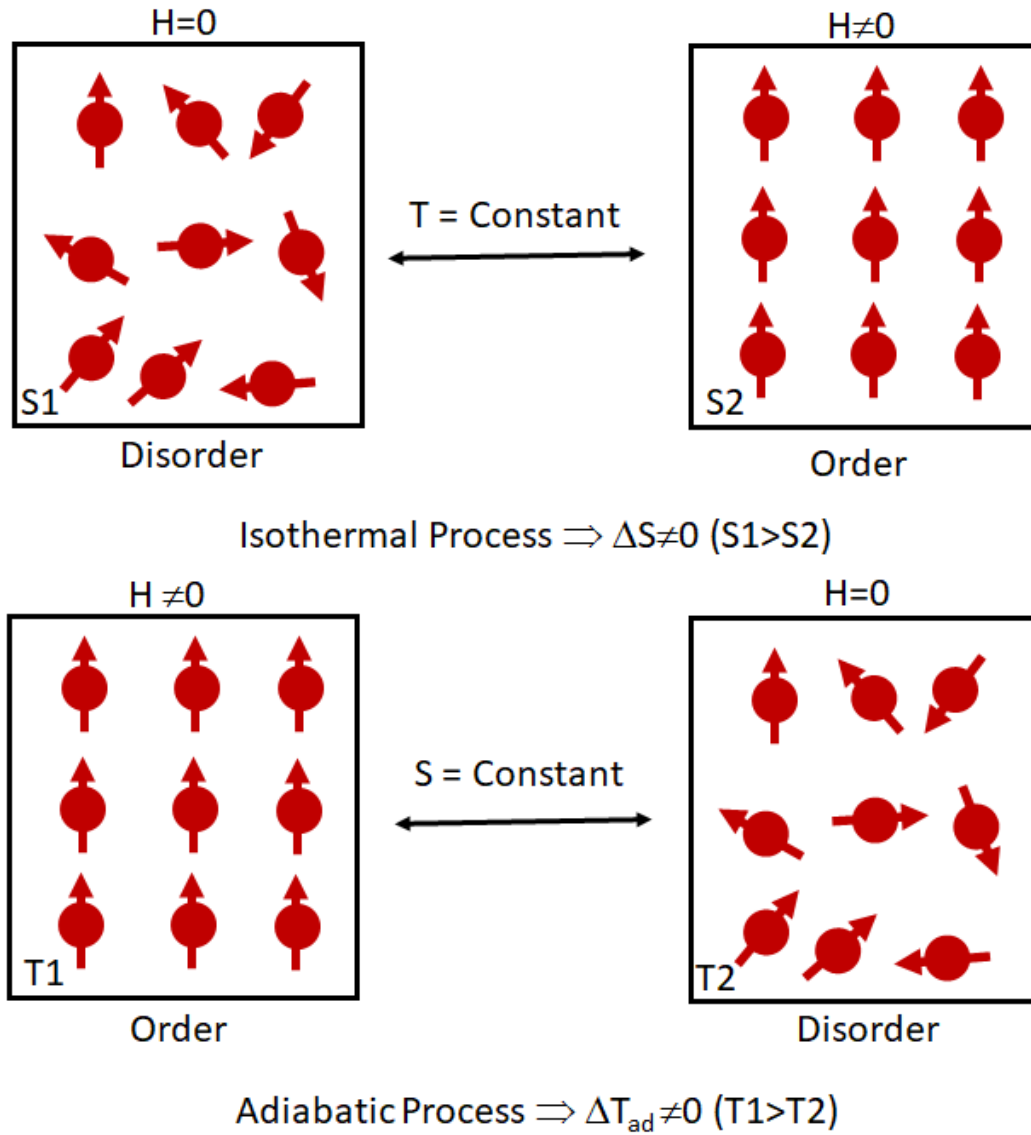


Figure 1.8: Schematic representation of Magnetocaloric effect under the magnetic field application. The application of a magnetic field under the isothermal process gives rise to magnetic entropy changes and in the adiabatic process the temperature of the substance changes.

Hence the entropy  $S$  and the magnetization  $M$  will be

$$S = - \left( \frac{\partial F}{\partial T} \right)_H \quad (1.16)$$

and

$$M = - \left( \frac{\partial F}{\partial H} \right)_T \quad (1.17)$$

The derivative of equations 1.16 and 1.17 with respect to  $H$  and  $T$ , respectively, gives the set of equations.

$$\left(\frac{\partial S}{\partial H}\right)_T = -\left(\frac{\partial}{\partial H}\left(\frac{\partial F}{\partial T}\right)_H\right)_T \quad (1.18)$$

$$\left(\frac{\partial M}{\partial T}\right)_H = -\left(\frac{\partial}{\partial T}\left(\frac{\partial F}{\partial H}\right)_T\right)_H \quad (1.19)$$

Using the thermodynamic relation  $\left(\frac{\partial}{\partial x}\left(\frac{\partial y}{\partial z}\right)_x\right)_z = \left(\frac{\partial}{\partial z}\left(\frac{\partial y}{\partial x}\right)_z\right)_x$ , the set of equations 1.18 and 1.19 gives Maxwell's equation

$$\left(\frac{\partial S}{\partial H}\right)_T = \left(\frac{\partial M}{\partial T}\right)_H \quad (1.20)$$

From Maxwell's equation 1.20, the expression of the magnetic entropy change can be written as

$$\Delta S_m = \int_0^H \left(\frac{\partial M}{\partial T}\right)_H dH. \quad (1.21)$$

Equation 1.21 is used to calculate the magnetic entropy change ( $\Delta S_M$ ) by measuring the magnetization. The magnetocaloric effect can be determined through isothermal magnetization measurements at constant temperature intervals, utilizing the following approximated equation.

$$\Delta S_m = \frac{1}{\Delta T} \left( \int_0^H M_2 dH - \int_0^H M_1 dH \right) \quad (1.22)$$

## 1.6 Electronic transport properties in magnetic systems

The advancement of the spintronics field needs more than the observation or characterization of different topological objects. To use these magnetic objects in real

devices, one requires to understand the basic electronic transport mechanism that they display, i.e., the interplay between the magnetization and conduction electrons in a magnetic system. The momentum space band topology and real-space spin textures lead to various intriguing transport phenomena, such as the Anomalous Hall effect (AHE) and the Topological Hall effect (THE). The study of AHE and THE yields valuable insights into the intrinsic magnetic structure of the materials. In the following, a discussion is focused on the underlying mechanism of anomalous Hall effect and topological Hall effect.

### 1.6.1 Anomalous Hall effect

In 1879, Edwin H. Hall [74] measured a transverse voltage when a current and magnetic field were applied perpendicular to each other in a conductor. The transverse voltage, known as the Hall voltage, appears perpendicular to both the applied current and magnetic field. The origin of the transverse voltage was understood in terms of the Lorentz force acting on charge carriers in the presence of the orthogonal magnetic field. This Hall effect phenomenon is known as the ordinary Hall effect, and the Hall resistivity is expressed as  $\rho_{xy} = R_0 H$ , where  $R_0$  is the Hall coefficient, which is inversely proportional to the carrier density. This simple measurement gives the carrier concentration and mobility of the materials.

Later, in 1881, Hall [75] performed the same experiment with a ferromagnetic material. This time, he found that the Hall resistivity is much larger compared to the non-magnetic specimen. Surprisingly, the Hall resistivity in this magnetic material follows the magnetization loop. Since the exact origin of this large Hall voltage was not known at that time, it was termed as anomalous Hall effect. After the discovery of anomalous Hall effect, a large number of theoretical and experimental studies were carried out. It was found that the anomalous Hall resistivity depends on the magnetization of the system, and an empirical equation for the total Hall resistivity

of a ferromagnetic system was given as

$$\rho_{xy} = \rho_{xy}^O + \rho_{xy}^A = R_0 H + R_s M. \quad (1.23)$$

The first term in the above equation represents the ordinary Hall effect, and the second term corresponds to the anomalous Hall effect, where  $R_s$  denotes the anomalous Hall coefficient. Despite extensive investigations of the anomalous Hall effect in various systems, its underlying fundamental physics remains obscure for a long time. Recent studies have suggested that there are mainly two different mechanisms that drive the anomalous Hall effect, the intrinsic mechanism and the extrinsic mechanism. The details of intrinsic and extrinsic mechanisms is discussed in the following section.

### 1.6.1.1 Intrinsic mechanism

In 1954, Karplus and Luttinger [76] proposed the intrinsic mechanism. They show that the electrons acquire an anomalous velocity under the influence of an external electric field. The anomalous velocity that intrinsically arises from the band structure of the system exhibits opposite directions for electrons with up and down spins, as depicted in Fig. 1.9. The intrinsic contribution is a scattering independent mechanism, as it is related to the band topology of the system. In current exploration, the intrinsic contribution of the AHE is understood in connection with the momentum space Berry curvature [77, 78, 79, 80]. When an electron moves in a periodic potential, its eigenstate evolves adiabatically over time. The  $n^{th}$  eigenstate at time  $t=0$  changes to the  $n^{th}$  eigenstate at time  $t=t$  with acquiring an additional phase factor. The evolved eigenstate at time  $t$  can be written as

$$\Psi_n(t) = e^{i[\theta_n(t)+\gamma_n(t)]}\Psi_n(0) \quad (1.24)$$

where  $\gamma_n(t) = i \int_0^t \langle \Psi_n(t) | \frac{\partial}{\partial t} | \Psi_n(t) \rangle dt$  is the geometrical phase and  $\theta_n(t) = -\frac{1}{\hbar} \int_0^t E_n(t) dt$  is the dynamical phase. The geometrical phase is known as the Berry phase where

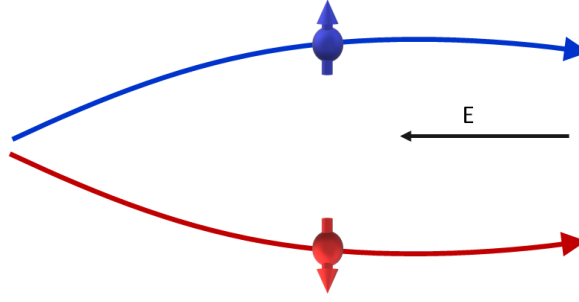


Figure 1.9: Schematic illustration of intrinsic deflection.

the Berry curvature is given by

$$\Omega_n(k) = \nabla_k \times b_n(k). \quad (1.25)$$

Here  $b_n(k) = i\langle\Psi_n(k)|\frac{\partial}{\partial k}|\Psi_n(k)\rangle$  is the Berry connection. The total Hall conductivity is calculated using the simplified Kubo formula

$$\sigma_{xy}^A = -\frac{e^2}{\hbar} \sum_n \int \frac{dk}{(2\pi)^3} f(\epsilon_n) \Omega_n(k). \quad (1.26)$$

The Berry curvature occupied by the conduction electron over the Brillouin zone gives the total anomalous Hall conductivity. The value of the total Berry curvature over the Brillouin zone depends on the symmetry of the system. For the system with preserved time-reversal symmetry, the  $\Omega_n(k) = -\Omega_n(-k)$ , and for the inversion symmetry invariant system  $\Omega_n(k) = \Omega_n(-k)$ . Hence for the system where both time-reversal and spatial-inversion symmetries are present, the total Berry curvature will be zero. If only spatial symmetry is broken, a finite Berry curvature at different points at the  $k$  space is present, and the total Berry curvature over the Brillouin zone is still zero. For the magnetic system, where the time-reversal symmetry is broken, a non-zero Berry curvature is present, as it is found in the case of Fe [81]. The Berry curvature-induced anomalous Hall effect is observed in several systems [82, 83, 84].

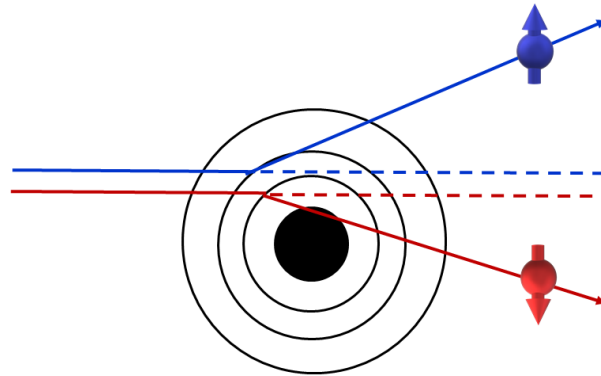


Figure 1.10: Schematic illustration of skew Scattering. The opposite spins are scattered asymmetrically at the impurity side.

### 1.6.1.2 Extrinsic mechanism

The extrinsic mechanism occurs due to the spin-dependent scattering of conduction electrons at the impurity side. There are two kinds of extrinsic scattering events; skew scattering and side jump.

#### Skew scattering

The skew scattering mechanism proposed by Smith [85] corresponds to the asymmetric scattering of conduction electrons by the charged impurities within a crystal. In the skew scattering process, the electrons are scattered in opposite directions depending on their spin, as depicted in the schematic diagram Fig. 1.10. When an electron approaches a charged impurity center, it experiences an electric field. In the presence of spin-orbit interaction (SOI), this electric field becomes the magnetic field in the electron's frame of reference. The direction of this magnetic field is perpendicular to both the velocity and the electric field. The presence of a magnetic field induces Zeeman energy, which exerts opposing forces on electrons with up and down spins. As a result, the up and down spins electrons are deflected in opposite directions. The skew scattering contribution depends on the lifetime ( $\tau$ ) of the Bloch state. Thus it dominates in a perfect crystal [86, 87].

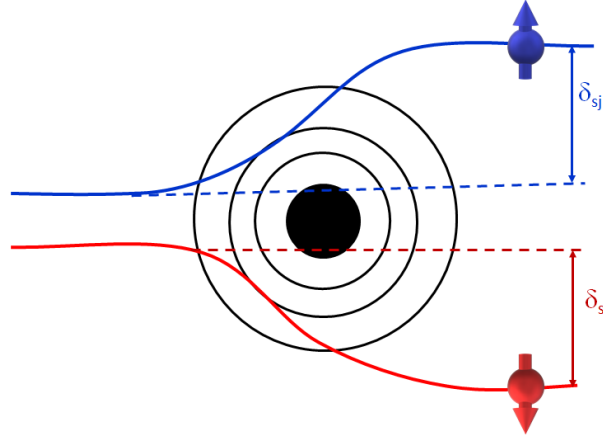


Figure 1.11: Schematic illustration of side jump scattering. The up and down spin electrons shift their trajectories in opposite directions at the impurity side.

### Side Jump mechanism

In the side jump mechanism, the electron trajectory shifts laterally at the impurity side, as depicted in Fig.1.11. It is a spin-dependent scattering in which the up and down spin electrons shift their trajectories in opposite directions. The transverse displacement  $\delta_{sj}$  is estimated to be  $\approx 10^{-10}$  to  $10^{-11}$  m. The side jump mechanism is mainly observed in multilayer systems where surface and interfacial scattering plays a crucial role [88, 89]. In bulk ferromagnetic systems, the side jump contribution is negligibly small [90].

#### 1.6.1.3 Universal scaling of AHE

Efforts have been made both theoretically and experimentally to understand the underlying mechanism of the anomalous Hall effect in different materials. It is found that in the case of a real system, both the intrinsic and extrinsic mechanisms are present simultaneously. Experimentally, it is a great challenge to distinguish these different mechanisms. The longitudinal conductivity ( $\sigma_{xx}$ ) of a material can be connected with the lifetime  $\tau$  by the relation  $\sigma_{xx} \propto \tau$ . The dissipationless intrinsic mechanism does not depend on the transport lifetime  $\tau$  of the Bloch state i.e.,  $\sigma_{xy}^A \propto \tau^0$  [91]. Hence, the intrinsic anomalous Hall resistivity can be written as  $\rho_{xy}^{A-int} \propto \rho_{xx}^2$  (as  $\sigma_{xy}^A = \frac{\rho_{xy}^A}{\rho_{xx}^2}$ ), where  $\rho_{xx}$  is the longitudinal resistivity. For skew scattering

contribution, the anomalous Hall conductivity is proportional to the lifetime, i.e.,  $\sigma_{xy}^A \propto \tau$ . Therefore, the anomalous Hall resistivity arising from the skew scattering can be expressed as  $\rho_{xy}^{A-skew} \propto \rho_{xx}$ . It is found that for side jump, the scaling relation is  $\rho_{xy}^{A-int} \propto \rho_{xx}^2$ . These relationships can be combined into a power law relation

$$\rho_{xy}^A \propto \rho_{xx}^\alpha. \quad (1.27)$$

Where  $\alpha$  is the scaling factor used to determine the dominant mechanism of AHE. For  $\alpha = 1$ , the dominant mechanism is skew scattering, and with  $\alpha = 2$ , the dominant mechanism is intrinsic or side jump. The total anomalous Hall resistivity, including intrinsic and extrinsic contribution, can be written as

$$\rho_{xy}^A = a\rho_{xx} + b\rho_{xx}^2 \quad (1.28)$$

Later, Tian et al. [92] modified the relation and presented a new scaling relation

$$\rho_{xy}^A = a\rho_{xx0} + \beta\rho_{xx0}^2 + b\rho_{xx}^2 \quad (1.29)$$

where  $\rho_{xx0}$  is the residual resistivity. The first term in equ. 1.29 represents the skew scattering contribution, the second term accounts for the side jump contribution, and the last term stands for the intrinsic contribution. Ignoring the side jump contribution the relation simplifies into

$$\rho_{xy}^A = a\rho_{xx0} + b\rho_{xx}^2. \quad (1.30)$$

Which has been used extensively for various systems [93, 94, 95, 96]. A large number of studies in different materials suggest that there exists mainly three different conductivity regions (i) a high conductivity region  $\sigma_{xx} > 10^6(\Omega - cm)^{-1}$  where skew scattering is dominant, (ii) an intermediate conductivity region  $10^4 < \sigma_{xx} < 10^6(\Omega - cm)^{-1}$  where intrinsic contribution dominates, and (iii) a bad metal region

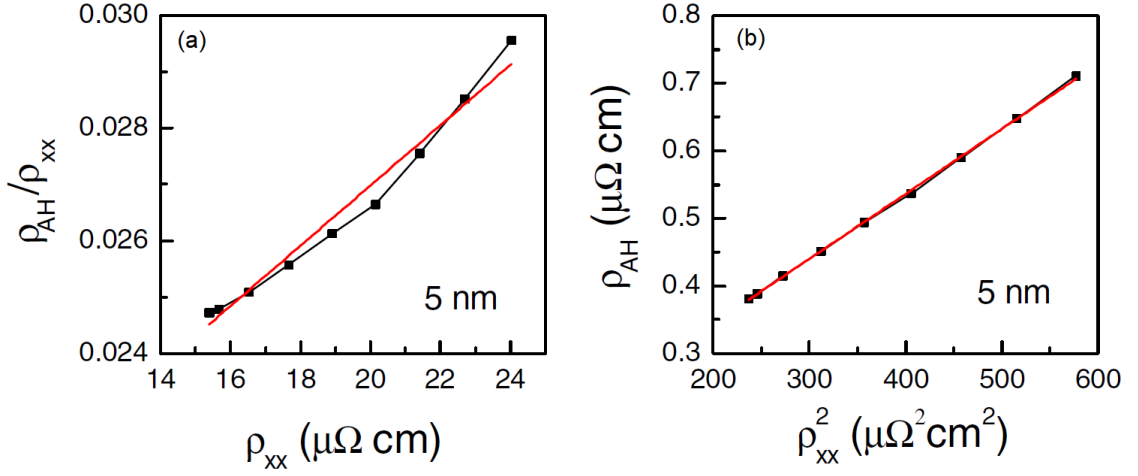


Figure 1.12: Scaling relation of AHE of Fe thin films. (a) Black squares are experimental data and red line is the linear fitting using the relation  $\frac{\rho_{AH}}{\rho_{xx}}$  vs  $\rho_{xx}$  (old scaling). (c) Linear fitting for the relation  $\rho_{AH}$  vs  $\rho_{xx}^2$  (new scaling) [92].

$\sigma_{xx} < 10^4 (\Omega - cm)^{-1}$  where  $\sigma_{xy}^A$  decreases with  $\sigma_{xx}$ .

In the following, recent experimental discoveries showing different mechanisms of the anomalous Hall effect are presented. In 2009, Tian et al. [92] presented a new scaling relation equ.1.29 in place of equ.1.28. In epitaxial films of Fe, they observed that the old scaling relation equ.1.28 [Fig. 1.12 (a)] does not give good fitting, whereas the modified new scaling relation equ.1.29 fitted well, shown in Fig. 1.12 (b). From their fitting, they extracted different contributions of AHE. Wang et al. [82] discovered the presence of a large anomalous Hall effect in  $\text{Co}_3\text{Sn}_2\text{S}_2$ , as shown in Fig. 1.13 (a). Figure 1.13 (b) depicts the magnetization of the sample. Using the power law equ.1.27 and scaling relation [Figs. 1.13 (c)- (d)] they confirm that the main contribution of the anomalous Hall effect arises from the intrinsic mechanism.

Shiomi et al. [86] show the presence of skew scattering dominated anomalous Hall effect in Co-doped Fe system. They observe the existence of skew scattering mechanism at low temperatures. Below 100 K, the conductivity of Co-doped Fe is in the range of clean limit ( $\sigma_{xx} > 10^6 (\Omega - cm)^{-1}$ ), as shown in Fig. 1.14 (a). In this region, the Hall conductivity  $\sigma_{xy}^A$  decreases with temperature, which confirms the presence of skew scattering mechanism [Fig. 1.14 (b)]. At high temperatures, the conductivity  $\sigma_{xx}$  falls in the intermediate region where the Hall conductivity

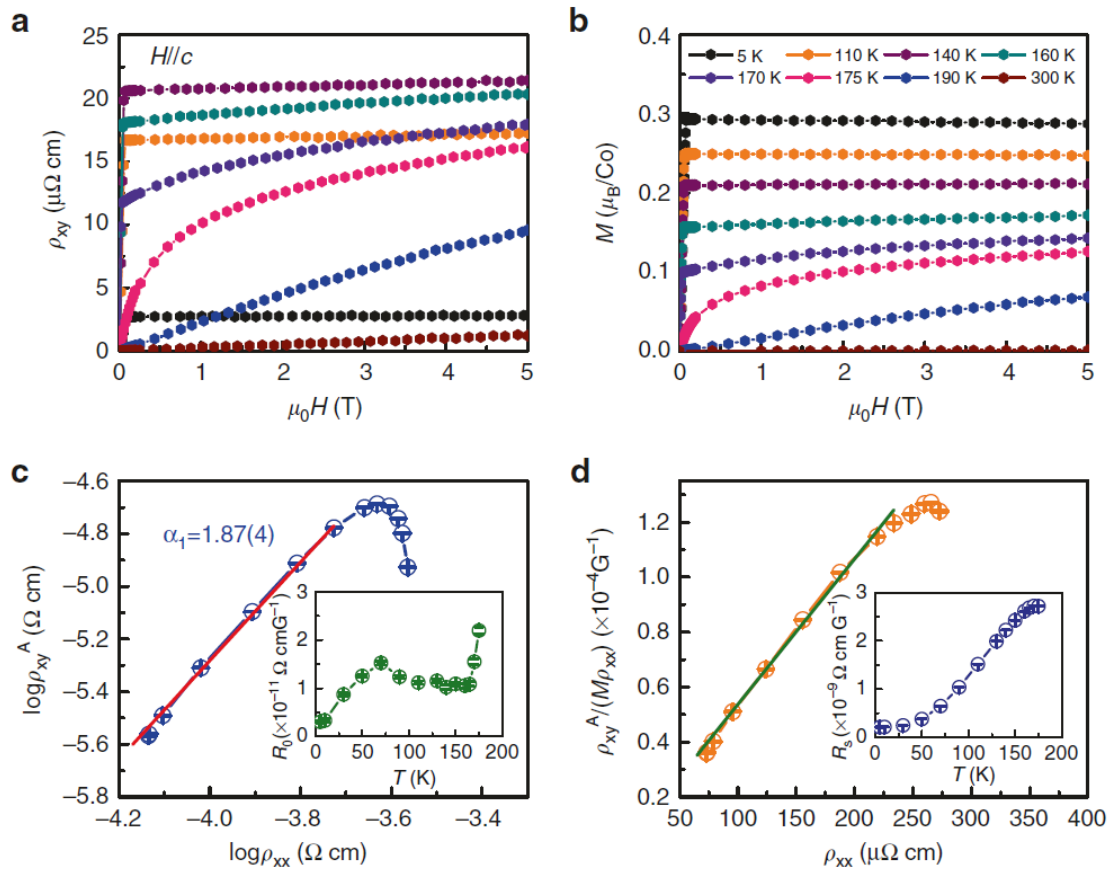


Figure 1.13: Anomalous Hall effect in  $\text{Co}_3\text{Sn}_2\text{S}_2$ . (a) Field-dependent Hall resistivity at several temperatures. (b) Field-dependent magnetization at various temperatures. (c) Plot of  $\log \rho_{xy}^A$  vs  $\log \rho_{xy}$ . (d) Plot of  $\frac{\rho_{xy}^A}{M \rho_{xx}}$  vs  $\rho_{xx}$  [82].

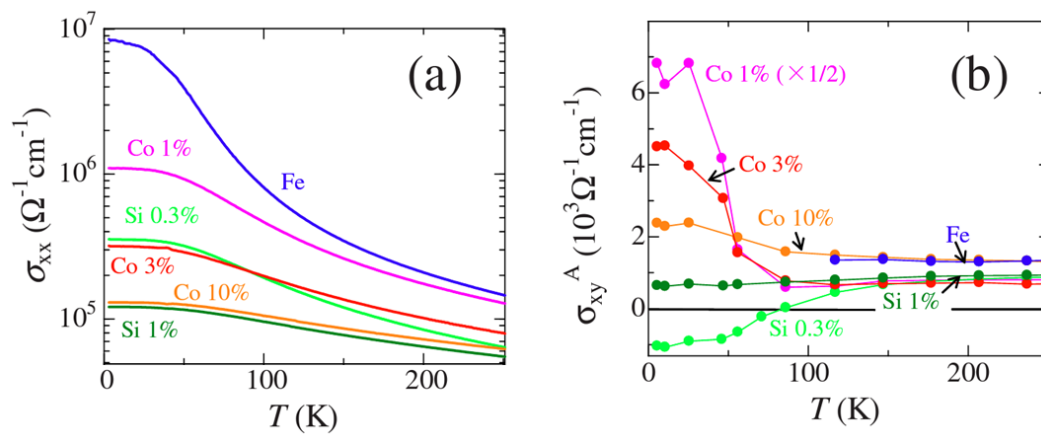


Figure 1.14: Observation of skew scattering dominant AHE in Co-doped Fe bulk system. (a) Temperature-dependent normal conductivity ( $\sigma_{xx}$ ). (b) Temperature-dependent Hall conductivity ( $\sigma_{xy}^A$ ). [86].

does not change with the temperature, confirming the intrinsic nature of the AHE. Although numerous studies have been conducted on the anomalous Hall effect, the experimental manipulation of distinct mechanisms remains absent within the existing literature.

### 1.6.2 Topological Hall effect

Non-trivial spin texture, such as magnetic skyrmion/antiskyrmion, can exhibit an extra component of Hall voltage in addition to the normal and anomalous Hall signals, known as topological Hall effect. The THE possesses a significant importance as it is directly associated with real-space spin textures. The AHE occurs due to the momentum space Berry phase, whereas the topological Hall effect originates from the real-space Berry phase. When an electron moves through a non-trivial spin texture, such as skyrmion/antiskyrmion, it adiabatically couples with the local magnetization, leading to the acquisition of a quantum mechanical Berry phase in real space. The acquired Berry phase is proportional to the scalar spin chirality (SSC),  $\chi = \sum S_i \cdot (S_j \times S_k)$ . The SSC is defined as the scalar product of three spins corresponding to the solid angle subtended by these spins  $(S_i, S_j, S_k)$  on a unit sphere. In the case of a coplanar spin arrangement, the SSC is zero. For non-coplanar arrangement, the presence of a finite scalar spin chirality induces the Berry phase, which acts as a fictitious magnetic field and deflects the charge carriers. The induced fictitious magnetic field during the movement of the conduction electrons through a smoothly varying spin texture, such as skyrmion/antiskyrmion can be written as,

$$B_{eff} = \frac{\phi_0}{4\pi} \mathbf{m}(\mathbf{r}) \cdot \left( \frac{\partial \mathbf{m}(\mathbf{r})}{\partial x} \times \frac{\partial \mathbf{m}(\mathbf{r})}{\partial y} \right) \quad (1.31)$$

Here  $\phi_0 = \frac{hc}{e}$  is the quantum of flux, and  $\mathbf{m}(\mathbf{r})$  is the local unit magnetization vector. The surface integral of the  $B_{eff}$  over a surface  $S$  which encloses the spin textures, gives the total magnetic flux. The magnetic flux is given by

$$\phi_i = \int_S B_{eff} dS. \quad (1.32)$$

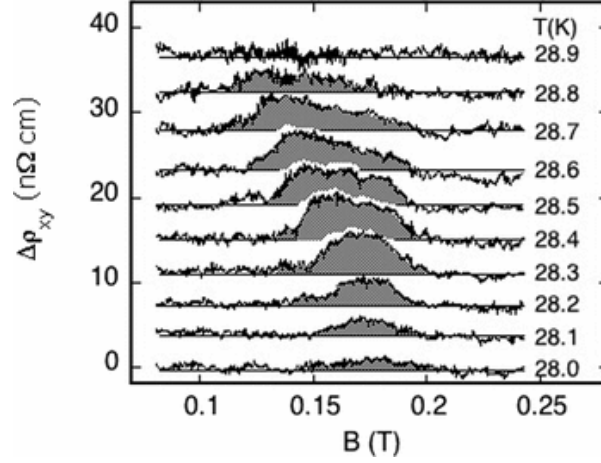


Figure 1.15: Topological Hall resistivity in the skyrmion phase of MnSi [97].

The skyrmion/antiskyrmion spin textures span over the unit sphere. Hence the total magnetic flux induced by a single skyrmion/antiskyrmion is  $\phi_i = \pm\phi_0$ . The effective emergent magnetic field induced by a single skyrmion/antiskyrmion is  $B_{eff} = \pm\frac{\phi_0}{a_{sk}^2}$ , where  $a_{sk}$  is the size of the skyrmion/antiskyrmion. The emergent field varies inversely proportional to the size of the spin textures. The topological Hall resistivity is given by  $\rho_{xy}^T = PR_0B_{eff}$ , where  $P$  is the spin polarization,  $R_0$  is the normal Hall coefficient.

The topological Hall effect has been found in various skyrmion host systems, where the magnitude of THE depends on the size of the skyrmion. In MnSi, the topological Hall resistivity in the skyrmion phase has been found to be  $\rho_{xy}^T = 4 n\Omega$  [ Shown in Fig. 1.15]. The size of the skyrmions is  $18 nm$ , and the emergent magnetic field is about  $2.5 T$ . In the case of MnSi thin films, the topological Hall feature has been observed in the Hall resistivity data [shown in Fig 1.16]. Figures 1.16 (a)- (d) show the Hall resistivity data with the application of an oblique field at several temperatures. The measurements set up is shown in the inset of Fig. 1.16 (a). The thick lines in Fig. 1.16 are the experimental data, and the thin lines are the fitting. The mismatch between these two lines is the topological Hall effect. With increasing the tilting angle, the topological Hall voltage decreases.

Recently, at room temperature, a large topological Hall effect is observed in  $D_{2d}$  symmetric Mn-Ni-Ga Heusler alloy [2]. The Mn-Ni-Ga based compounds un-

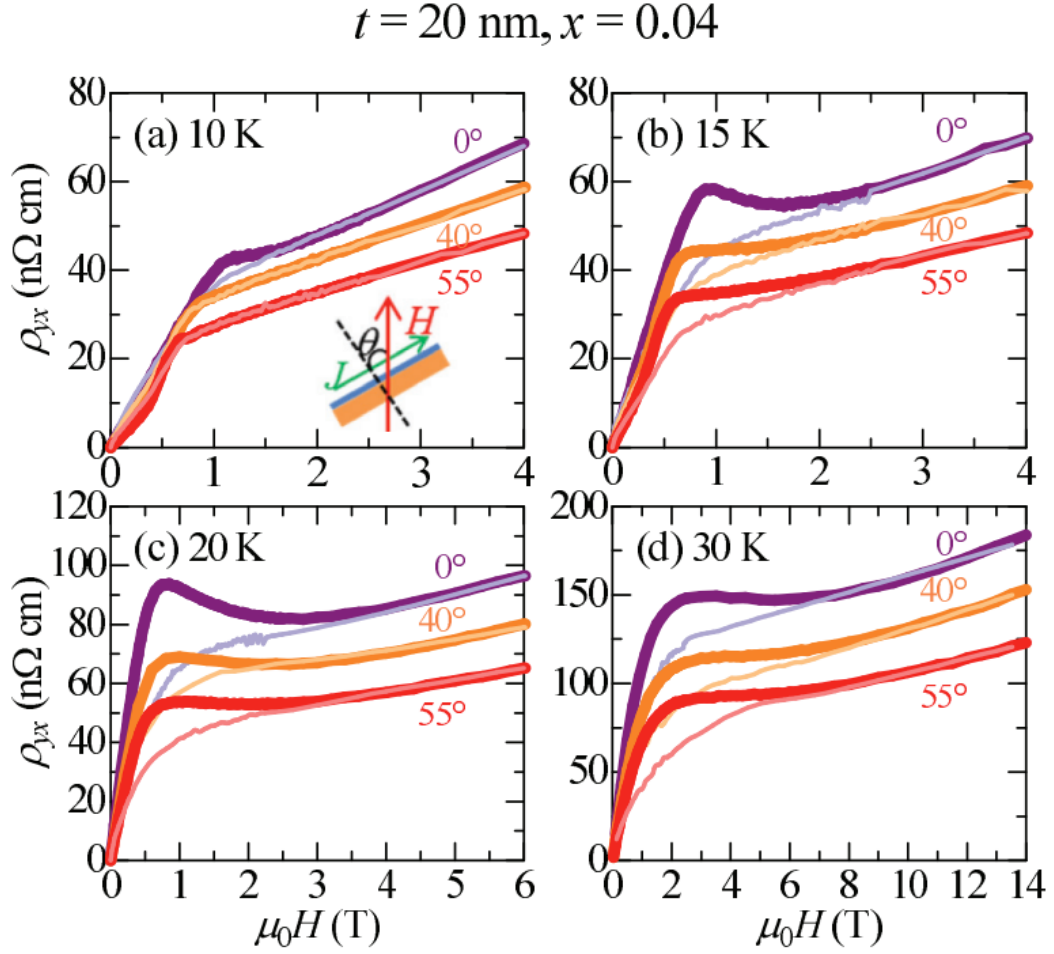


Figure 1.16: (a)-(d) Field-variation of Hall resistivity at several temperatures at an applied tilted magnetic field. Thick lines represent the experimental data and the thin lines represent the fitting. [98].

dergo from a high-temperature austenite cubic phase to a low-temperature tetragonal phase with space group  $\bar{1}4m2$ , which is non-centrosymmetric in nature [2]. The symmetry favors the stabilization of antiskyrmion type of spin textures in this series of samples. Most importantly, the Curie temperature for these materials is above 600 K. The observation of large topological Hall and ac susceptibility study confirm the presence of antiskyrmions in this system [2]. Figures 1.17 (a) and (b) show the topological Hall effect observed in bulk polycrystalline  $\text{Mn}_2\text{NiGa}$  and  $\text{Mn}_{2.1}\text{NiGa}_{0.9}$ , respectively [3]. The magnitude of topological Hall signal in these compounds is more than  $100 \text{ n}\Omega - \text{cm}$ , signaling towards small skyrmion size of about 10-20 nm.

The temperature-field phase diagram constructed using the THE measurements

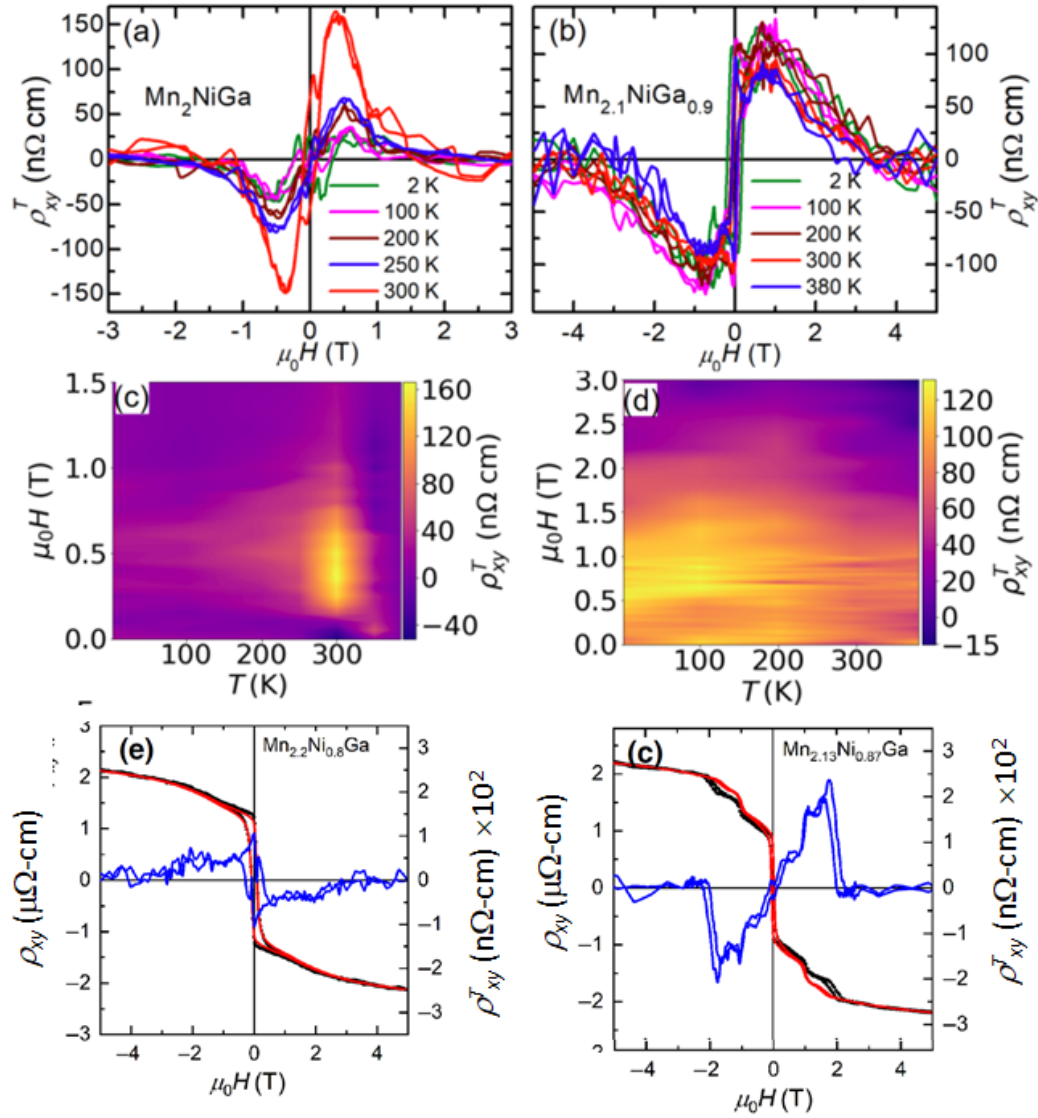


Figure 1.17: Topological Hall resistivity of Mn-Ni-Ga Heusler compound. (a)-(b) Field variation of topological Hall resistivity ( $\rho_{xy}^T$ ) for  $\text{Mn}_2\text{NiGa}$  and  $\text{Mn}_{2.1}\text{NiGa}_{0.9}$ , respectively (c)-(d) Temperature-field phase diagram of  $\text{Mn}_2\text{NiGa}$  and  $\text{Mn}_{2.1}\text{NiGa}_{0.9}$ . (e)-(f) Field variation of topological Hall resistivity ( $\rho_{xy}^T$ ) for  $\text{Mn}_{2+x}\text{Ni}_{1-x}\text{Ga}$  (with  $x=0.1,0.3$ ) [2, 3].

is shown in Figs. 1.17 (c)- (d) for  $\text{Mn}_2\text{NiGa}$  and  $\text{Mn}_{2.1}\text{NiGa}_{0.9}$ , respectively. Both the samples show THE over a wide temperature-field range. In the Ni deficiency compound of the  $\text{Mn}_{2+x}\text{Ni}_{1-x}\text{Ga}$  system, a similar type of topological Hall is observed with a much larger value [3]. Figures 1.17 (e)-(f) show the Hall resistivity and extracted topological Hall effect for  $\text{Mn}_{2+x}\text{Ni}_{1-x}\text{Ga}$  (with  $x=0.1,0.3$ ). The measured Hall resistivity is represented by the black curves, while the red lines depict

the calculated Hall resistivity. The extracted topological Hall effect is indicated by the blue curves.

The topological Hall effect can be interpreted as the electrical signature of skyrmion/antiskyrmion textures. Hence the observation of topological Hall signal has been widely used to identify topological objects. Using the THE the smaller size of magnetic skyrmion/antiskyrmion can be identified over a large temperature-field range. Furthermore, the THE gives information about the quantize emergent magnetic flux associated with the complex spin textures, which is not accessible in other techniques used to detect the skyrmion phase. From the application point of view, the electrical signature of magnetic skyrmion/antiskyrmion can find utility in memory devices as a readout component, as well as in probabilistic and neuromorphic computing.

## 1.7 Heusler compounds

The realization of spin-based devices strongly relies on various parameters, such as high Curie temperature, tunable magnetic properties, low damping, large spin-orbit coupling, high spin polarization, and good crystalline ordering. In this regard, the intermetallic Heusler compounds fulfill most of the requirements for their use in spintronics. In 1903, Fritz Heusler successfully synthesized a room temperature ferromagnetic compound  $\text{Cu}_2\text{MnAl}$ , although none of the constituent elements show ferromagnetism [99, 100]. Some particular group elements in the periodic table participate to form the Heusler compounds, as shown in Fig. 1.18 [101]. These allow one to design materials with tunable magnetic properties, such as ferromagnetic, compensated ferrimagnetic, antiferromagnetic, and non-collinear magnetic ordering. The magnetic and electronic properties of Heusler compounds can be controlled using suitable chemical substitutions. For example, the saturation magnetization of most of the cubic Heusler compounds is proportional to the valance electrons, which can be precisely controlled using chemical substitution [102, 103]. This precise control over the electronic and magnetic properties makes them unique and attractive

**X<sub>2</sub>YZ Heusler compounds**

H																	He	
2.20																		
Li	Be											B	C	N	O	F	Ne	
0.98	1.57											2.04	2.55	3.04	3.44	3.98		
Na	Mg											Al	Si	P	S	Cl	Ar	
0.93	1.31											1.61	1.90	2.19	2.58	3.16		
K	Ca	Sc	Ti	V	Cr	Mn	Fe	Co	Ni	Cu	Zn	Ga	Ge	As	Se	Br	Kr	
0.82	1.00	1.36	1.54	1.63	1.66	1.55	1.83	1.88	1.91	1.90	1.65	1.81	2.01	2.18	2.55	2.96	3.00	
Rb	Sr	Y	Zr	Nb	Mo	Tc	Ru	Rh	Pd	Ag	Cd	In	Sn	Sb	Te	I	Xe	
0.82	0.95	1.22	1.33	1.60	2.16	1.90	2.20	2.28	2.20	1.93	1.69	1.78	1.96	2.05	2.10	2.66	2.60	
Cs	Ba		Hf	Ta	W	Re	Os	Ir	Pt	Au	Hg	Tl	Pb	Bi	Po	At	Rn	
0.79	0.89		1.30	1.50	1.70	1.90	2.20	2.20	2.20	2.40	1.90	1.80	1.80	1.90	2.00	2.20		
Fr	Ra																	
0.70	0.90																	
		La	Ce	Pr	Nd	Pm	Sm	Eu	Gd	Tb	Dy	Ho	Er	Tm	Yb	Lu		
		1.10	1.12	1.13	1.14	1.13	1.17	1.20	1.20	1.10	1.22	1.23	1.24	1.25	1.10	1.27		
		Ac	Th	Pa	U	Np	Pu	Am	Cm	Bk	Cf	Es	Fm	Md	No	Lr		
		1.10	1.30	1.50	1.70	1.30	1.28	1.13	1.28	1.30	1.30	1.30	1.30	1.30	1.30	1.30		

Figure 1.18: Periodic table of elements and the colored elements form Heusler alloy. [101]

candidates for spintronics applications.

### 1.7.1 Structural properties

In general, the Heusler compounds are divided into two groups; (i) half Heusler compounds with  $XYZ$  formula, and (ii) full Heusler compounds with  $X_2YZ$  formula, where  $X$  and  $Y$  are transition metals, and  $Z$  is a main group element. The half Heusler compounds form in cubic crystal structure with space group  $F\bar{4}3m$  (No. 216). The crystal structure of half Heusler compounds can be understood as three interpenetrating FCC sub-lattices [104]. The  $X, Y$ , and  $Z$  atoms are located at  $4c$  ( $\frac{1}{4}, \frac{1}{4}, \frac{1}{4}$ ),  $4b$  ( $\frac{1}{2}, \frac{1}{2}, \frac{1}{2}$ ), and  $4a$  (0,0,0) positions, respectively, as shown in Fig. 1.19 (a). Generally, three types of atomic arrangements are possible as depicted in table (1.1). The full Heusler compounds crystallize in the  $L2_1$  structure with space group  $Fm\bar{3}m$  (No. 225) with  $Cu_2MnAl$  as a prototype [99, 100, 101, 105]. The Wyckoff positions of  $Z, Y$ , and  $X$  atoms are  $4a$  (0, 0, 0),  $4b$  ( $\frac{1}{2}, \frac{1}{2}, \frac{1}{2}$ ) and  $8c$  ( $\frac{1}{4}, \frac{1}{4}, \frac{1}{4}$ ), respectively, as shown in Fig. 1.19 (b) [106]. In addition, the existence of inverse Heusler structure is also found when the atomic number of  $Y$  is more than the  $X$

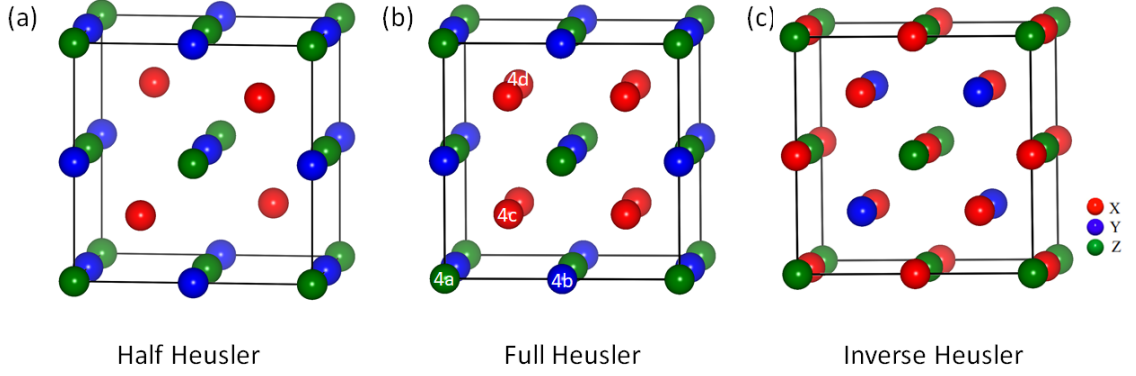


Figure 1.19: Heusler structure. (a) Half Heusler. (b) Regular full Heusler. (c) Inverse Heusler.

Table 1.1: Possible arrangements of atomic position for a half Heusler alloy in the Wyckoff positions 4a, 4b, and 4c.

Type	4a	4b	4b
1	X	Y	Z
2	Z	X	Y
3	Y	Z	Y

(i.e.  $Z(Y) > Z(X)$ ). The inverse Heusler structure is shown in Fig. 1.19(c). It is the prototype of  $\text{HgCu}_2\text{Ti}$  with space group  $F\bar{4}3m$  (No. 216) [107]. The  $X$  atoms are located at 4b  $(\frac{1}{2}, \frac{1}{2}, \frac{1}{2})$  and 4d  $(\frac{3}{4}, \frac{3}{4}, \frac{3}{4})$  positions.  $Z$  and  $Y$  atoms sit at 4a  $(0,0,0)$  and 4c  $(\frac{1}{4}, \frac{1}{4}, \frac{1}{4})$ , respectively. The inverse Heusler alloys are mostly observed for  $\text{Mn}_2\text{YZ}$ -based systems such as  $\text{Mn}_2\text{CoSn}$  [108],  $\text{Mn}_2\text{NiSn}$  [109],  $\text{Mn}_2\text{FeSi}$  [110]. In Heusler compounds, different kinds of disorder are observed due to the mixing of atoms in different sites [111, 112, 113, 114].

Apart from the cubic structure, Heusler compounds can be formed in a tetragonal structure. The cubic structure starts to distort when the crystal field becomes large. If the cubic structure distorted along  $[001]$  direction, then a tetragonal structure forms. This type of distortion is known as Jhon-Teller distortion. Figures 1.20 (a) -(d) show the transformation of a cubic structure to a tetragonal structure. The regular Heusler structure undergoes a transformation to a tetragonal structure with space group  $I4/mmm$ , while the inverse Heusler structure transforms into a

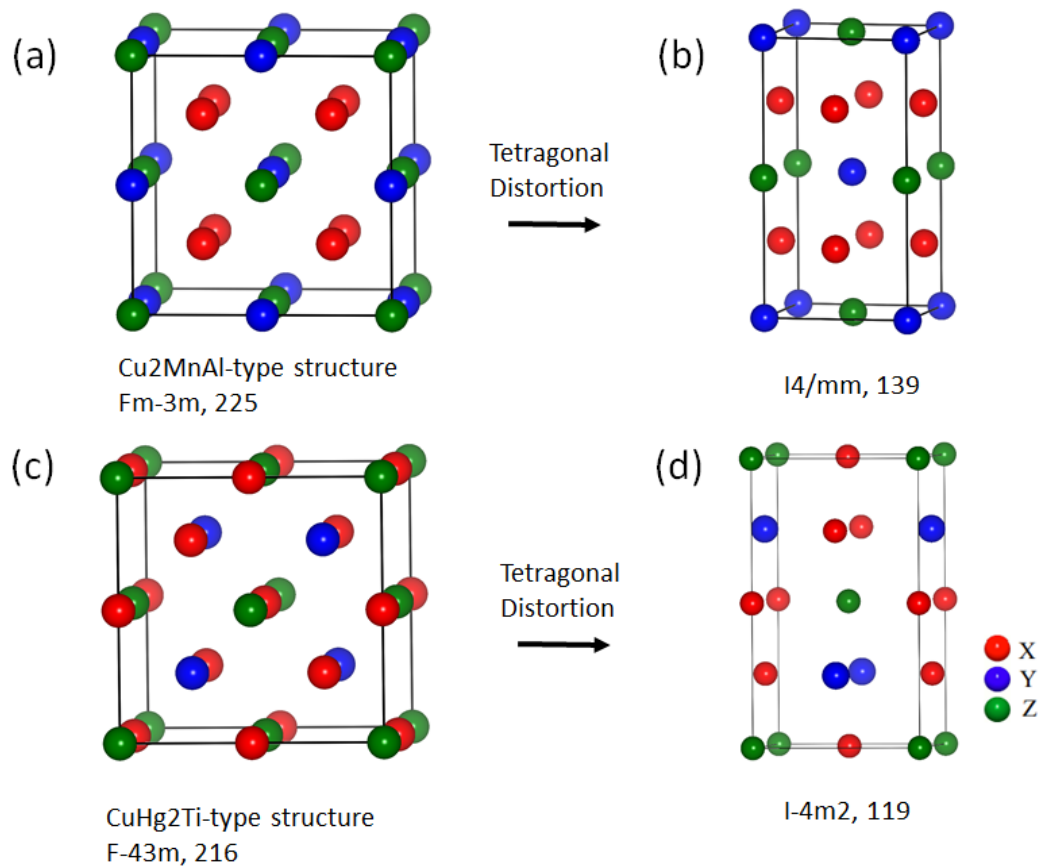


Figure 1.20: Transformation of cubic Heusler compound to its corresponding tetragonal structure. (a)-(b) Regular Heusler to tetragonal structure of space group  $I4/mmm$ . (c)-(d) Inverse cubic Heusler to the tetragonal structure of space group  $I\bar{4}m2$ .

tetragonal structure with space group  $I\bar{4}m2$ . For  $I4/mmm$  space group, the Wyckoff positions of  $X$ ,  $Y$  and  $Z$  atoms are  $4d$   $(0, \frac{1}{2}, \frac{1}{4})$ ,  $2b$   $(0, 0, \frac{1}{2})$ , and  $2a$   $(0,0,0)$ , respectively. In the case of inverse tetragonal structure with space group  $I\bar{4}m2$ , one of the  $X$  atom sits at  $2b$   $(0, 0, \frac{1}{2})$ , the second  $X$  atom and  $Y$  atoms occupy the  $4d$   $(0, \frac{1}{2}, \frac{1}{4})$  position, while the  $Z$  atoms fill the  $2a$   $(0, 0, 0)$  position. The inverse tetragonal structure shows various exotic properties, such as perpendicular magnetic anisotropy, large Curie temperature with low saturation magnetization, and non-collinear magnetism which makes them promising candidates for spintronics applications.

Some of the Heusler compounds show the shape memory effect, in which a structural transition occurs from a high-temperature cubic to a low-temperature tetrago-

nal phase. This transition is reversible, although the phase transformation does not trace the same path. The high-temperature cubic phase is known as the austenite phase and the low-temperature tetragonal phase is referred as the martensite phase. The austenite phase has higher symmetry than the martensite phase. During the transition from the austenite to martensite phase, the Heusler compound adopts a distorted crystal structure, typically characterized by twinned variants [115, 116, 117]. Twin crystal structures represent the formation of distinct crystallographic domains within a material. These twin domains show similar types of structures with different orientations [as shown in Fig. 1.21 (a)]. The twinning phenomenon arises due to the reorientation of atoms during the phase transition to minimize the strain energy. The twin domains are separated by the twin boundaries. The width of the twin domains depends on the composition and the crystal growth process. Sometimes, the width of the twins becomes several microns, whereas some materials also show nano twins [116, 118]. Figure 1.21 (b) shows the nano twin structure and the effects on the Selected Area Electron Diffraction (SAED) pattern [116]. The diffraction spots are elongated and consist of multiple spots.

In the case of magnetic materials with twining microstructure, complex domain structures are observed. The magnetic domain inside a single twin variant is  $180^\circ$  type [119], while  $90^\circ$  domains are formed in the adjacent twins as depicted in Fig. 1.21 (c). Figure 1.21 (d) shows the twin structure and magnetic domain of Ni-Mn-Ga Heusler alloy. The black and dark regions are distinct magnetic domains where the magnetic moments form  $180^\circ$  (black and white arrow) domain. The modulated structure forms in such a way that the magnetic moment in each twin variant always align along  $[001]$  easy axis.

### 1.7.2 Magnetic properties of Heusler compounds

The Heusler compounds exhibit a diverse range of magnetic properties, including ferromagnetism, ferrimagnetism, antiferromagnetism, and even non-collinear magnetism. In the half-Heusler (XYZ) structure, in general, only one of the constituent

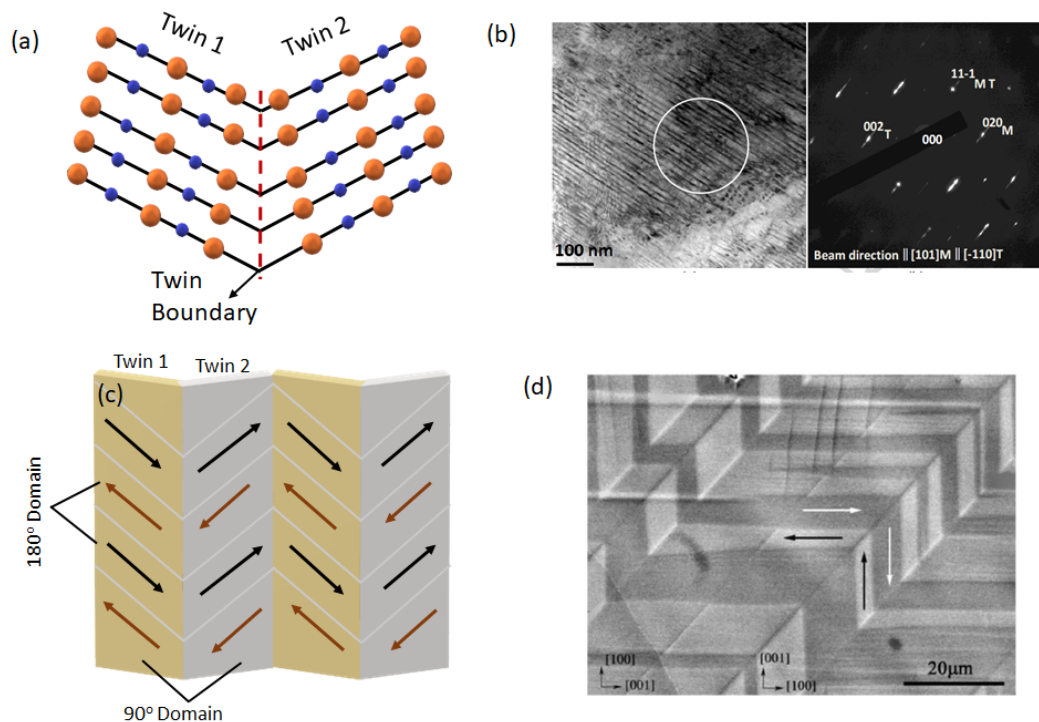


Figure 1.21: (a) Schematic of twin crystal structure. (b) Microstructure of twin domains and Selected Area Electron Diffraction (SAED) pattern [116]. (c) Illustration of the magnetic domain in the presence of twin crystals. (d) Image of magnetic (black and white region) and twin domain. The Black and white arrows show the orientation of the magnetic moment [119].

atoms carries a magnetic moment [83, 120, 121]. Specifically, in the case of Mn-based compounds (MnYZ), the magnetic moment is carried by the localized 3d electrons of  $\text{Mn}^{3+}$ , while in certain rare-earth (RE) based Heusler compounds, the 4f electrons of RE atoms carry the magnetic moment [121]. The full Heusler or inverse Heusler alloys in general exhibit more than two magnetic sub-lattices. Two different sub-lattices can have ferromagnetic or antiferromagnetic alignment. The magnetic moment in the cubic Heusler compounds can be estimated by Slater - Pauling rule [122, 123]. For cubic full Heusler alloy, the magnetic moment is given by  $M_s = 24 - N_v$ , and in the case of cubic half Heusler the magnetic moment is given as  $M_s = 18 - N_v$ , where  $N_v$  represents the number of valence electrons. Sometimes this rule does not work when atomic disorders are present in the system. Apart from collinear magnetism, certain Heusler system, e.g.,  $\text{Mn}_2\text{RhSn}$  exhibits

non-collinear magnetic structure [124]. In the Mn-based Heusler compounds the distance between Mn-Mn is relatively large, thereby excluding the direct exchange. The Ruderman-Kittel-Kasuya-Yosida(RKKY) type indirect exchange interaction is observed in these compounds. The RKKY interaction is mediated by the sp electrons of Z element [102, 125].

### 1.7.3 Heusler compounds in Spintronics

The distinct properties of Heusler compounds make them excellent candidates for the realization of spintronics devices, such as magnetic memory devices, switching devices, and logic devices. Heusler materials exhibit all the basic properties required for practical spintronics device applications, including a high Curie temperature with tunable magnetic properties, large spin polarization, and excellent crystalline ordering. These inherent characteristics make Heusler systems promising candidates in the field of spintronics, enabling the development of advanced and efficient electronic devices. For example, NiMnSb shows large spin polarization that can enhance the efficiency of a magnetic tunnel junction (MTJ) [126, 127, 128, 129]. Similarly, Mn<sub>2.5</sub>Ge displays a large perpendicular magnetic anisotropy [130]. The strong perpendicular magnetic anisotropy gives thermal stability at a reduced size in high-density data storage devices. Some Heusler compounds exhibit unique band topology that gives rise to a non-zero Berry phase, which gives large anomalous Hall, thermal Hall effect, and other quantum emergent properties [131, 132, 133]. The heavy-metal-based Heusler systems possess large spin-orbit coupling [134, 135]. The interplay of electronic and magnetic structures along with large spin-orbit coupling, gives rise to different exotic phenomena. Particularly, the  $D_{2d}$  materials with large spin-orbit coupling can lead to non-collinear magnetic structures, such as skyrmion/antiskyrmion at room temperature [1, 62, 124, 136, 137, 138]. These novel magnetic phases can be used as the building blocks of future spintronics devices.

Due to the above discussed exceptional characteristics, Heusler materials continue to attract a lot of attention for their use in spintronics devices, such as mag-

netic memories, spin valves, tunneling magnetoresistance devices, and spin Hall effect devices. The ongoing research involving these compounds aims to unlock the full potential of the Heusler family in the advancement of spintronics technology, paving the way for the development of faster, efficient, and energy-saving devices.

## 1.8 Outline of the Thesis

In the present thesis, a detailed investigation of the characterization of non-trivial spin textures and anomalous electronic transport properties in Mn-based Heusler alloys are carried out. This work includes the study of thermomagnetic and electrical signatures of magnetic antiskyrmions, as well as their stability under external perturbations. In addition, the manipulation of electronic transport properties is shown using chemical engineering. The present thesis is divided into five chapters. The Chapter-1 is focused on the introductory part involving different types of magnetic interactions/ phenomena and a literature survey. Chapter-2 mostly discusses the experimental techniques used in the present thesis. Chapter-3 is focused on the characterization of antiskyrmion phase using the magnetocaloric effect (MCE) and ac susceptibility measurements. The study on stability and phase evolution of magnetic antiskyrmions in a micron size single crystalline device is presented in Chapter-4. In Chapter-5, the manipulation of anomalous Hall effect (AHE) involving different mechanisms is demonstrated. Finally, the summary and concluding remark is given in Chapter-6.

# Chapter 2

## Experimental Methods

This chapter presents the experimental methods and the working principle of various instruments used in this thesis work. First, the sample preparation technique, followed by the detailed procedure of structural and magnetic characterization techniques, are presented. After that, the fabrication procedures of Hall devices and TEM samples are discussed. The details of electrical resistivity measurement are included towards the end.

### 2.1 Sample preparation

The first step towards the experimental study of magnetic/electrical phenomena in a particular system is the synthesis of high-quality crystals. For the present thesis, polycrystalline samples of  $\text{Mn}_{1.4}\text{Pt}_{1-x}\text{Pd}_x\text{Sn}$  (with  $x=0$  and  $0.1$ ),  $\text{Mn}_{1.1}\text{PtSn}$  and  $\text{MnPt}_{1-x}\text{Ir}_x\text{Sn}$  (with  $x=0, 0.1, 0.2, 0.3, 0.5$ ) are synthesized using the arc melting furnace, which is a well-known method widely used to prepare intermetallic compounds. The arc-melt procedure consists of two essential components: (1) a copper hearth plate with several grooves, which is connected to water cooled chiller, and (2) a tungsten tip. The copper plate acts as the positive electrode and the tungsten tip works as the negative electrode. The tungsten tip is positioned close to the copper plate, and a high voltage is applied between the copper hearth and the



to a pressure of around  $10^{-3}$  mbar, and argon gas is purged several times during the vacuum process. Once the chamber is ready, first the titanium piece is melted to remove any oxygen impurity. Then the arc is struck carefully on the elements placed in another groove. The elements are melted for a few seconds to ensure proper mixing and liquefaction. After that, the current is set to zero so that the melted liquid ingot becomes solid. Then the ingot was flipped and remelted 3-4 times for proper mixing of the elements. The prepared ingots are sealed in a quartz tube under vacuum and annealed at required temperatures for one week.

## 2.2 Structural characterizations

### 2.2.1 X-ray Diffraction (XRD)

X-ray diffraction is used for the structural characterization of the polycrystalline samples presented here. The X-ray diffraction works on the principle of Bragg's law, which is expressed as

$$2d\sin(\theta) = n\lambda \quad (2.1)$$

where  $d$  denotes the interplanar spacing of two adjacent planes,  $\theta$  represents the angle of incident, and  $\lambda$  is the wavelength of the X-ray. The characteristic primary X-ray beam incident on the sample surface and get scattered by the lattice planes. After scattering from the adjacent planes, the scattered X-rays gain a path difference, as shown in Fig. 2.2. The path difference between the reflected X-rays from the adjacent planes is  $2d\sin\theta$  for an incident angle  $\theta$ . The reflected beams produce constructive interference once they satisfy the Bragg's condition. The diffraction pattern consists of multiple peaks at different  $\theta$  positions. The value of  $d$  corresponding to the lattice plane can be determined from the known values of  $\theta$  and  $\lambda$ .

For the present work, the Rigaku SmartLab X-ray diffractometer with Cu-K $\alpha$  source of wavelength  $\lambda = 1.54$  is used.

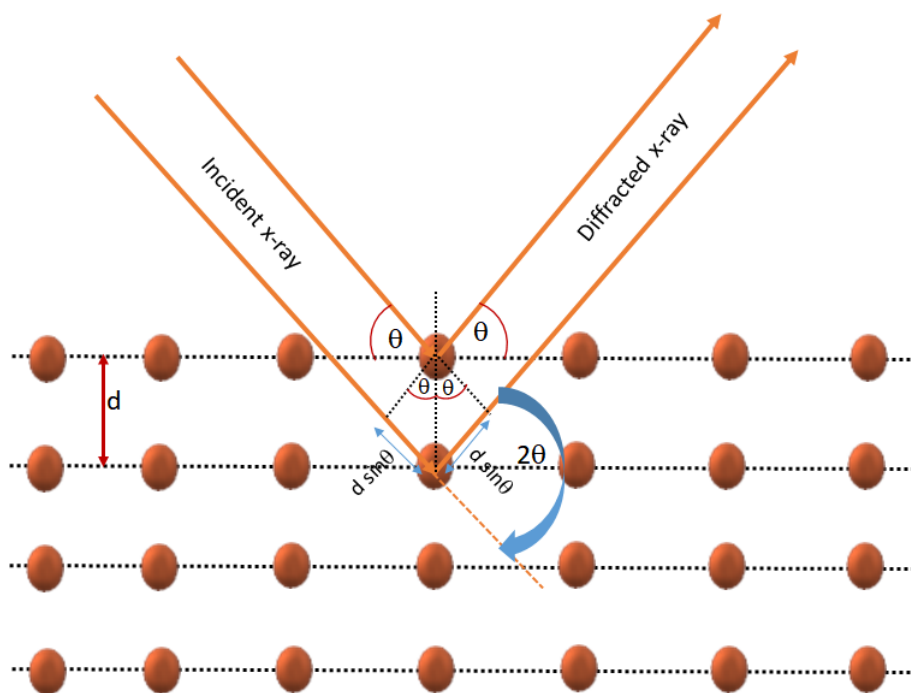


Figure 2.2: Schematic of X-ray diffraction scattered from a set of lattice planes.

### 2.2.2 Scanning Electron Microscopy (SEM)

The surface morphology, phase purity, and compositional analysis for all the samples are examined using Scanning Electron Microscopy (SEM) and Energy-Dispersive X-ray Spectroscopy (EDS). The emitted electrons from the field emission gun are focused on the sample surface and produce several signals. These signals are collected by different detectors and give valuable information regarding the homogeneity, as well as the quantification of the composition. The schematic of SEM is shown in Fig. 2.3. It consists of an electron gun that emits electrons with the application of high voltage. The emitted electrons are accelerated and directed toward the sample surface by condenser lenses and objective lenses. The condenser lenses control the beam size, and the objective lens focuses the electron beam on the sample. Once the electrons interact with the sample surface, secondary electrons, backscattered electrons, and characteristic X-rays are produced. Secondary electrons are used to image the surface topography, and backscattered electrons are used to examine the compositional contrast. The X-rays are produced when the primary electrons knock

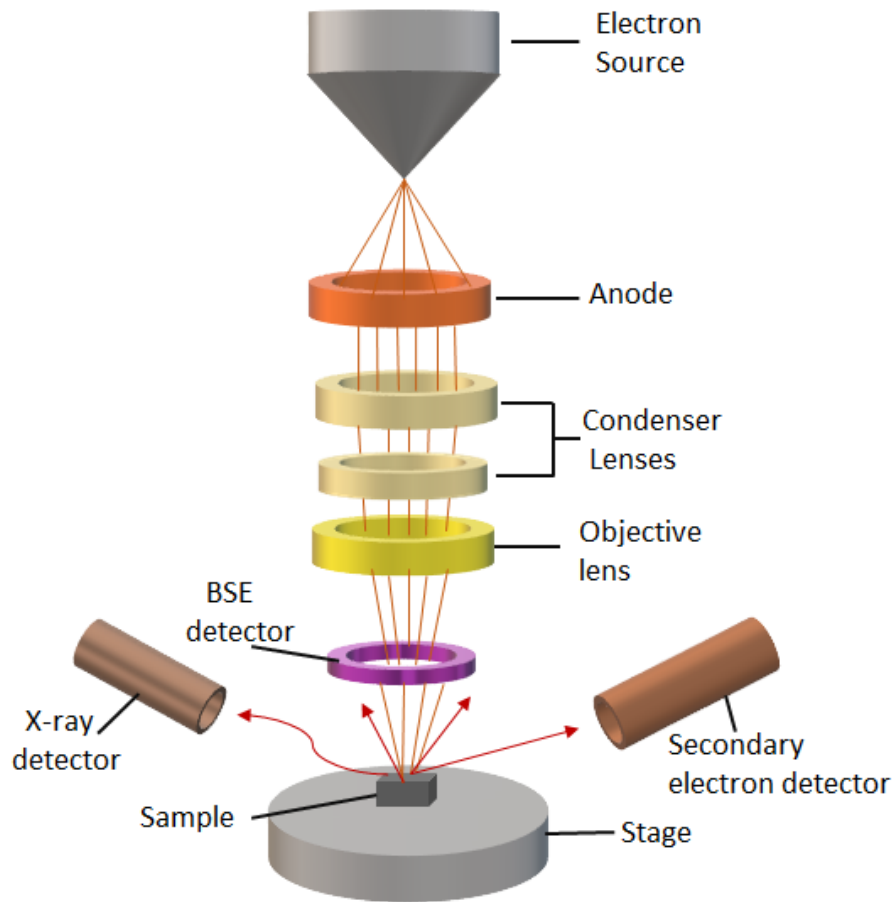


Figure 2.3: Schematic of scanning electron microscope (SEM)

out the inner shell electron, leaving a vacant position that is filled by another electron from the outer shell. This resulted in the emissions of extra energy in the form of X-rays. These emitted X-rays give information about the composition of the elements present in the sample.

### 2.2.3 Transmission Electron Microscopy (TEM)

In the present thesis work, transmission electron microscopy is used to identify the orientations of the devices presented in Chapter 4. The high-energy electron beam passes through an electron transparent sample and interacts with the atoms in the crystal. The electrons are then diffracted by the atoms and produce a diffraction spot when they satisfy Bragg's condition. The diffraction patterns consist of bright spots, which are recorded using a camera. The schematic of TEM diffraction through

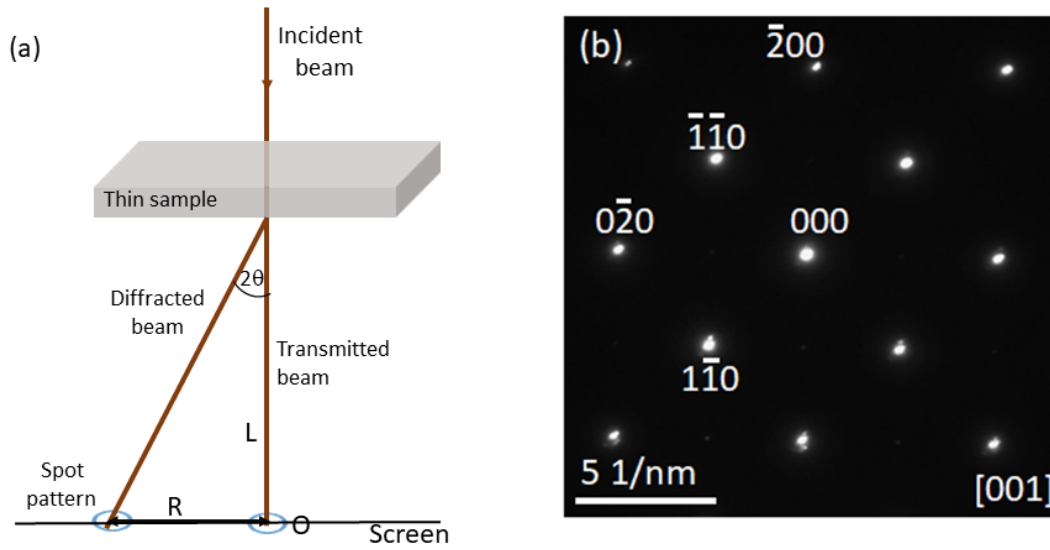


Figure 2.4: (a) Illustration of TEM diffraction. (b) Selected Area Electron Diffraction (SAED) pattern.

a thin sample and typical diffraction pattern are shown in Fig. 2.4. The relation with the distance  $R$  of a diffraction spot from the central spot and the lattice spacing  $d_{hkl}$  is given by  $d_{hkl} = \frac{\lambda L}{R}$ . Here  $\lambda$ , is the wavelength of the incident electrons, and  $L$  is the camera length. From the diffraction patterns, one can know the crystal structure and orientation of the crystal. By measuring the distance  $R$  from the central spot and using the experimental value of  $\lambda$  and  $L$ , one can calculate the  $d_{hkl}$ . By calculating  $d_{hkl}$  the crystal orientation can be determined. In the present work, the selected area electron diffraction patterns are taken using JEOL JEM F200 TEM with electron energy 200 kV.

### 2.3 Magnetic characterizations

A Quantum Design Superconducting Quantum Interference Device - Vibrating Sample Magnetometer (SQUID-VSM) is used to perform the magnetic measurements. The zero field-cooled (ZFC) and field-cooled (FC) temperature variation of magnetization  $M(T)$  measurements are carried out for all the samples. The zero field-cooled protocol involves cooling the sample to a low temperature without a magnetic field. The measurements are then taken while the temperature is increased in the presence

of a constant applied field. In the case of the field-cooled protocol, the measurements are taken during cooling in the presence of the magnetic field. Field-dependent magnetization  $M(H)$  measurements are performed over a field range of +5 T to -5 T at several temperatures. In the following, the working principles of VSM and SQUID are discussed.

### 2.3.1 Vibrating Sample Magnetometer (VSM)

Precise magnetic measurements are possible using a Vibrating Sample Magnetometer (VSM). The working principle is based on the Faraday's law of induction, which can be written as

$$V_{coil} = -\frac{d\phi}{dt}. \quad (2.2)$$

The law states that a change in magnetic flux  $\frac{d\phi}{dt}$  can generate an electric field or voltage  $V_{coil}$ . The generated voltage is used to measure the magnetic field. The schematic of a VSM is shown in Fig. 2.5. First, the sample is placed inside the VSM, and a constant magnetic field is applied, which magnetizes the sample. Inside the VSM, the sample is forced to oscillate in an up-and-down direction. As the sample moves, the change in magnetic flux generates an electric field. The induced voltage detected by the coils is related to the magnetic moment of the sample by the following relation

$$V_{coil} = 2BmA\sqrt{f}\sin(2\sqrt{ft}) \quad (2.3)$$

where B represents the coupling constant,  $m$  accounts for the DC magnetic moment of the sample, A is the amplitude of oscillation, and f is the frequency of oscillation.

### 2.3.2 Superconducting Quantum Interference Device (SQUID)

Superconducting Quantum Interference Device (SQUID) can measure extremely weak magnetic fields. The core component of a SQUID consists of two Josephson junctions in a superconducting loop. The Josephson junction is formed with a combination of two superconductors separated by a thin insulating layer. The

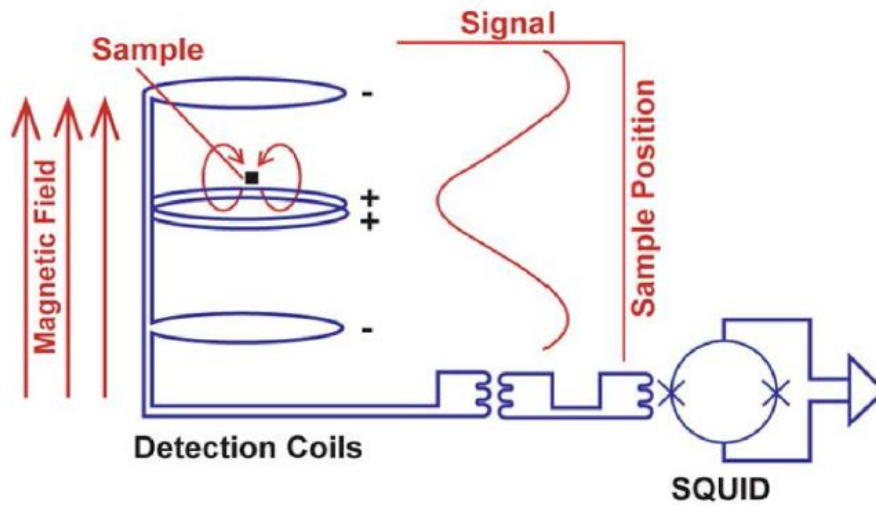


Figure 2.5: Schematic of Vibrating Sample Magnetometer (VSM) with the attachment of SQUID. (The schematic diagram is taken from Quantum Design user's manual)

flow of current through the junction depends on the external magnetic flux. Hence, whenever there is a magnetic flux, a voltage is developed across the junction, which is proportional to the magnetic field. The voltage is measured by an integrated circuit. The detection of tiny magnetic fields can be influenced by the presence of other magnetic fields or the presence of noise. For this, the SQUID is placed inside a superconducting shield. A VSM is used to vibrate the sample inside the coil which generates a magnetic flux that is picked up by the coil. The change in the flux is then sensed by the SQUID and the corresponding change in the voltage is measured by the electrical circuit. The combination of VSM and SQUID makes a very sensitive tool to measure the magnetization of the sample. In this thesis work, a quantum design MPMS3 is used to measure the magnetic properties of the samples.

### 2.3.3 AC Susceptibility measurement

The AC susceptibility measurement is an important tool to identify different magnetic phases present in the systems. The magnetization  $M$  of the sample is related

to the applied field  $H$  by the relation

$$M = \chi H \quad (2.4)$$

where  $\chi$  is the susceptibility, which refers to the response of a system under an applied magnetic field. In the AC susceptibility measurements, a small AC field is applied, and the response of the sample's magnetic moment to the field is measured. Depending on the study of interest, a DC field is also applied during the AC susceptibility measurements. The AC susceptibility is a complex quantity and is expressed as

$$\chi_{AC} = \chi'_{AC} - \chi''_{AC} \quad (2.5)$$

Where  $\chi'_{AC}$  is the real part, which is related to reversible magnetization and the  $\chi''_{AC}$  is the imaginary part associated with the losses because of the irreversible magnetization process under the influence of an applied field  $H(t) = H_{DC} + h_{AC}\cos\omega t$ . The magnetization under the oscillating field tries to follow the AC magnetic field, and sometimes it may lag behind with the applied field. The total magnetization in response to the applied field  $H(t)$  is expressed as

$$M(t) = M_{DC} + m_{AC}\cos(2\pi\omega t - \theta) = M_{DC} + m_{AC}\cos\omega t\cos\theta + m_{AC}\sin\omega t\sin\theta \quad (2.6)$$

where  $M_{DC}$ , and  $m_{AC}$  are the DC and AC components of the magnetization, respectively.  $\theta$  is the phase difference between the magnetization and applied AC field. The real and imaginary parts of AC susceptibility can be written as  $\chi' = m_{AC}\cos\theta/h_{AC}$  and  $\chi'' = m_{AC}\sin\theta/h_{AC}$ . The real part is in phase and the imaginary part is out of phase with the AC magnetic field.

In this work, field-dependent AC susceptibility measurements are performed using the ACMS option available in Quantum Design- Physical Property Measurement System (QD-PPMS), with  $h_{AC} = 10 \text{ Oe}$ .

### 2.3.4 Neutron Diffraction

Neutron diffraction is widely used to determine the structural as well as microscopic magnetic properties of a magnetic material. The wavelength of the thermal neutron is comparable to the lattice spacing which makes it valuable for investigating structural and magnetic characteristics. The neutron beam interacts with the atomic nuclei, resulting in a diffraction pattern analogous to that observed in X-ray diffraction. Neutron diffraction provides more detailed information compared to the X-ray diffraction. The neutrons interact with the atomic nuclei, while the X-rays interact with the electron cloud. The scattering of neutrons from the nuclei is isotropic, which means the scattering amplitude does not vary with the scattering angle, as observed in the case of X-ray diffraction. Apart from structural information, neutron diffraction is capable of detecting the magnetic state of the sample because of the presence of a small magnetic moment of  $-1.913 \mu_N$ . The presence of a small magnetic moment with zero charge makes it sensitive to the magnetic scatterers in the target materials. Depending on the magnetic structure, magnetic satellite peaks and nuclear Bragg peaks in the neutron diffraction pattern can be obtained. In the case of similar nuclear and magnetic unit cells, the magnetic and nuclear Bragg peaks appear at the same position. This results in an increase in the intensity of the Bragg peaks.

For the present work, powder neutron diffraction data at several temperatures are taken using PD2 powder diffractometer ( $\lambda = 1.243 \text{ \AA}$ ) at the Dhruva reactor, Bhabha Atomic Research Centre, Mumbai, India.

## 2.4 Site-specific device and TEM sample fabrication

The detailed study of the antiskyrmion phase and its stability is carried out in single crystalline micron-size Hall devices. Thin Hall bars with specific orientations

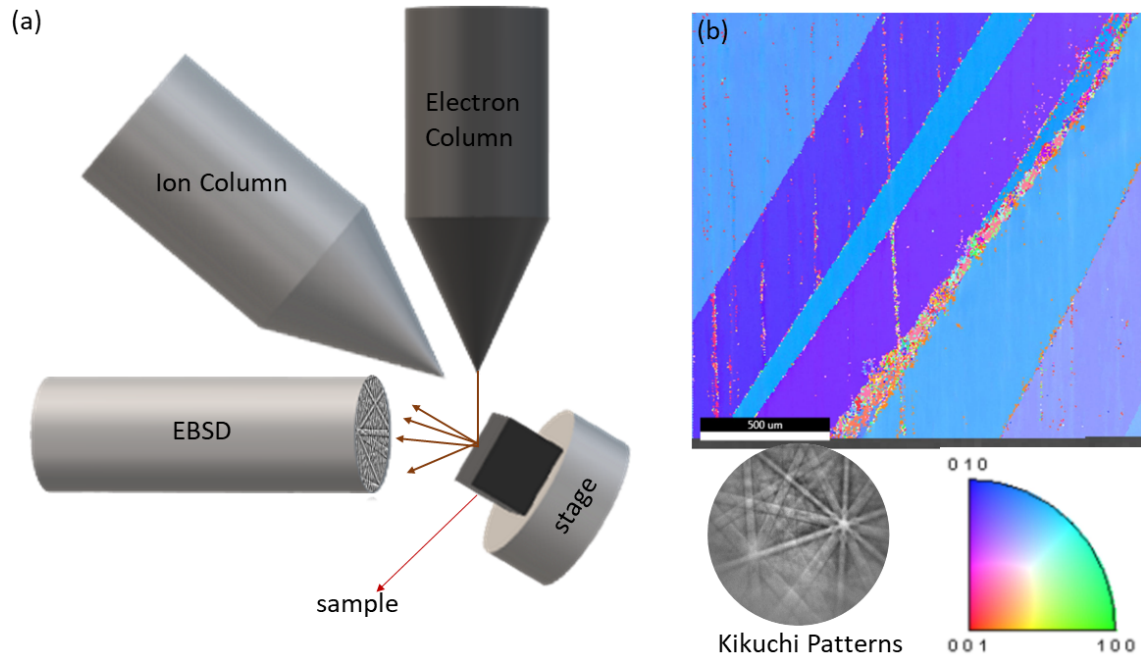


Figure 2.6: (a) Schematic of FIB system with EBSD detector setup. (b) EBSD mapping of inverse pole figure of a polycrystalline material. Lower panel shows the Kikuchi patterns and color wheel.

are fabricated utilizing Electron Backscatter Diffraction (EBSD) and Focused Ion Beam (FIB). The working principle and the experimental procedure are discussed in the subsequent section.

### 2.4.1 Electron Backscatter Diffraction (EBSD)

Electron Backscatter Diffraction (EBSD) with a combination of SEM is used to determine the crystal orientations, phase identification, and local texture of crystalline materials. It is capable of giving information with sub-micron level resolution and can be used for any crystalline sample. The EBSD patterns are collected by tilting a highly polished sample inside the SEM chamber [shown in the schematic Fig. 2.6 (a)]. The reason for high tilting is that it gives a much higher diffraction signal, which reduces the signal-to-noise ratio. A high-energy electron beam interacts with the sample surface and gets scattered from the sample surface or the lattice plane. The backscattered electrons create diffraction patterns once they satisfy Bragg's condition  $2d\sin\theta = n\lambda$ . These diffracted electrons form a pattern on the phosphor

screen called Kikuchi patterns, shown in the lower panel of Fig. 2.6 (b). The Kikuchi patterns or Kikuchi bands are representative of individual lattice planes. The width of the Kikuchi band is inversely proportional to the lattice spacing  $d$ , and the angle between two Kikuchi bands depends on the angle between two lattice planes. The characteristics of these bands are used to determine the crystal orientation. Once the diffraction pattern is collected from the sample, it is indexed with the help of a known crystal structure and gives crystallographic information. Figure 2.6 (b) shows the EBSD mapping of a polycrystalline specimen. The different color region represents various grains, and the color wheel (lower panel of Fig. 2.6 (b)) depicts the orientation of the grains.

During the experiment, the bulk polycrystalline sample is polished with mechanical and vibratory polisher in several steps. The sample is put inside the SEM chamber and tilted  $70^\circ$  from the horizontal position. Electrons with an energy of 20 kV are used to collect the EBSD patterns. Automated indexing maps the crystal orientation from which the desired grain is selected for the present study.

## 2.4.2 Focused Ion Beam (FIB)

A focused Ion Beam (FIB) is a powerful tool for imaging and nano-fabrication in scientific research and industrial sections. In addition to the electron beam column, a FIB consists of an ion beam column. The ion beam column consists of an ion source, several apertures, and objective lenses which control the ion beam. The ion beam is used for the milling and fabrication of nanostructure. In most of the FIB systems,  $Ga^+$  ion is used because of its several benefits. The melting point of Ga metal is low, and it can easily be ionized, which is essential to produce an ion beam efficiently. From the ion source,  $Ga^+$  ions are ejected, and the ions are accelerated with a high voltage to a maximum energy of 30 kV. The accelerated ions are collimated and focused using electrostatic lenses. The apertures, in combination with several condensers, are used to adjust the probe current from 1 pA to 100 nA. The high-energy  $Ga^+$  with adjusted probe currents are used to sputter the

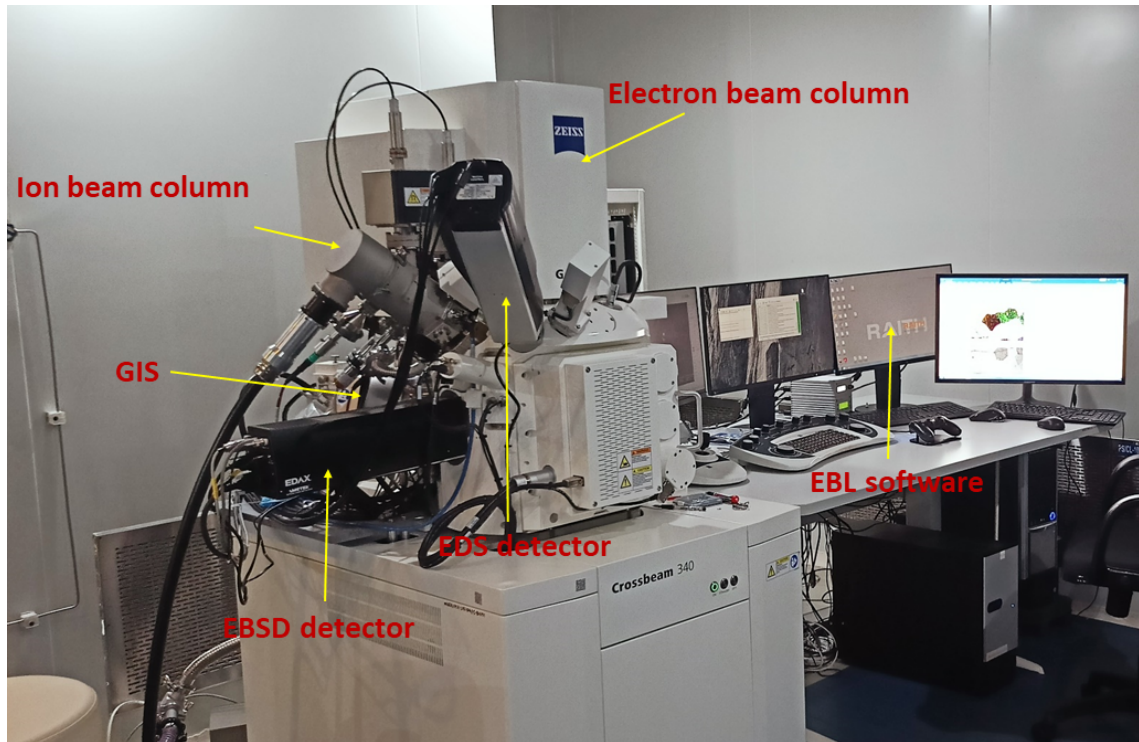


Figure 2.7: (a) Image of Focused Ion Beam (FIB) system (Crossbeam 340, Zeiss) installed in the School of Physical Sciences, NISER, Bhubaneswar.

materials from a specific position in a controlled way. In addition to milling, a Gas injection system (GIS) is attached to the FIB system to deposit several materials. During the deposition process, a precursor gas is released to the sample surface from the GIS needle and ions are released simultaneously. The interaction of ions with the precursor gas molecules creates volatile and non-volatile products. The sample surface absorbs the non-volatile products, and the volatile products are pumped out from the chamber. In this way, several materials are deposited using the combination of ion beam and GIS.

In this thesis work, site-specific devices and TEM lamellae are prepared using Zeiss cross beam 340 installed in the School of Physical Sciences, NISER, Bhubaneswar (shown in Fig 2.8). The FIB system is equipped with a dual beam, a combination of SEM and ion gun. In addition, an EBSD detector and a micromanipulator are attached to the system. The micromanipulator can be moved with a joystick in the x, y, and z directions. It is used to lift out the micron-size sam-

ples. The detailed procedures for the fabrication of devices and TEM specimens are discussed below.

#### 2.4.2.1 Site-specific device fabrication

The site-specific thin Hall bars are fabricated using the combination of EBSD and FIB in several steps. In this thesis work, the Hall bar devices and the TEM lamellae are prepared from a single grain of specific direction. At first, using the EBSD, the desired grain is identified. The angle between the SEM column and the ion beam column of Zeiss 340 dual beam is  $54^\circ$ , and the optimum FIB working distance is 5.1 mm. After the grain is identified, the stage is tilted back to  $54^\circ$  with working distance of 5.1 mm. Next, the ion beam is switched on, and two big trenches are cut using  $Ga^+$  ion with probe current ranging from 7 nA to 15 nA, as shown in Fig. 2.8 (a). Subsequently, the two sides of the lamella are polished using  $Ga^+$  ion milling with a lower probe current of 1.5 nA to 3 nA. This step is repeated several times to thin the sample shown in Figs. 2.8 (b)- (c). Next, the stage is tilted back to  $0^\circ$ , and a L shape cut is made to free the lamella from the two sides, shown in Fig. 2.8 (d). Now, a micromanipulator is inserted and touches the sample at the free end of the lamella. After that, the lamella is attached to the micromanipulator using tungsten deposition, and the portion of the lamella connected with the bulk sample is cut. Then the lamella is lifted out from the bulk sample [shown in Fig. 2.8 (e)]. The lamella is then transferred to the Si/SiO<sub>2</sub> substrate having predefined gold electrodes [Fig. 2.8 (f)], and securely fixed using tungsten deposition [Fig. 2.8 (g)]. The final connections between the Hall bar terminals and the gold electrodes are made using GIS-assisted tungsten deposition. Figure 2.8 (h) is the false color SEM image of the final device structure with the gold electrodes. The dimension of the device shown here is  $17 \mu m \times 5.3 \mu m \times 975 nm$ .

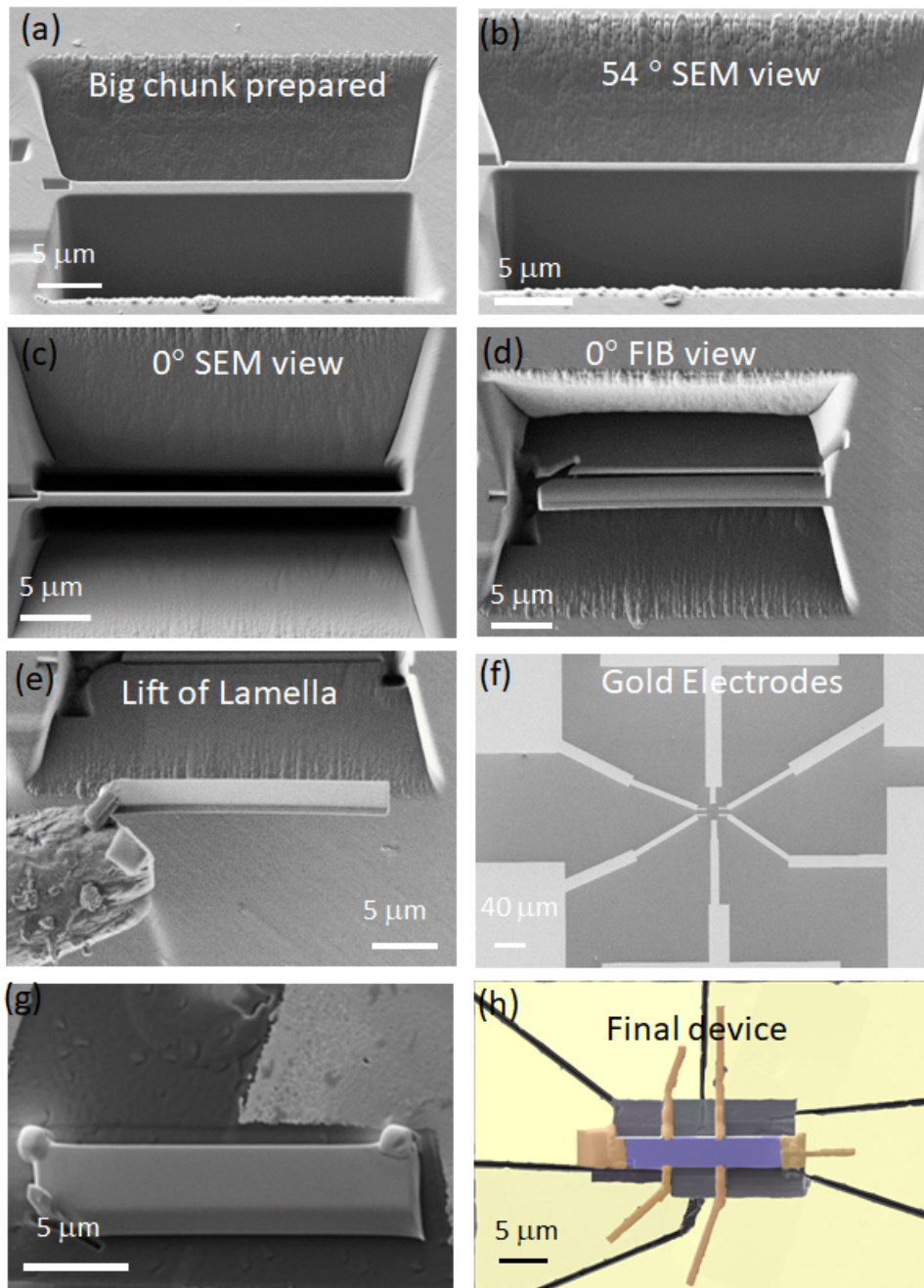


Figure 2.8: Flow chart of Hall device fabrication. (a) Two big trenches are milled using  $Ga^+$  ions to prepare a chunk. (b)-(c) 54° and 0° SEM view of thin lamella, respectively. (d) L shape cut to free the lamella from two sides. (e) Lift off the lamella using micromanipulator. (f) Si/SiO<sub>2</sub> substrate with predefined gold electrodes. (g) Lamella is mounted on the substrate. (h) False color SEM image of final Hall device with Hall terminals connected to gold electrodes using tungsten deposition.

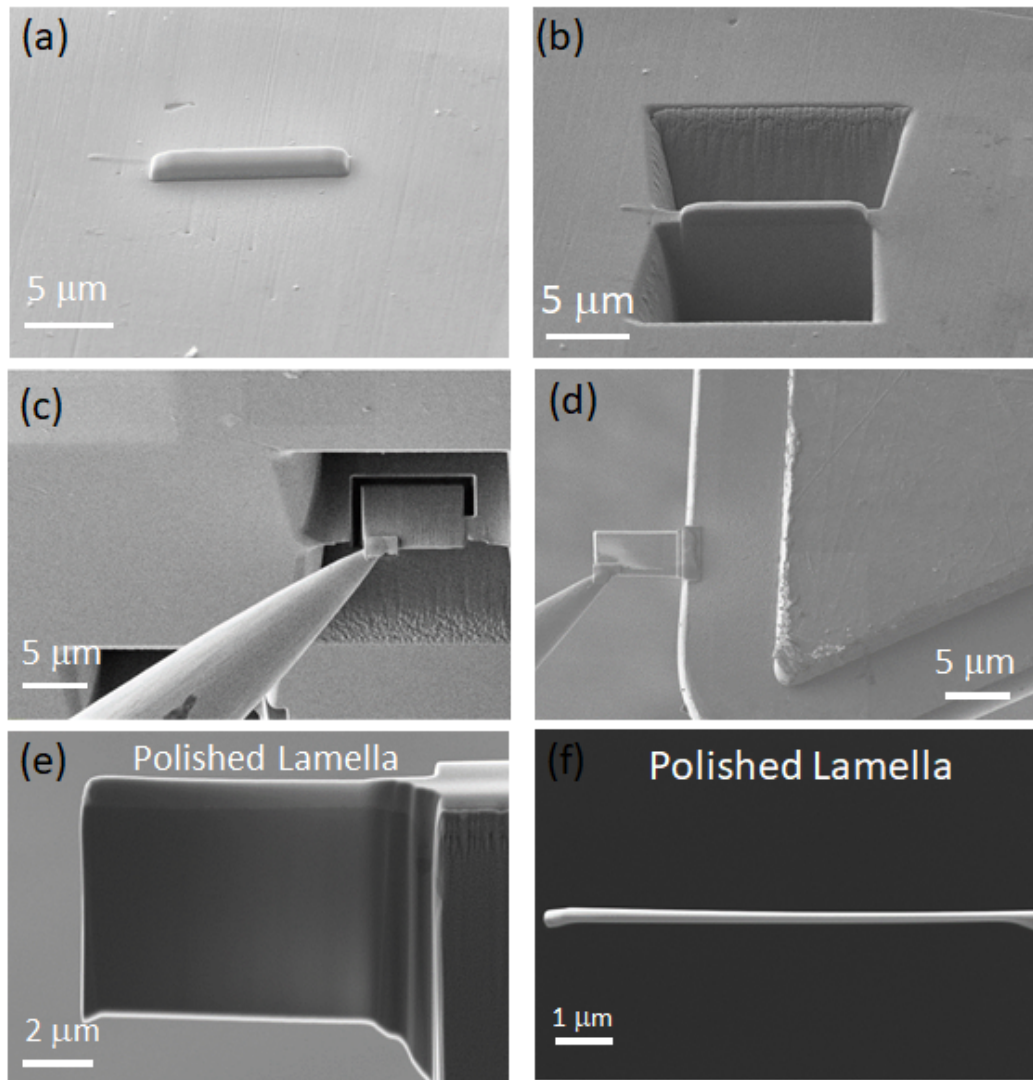


Figure 2.9: TEM sample preparation procedure. (a) A protective layer of Pt is deposited. (b) Two sides of the protective layer region are milled. (c) Micromanipulator is attached with the lamella. (d) The lamella is fixed in a Cu grid. (e)-(f)  $54^\circ$  and  $0^\circ$  SEM view of the polished electron transparent lamella, respectively.

#### 2.4.2.2 TEM sample preparation

The preparation of electron transparent TEM specimens is carried out in a similar manner to that of the Hall device fabrication. Here, some additional steps are used to prepare the thin TEM lamellae. In the first place, a protective layer of platinum is deposited on the sample surface as shown in Fig. 2.9 (a). This is required to prevent any damage due to the  $Ga^+$  ions while thinning it to nanometer thickness.

The platinum deposition is carried out at  $54^\circ$  angle with a probe current of 100 pA to 300 pA. Then the steps shown in Figs. 2.8 (d) - (e) are followed to lift out the lamella. This time the lamella is transferred to a half-moon Copper grid and fixed using Pt deposition [shown in Fig. 2.9(d)]. After that, the lamella is detached from the tip. The next and crucial step is to thin the sample down to 100 nm thickness. The back side of the lamella is polished by tilting the sample at an angle of  $51^\circ$ , and the front side is polished with a tilting angle of  $57^\circ$ . This is done intentionally to remove any thickness variation in the sample surface. Figures 2.9 (e)- (f) show the SEM image of the thin lamella at  $54^\circ$  and  $0^\circ$  angles, respectively. The thickness of the final electron transparent lamella is about 100 nm.

### 2.4.3 Electron Beam Lithography (EBL)

Electron beam lithography or e-beam lithography is a maskless lithography technique used to pattern different structures with nanometer resolution. The electron beam lithography (Raith software) attached to the FIB system is used to pattern the desired structure. Several steps of metal deposition using the e-beam lithography process are shown in Fig. 2.10. In the first step, Si/SiO<sub>2</sub> substrate is cleaned using an ultrasonic bath; then, the cleaned substrate is coated with electron beam-sensitive resist (PMMA 450) using the spin coater. The coated substrate is baked at  $100^\circ\text{C}$  for 2 min. Utilizing the Raith software, the desired patterns are generated, and subsequently, the electron beams are exposed on the designated area of interest. The exposures are carried out with electron energy 10 kV - 20 kV. The electron beam changes the solubility of the exposed area. Then the substrate is immersed in a solution of mixed MBK and IPA with a 1:3 ratio. The solution removes the resist (for positive resist) from the exposed area, whereas it remains intact in the unexposed area. The gold metal deposition is carried out using DC sputtering, and then the substrate is immersed in acetone for the lift-off. Once the lift-off process is completed, the gold metal remains exclusively within the exposed area. Figure 2.8 (f) depicts a substrate featuring gold electrodes fabricated utilizing the aforementioned

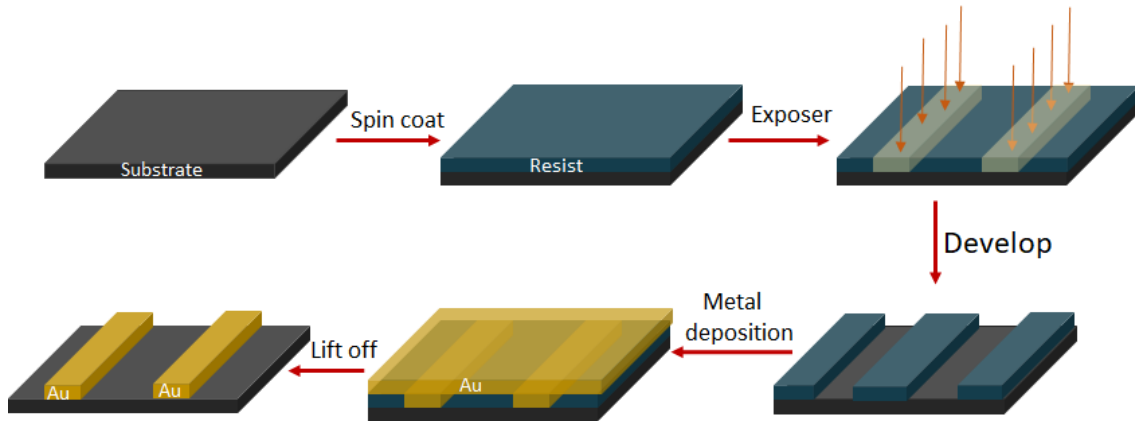


Figure 2.10: Different steps of preparing metal electrodes using Electron beam lithography and metal deposition.

method.

## 2.5 Electronic transport measurements

The electronic transport properties are measured using a Quantum Design Physical Properties Measurements System (PPMS) [shown in Fig. 2.11]. The longitudinal and transverse Hall resistivity are measured using four and five probe configurations using the ACT option available in the PPMS. The measurements are performed in a rectangular shape bulk sample and Hall device with applying an AC current. The schematics of four probe and five probe connections are shown in Fig. 2.12. The Hall resistivity is measured in four probes as well as with the five probe method, while the longitudinal resistivity is measured using four probe method. In the four probe longitudinal resistivity measurements, an AC current is applied through the current terminals (I+ and I-), and simultaneously the voltage drop across the terminals (V+ and V-) is measured as shown in Fig. 2.12 (a). The corresponding resistivity of the voltage drop across the terminals is given by

$$\rho_{xx} = \frac{AV}{lI} \quad (2.7)$$



Figure 2.11: Image of Physical properties measurement system (PPMS, Quantum Design) used to measure the transport properties. The rotator probe and sample puck are shown.

where  $A$  is the cross-sectional area,  $l$  is the distance between the voltage terminals,  $I$  is the magnitude of the current, and  $V$  is the voltage drop across the terminals. The schematic of four probe connections to measure the Hall resistivity (used for Hall devices) is shown in Fig. 2.12 (b). In the four-probe Hall resistivity measurements, one needs to make the voltage connections ( $V+$  and  $V-$ ) exactly opposite to each other. For the bulk samples, it is difficult to make connections with exactly in opposite positions. Slight misalignment can give some longitudinal resistivity contribution in the transverse resistivity data. To overcome this difficulty, five probe method is used to measure the Hall resistivity, as shown in Fig. 2.12 (c). A potentiometer is connected between  $V_a$  and  $V_b$  voltage leads, and before starting the measurements, the potentiometer is tuned to achieve zero voltage drop across the leads. In this way, the longitudinal contribution is reduced significantly in the transverse voltage signal. The availability of two separate channels in the QD PPMS allows one to measure the longitudinal and the transverse resistivity simultaneously. Figure 2.12

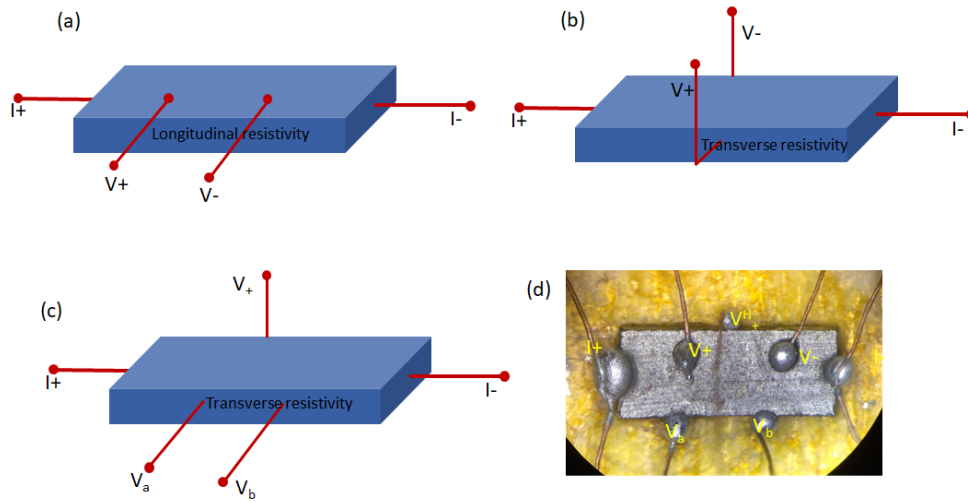


Figure 2.12: Schematic of resistivity measurements. (a) Four probe method for longitudinal resistivity measurements. (b) Transverse resistivity measurements using four probe method. (c) Five probe method for transverse resistivity measurements. (d) Electrical connections between the samples and the current/voltage leads of sample carrier.

(d) shows the electrical connection of the bulk samples with the sample puck for the measurements of the longitudinal and five probe transverse resistivity.

The angular field variation of the Hall resistivity are measured in a horizontal rotator probe available in the PPMS [shown in Fig. 2.11]. The sample is mounted on a puck, and the electrical connections between the electrodes with current/voltage leads are made using a wire bonder. After that, the sample puck is attached to the rotator probe, and it is inserted inside the PPMS chamber. A motor is then attached with the rotator probe, which can rotate the probe from  $0^\circ$  to  $360^\circ$ .

# Chapter 3

## Antiskyrmion phase mapping using Magnetocaloric effect and AC susceptibility study

Study of different types of magnetic phase transitions in magnetic materials requires suitable techniques that are easily available in the laboratory. For instance, the skyrmionic phase transition has been studied in several systems with different microscopic techniques, such as small angle neutron scattering (SANS), Lorentz Transmission Microscopy (LTEM), Scanning tunneling electron microscopy (STEM) and magnetic forced microscopy (MFM), etc. These techniques require advanced sample preparation methods and sophisticated instrumentation to characterize the experiential data. These advanced techniques are not easily accessible to the wider community working in this field. For rapid identification of these spin textures, it is desirable to develop non-destructive techniques accessible in most of the laboratories. In this regard, the present chapter is dedicated to the utilization of some of the well-known phenomena, such as magnetocaloric effect and AC susceptibility study to characterize the magnetic antiskyrmion phase in Mn-Pt(Pd)-Sn system. These two methods need only magnetization measurements and provide deep insight into the thermomagnetic response of the antiskyrmion phase. Another advantage of

these techniques is that one can study the antiskyrmion phase in the bulk limit and across a temperature range spanning from low to above room temperature. In the present chapter, the antiskyrmion phase is studied in  $D_{2d}$  symmetric  $Mn_{1.4}Pt(Pd)Sn$  Heusler system. The structural and magnetic characterizations for the arc melting prepared polycrystalline samples are carried out using XRD and DC magnetization measurements. Isothermal magnetization and AC susceptibility measurements are performed to explore the antiskyrmion phase.

## 3.1 Sample preparation

Polycrystalline  $Mn_{1.4}PtSn$ ,  $Mn_{1.4}Pt_{0.9}Pd_{0.1}Sn$ , and  $Mn_{1.1}PtSn$  samples are prepared in an arc melting furnace under an argon atmosphere. The ingots are melted three to four times to ensure proper mixing of the elements. The prepared ingots are sealed in a quartz tube under the vacuum. The vacuum-sealed ingots are annealed at  $800^\circ C$  for one week and subsequently quenched in an ice-water mixture.

## 3.2 Characterizations

### 3.2.1 Structural characterization (XRD)

The phase purity and the crystal structure of the samples are examined using powder XRD experiments. Figures 3.1 (a)-(c) show the Rietveld refinement of the room-temperature powder XRD patterns. The black scattered data points are the experimental data, and the red lines are the simulated patterns. The green bars represent the Bragg peaks, and the dark yellow line is the difference between the experimental and the simulated XRD patterns. In the XRD pattern, no extra peaks are observed other than the indexed peaks, confirming the single phase present in all the samples. The  $Mn_{1.4}PtSn$  and  $Mn_{1.4}Pt_{0.9}Pd_{0.1}Sn$  crystallize in inverse tetragonal structure with space group  $I\bar{4}2m$  (No. 121), whereas  $Mn_{1.1}PtSn$  crystallizes in cubic structure with  $F\bar{4}3m$  (No. 216). The crystal structure of  $Mn_{1.4}PtSn$  and  $Mn_{1.1}PtSn$

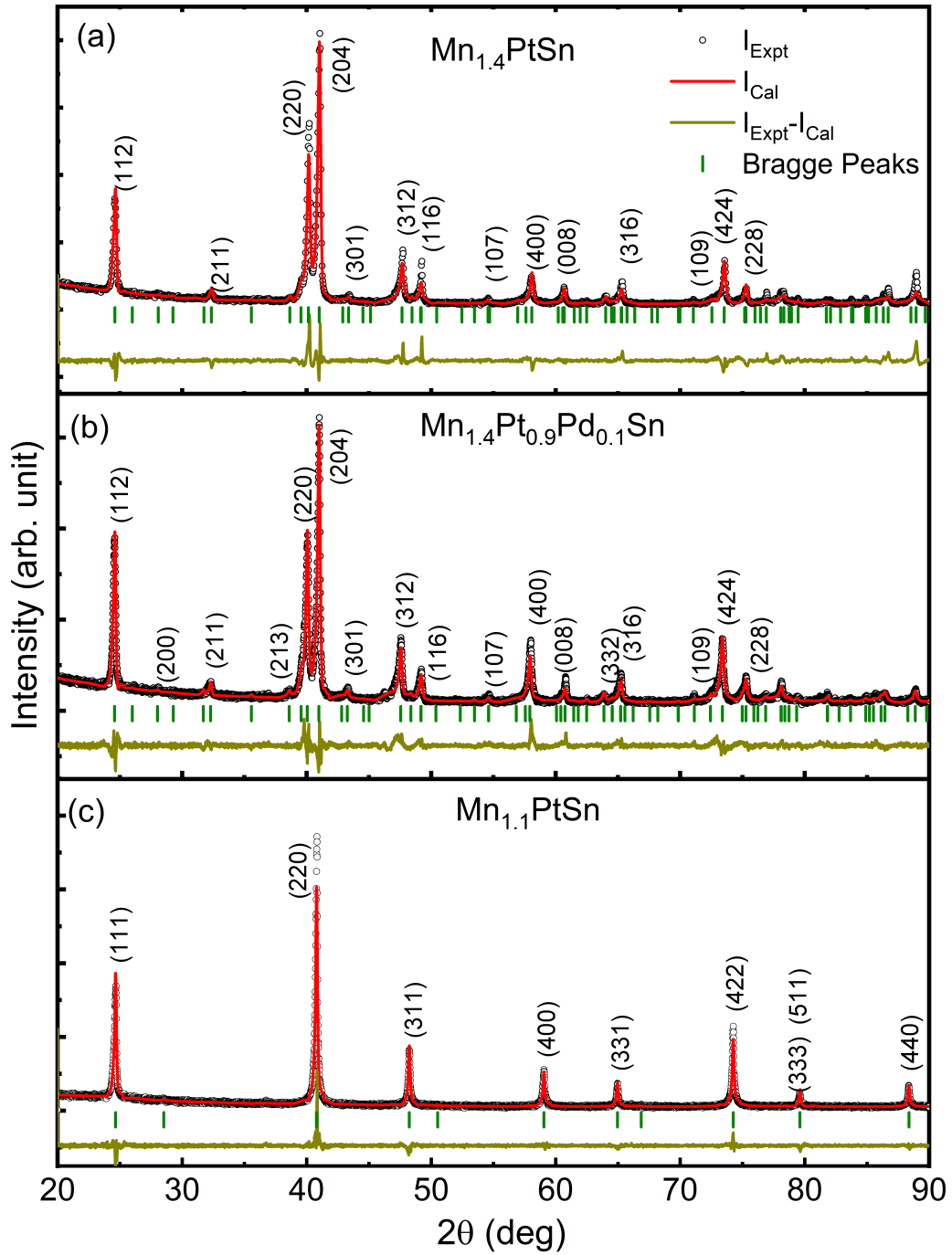


Figure 3.1: Rietveld refinement of powder x-ray diffraction (XRD) of the polycrystalline samples, (a)  $\text{Mn}_{1.4}\text{PtSn}$ , (b)  $\text{Mn}_{1.4}\text{Pt}_{0.9}\text{Pd}_{0.1}\text{Sn}$ , and (c)  $\text{Mn}_{1.1}\text{PtSn}$ .

are depicted in Figs. 3.2 (a)-(b). In  $\text{Mn}_{1.4}\text{PtSn}$ , the Mn atoms fully occupy the 2b  $(0, 0, \frac{1}{2})$  and 8i  $(x, x, z; x=0.29, z=0.63)$  sites, and 4d  $(0, \frac{1}{2}, \frac{1}{4})$  position is partially filled. Sn atoms occupy the 8i  $(x, x, z; x=0.25, z=0.87)$  sites, and Pt atoms sit at

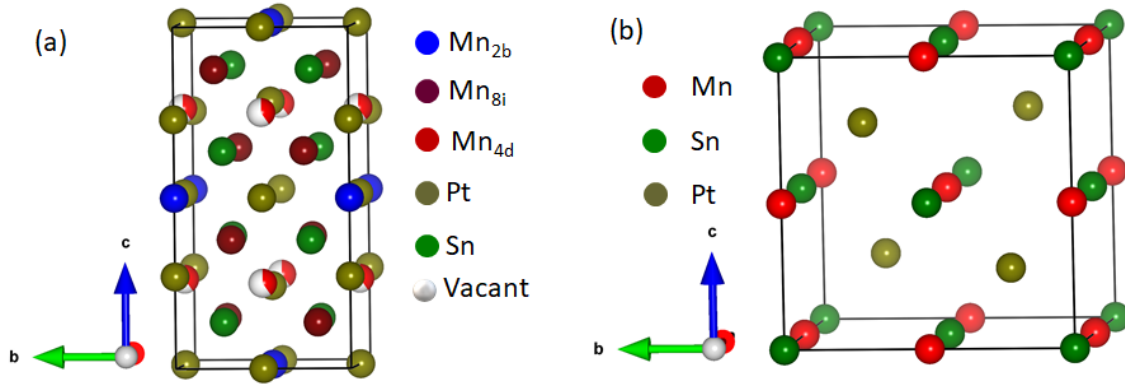


Figure 3.2: (a) Tetragonal crystal structure  $\text{Mn}_{1.4}\text{PtSn}$  having space group  $I\bar{4}2m$  (No 121). (b) Crystal structure of  $\text{Mn}_{1.1}\text{PtSn}$  with space group  $F\bar{4}3m$  (No 216).

$4c$   $(0, \frac{1}{4}, 0)$  and  $4e$   $(0, 0, z=0.73)$  positions. In Pd-doped  $\text{Mn}_{1.4}\text{PtSn}$ , the Pd atoms partially occupy in the Pt positions. In the case of  $\text{Mn}_{1.1}\text{PtSn}$ , Mn, Pt, and Sn atoms occupy  $4b$   $(\frac{1}{2}, \frac{1}{2}, \frac{1}{2})$ ,  $4c$   $(\frac{1}{4}, \frac{1}{4}, \frac{1}{4})$  and  $4a$   $(0, 0, 0)$  positions, respectively. The lattice constant for  $\text{Mn}_{1.4}\text{PtSn}$  are  $a= 6.34 \text{ \AA}$  and  $c= 12.20 \text{ \AA}$  and for  $\text{Mn}_{1.4}\text{Pt}_{0.9}\text{Pd}_{0.1}\text{Sn}$  are  $a= 6.37 \text{ \AA}$  and  $c= 12.21 \text{ \AA}$ . The lattice constant for  $\text{Mn}_{1.1}\text{PtSn}$  is  $a= 6.25 \text{ \AA}$ .

### 3.2.2 SEM and EDS studies

The compositional homogeneity of all the samples are examined using Field Emission Scanning Electron Microscopy (FESEM) and energy dispersive X-ray spectroscopy (EDS) studies. Figure 3.3 depicts the SEM image for all the samples, where a homogeneous phase contrast is observed. The chemical compositions of the samples are shown in table 3.1. The composition of the samples determined from the EDS study nearly matches to that of the initial compositions. The homogeneous contrast in the SEM image confirms the single phase of the samples.

### 3.2.3 Magnetic characterizations

Figures 3.4 (a)-(c) show the zero field-cooled (ZFC) and field-cooled (FC) DC magnetization with the variation of temperature for all the samples. Inset displays the first derivative of the magnetization  $(\frac{dM}{dT})$  with respect to temperature. In

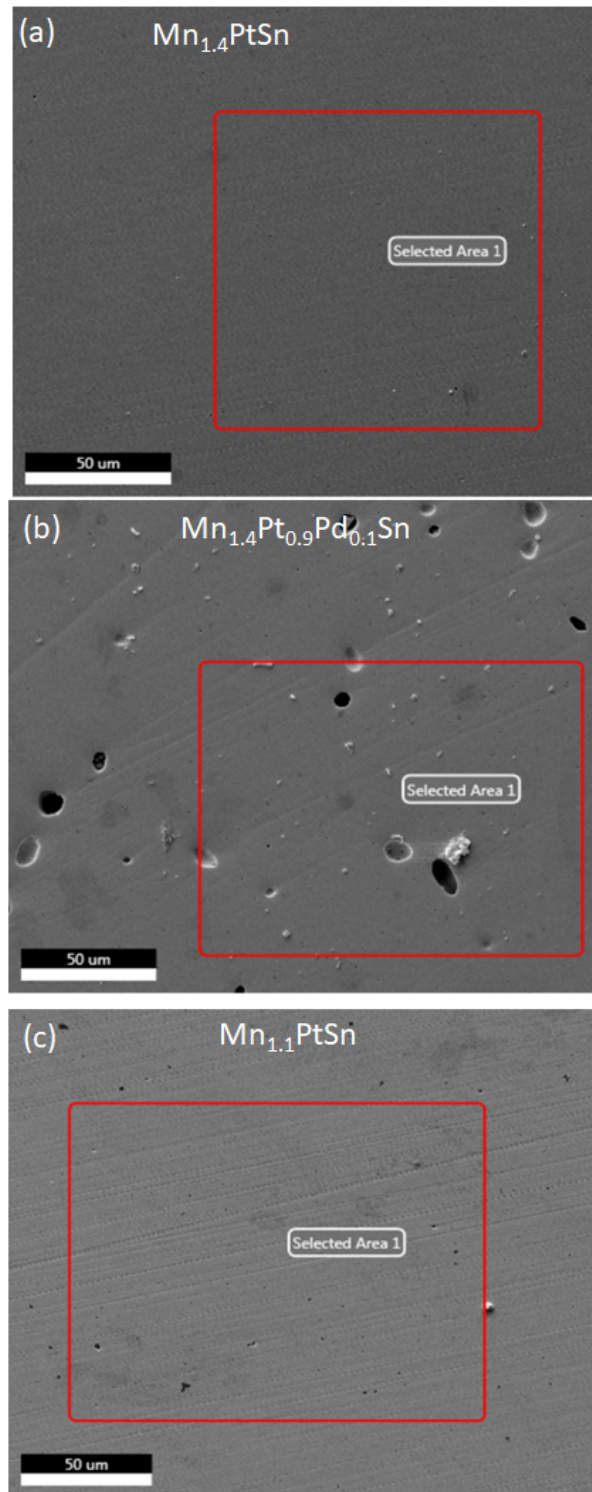


Figure 3.3: Scanning electron microscopy (SEM) images for (a)  $\text{Mn}_{1.4}\text{PtSn}$ , (b)  $\text{Mn}_{1.4}\text{Pt}_{0.9}\text{Pd}_{0.1}\text{Sn}$ , and (c)  $\text{Mn}_{1.1}\text{PtSn}$

Table 3.1: Atomic ratios obtained from EDS measurements

Sample	Starting atomic ratios (%)	Obtained atomic ratios (%)
Mn <sub>1.4</sub> PtSn	Mn- 41.2, Pt- 29.4, Sn- 29.4	Mn- 42.7, Pt- 28.3, Sn- 29.0
Mn <sub>1.4</sub> Pt <sub>0.9</sub> Pd <sub>0.1</sub> Sn	Mn- 41.2, Pt-26.46, Pd- 2.94, Sn-29.4	Mn- 42.6, Pt-25.8, Pd- 2.5, Sn-29.1
Mn <sub>1.1</sub> PtSn	Mn- 35.5, Pt- 32.25, Sn- 32.25	Mn- 37.3, Pt- 30.6, Sn-32.1

Mn<sub>1.4</sub>PtSn and Mn<sub>1.4</sub>Pt<sub>0.9</sub>Pd<sub>0.1</sub>Sn, two transitions are observed; at high temperature, the paramagnetic to ferromagnetic transitions ( $T_C$ ) occurs, and at low temperature, a spin-reorientation transition ( $T_{SR}$ ) appears (at 165 K for Mn<sub>1.4</sub>PtSn and 150 K for Mn<sub>1.4</sub>Pt<sub>0.9</sub>Pd<sub>0.1</sub>Sn). The  $T_C$  for the Mn<sub>1.4</sub>PtSn and Mn<sub>1.4</sub>Pt<sub>0.9</sub>Pd<sub>0.1</sub>Sn is 395 K and 375 K, respectively. At high temperatures, the Mn atoms at the 8i site give larger magnetic moments and are aligned antiparallel with Mn at 2b and 4d sites having smaller magnetic moments. The antiparallel alignments and the presence of Dzyaloshinskii–Moriya interaction (DMI) stabilize the helical spin structure along [100] and the cycloid spin structure along [110]. Previous neutron diffraction study [1] shows the reorientation of magnetic moments at low temperatures, giving rise to the formation of a non-collinear spin structure. The  $T_C$  of Mn<sub>1.1</sub>PtSn is about 340 K, and no other transition is observed in this sample. Figures 3.4 (d)-(f) show the field-dependent magnetization ( $M(H)$ ) at 2 K (black curve) and 300 K (red curve) for all the samples. The magnetic moment of Mn<sub>1.4</sub>PtSn and Mn<sub>1.4</sub>Pt<sub>0.9</sub>Pd<sub>0.1</sub>Sn is almost same and it is about  $4.7 \mu_B/f.u$  at 2 K. The magnetic moment of Mn<sub>1.1</sub>PtSn is  $3.5 \mu_B/f.u$  at 2 K.

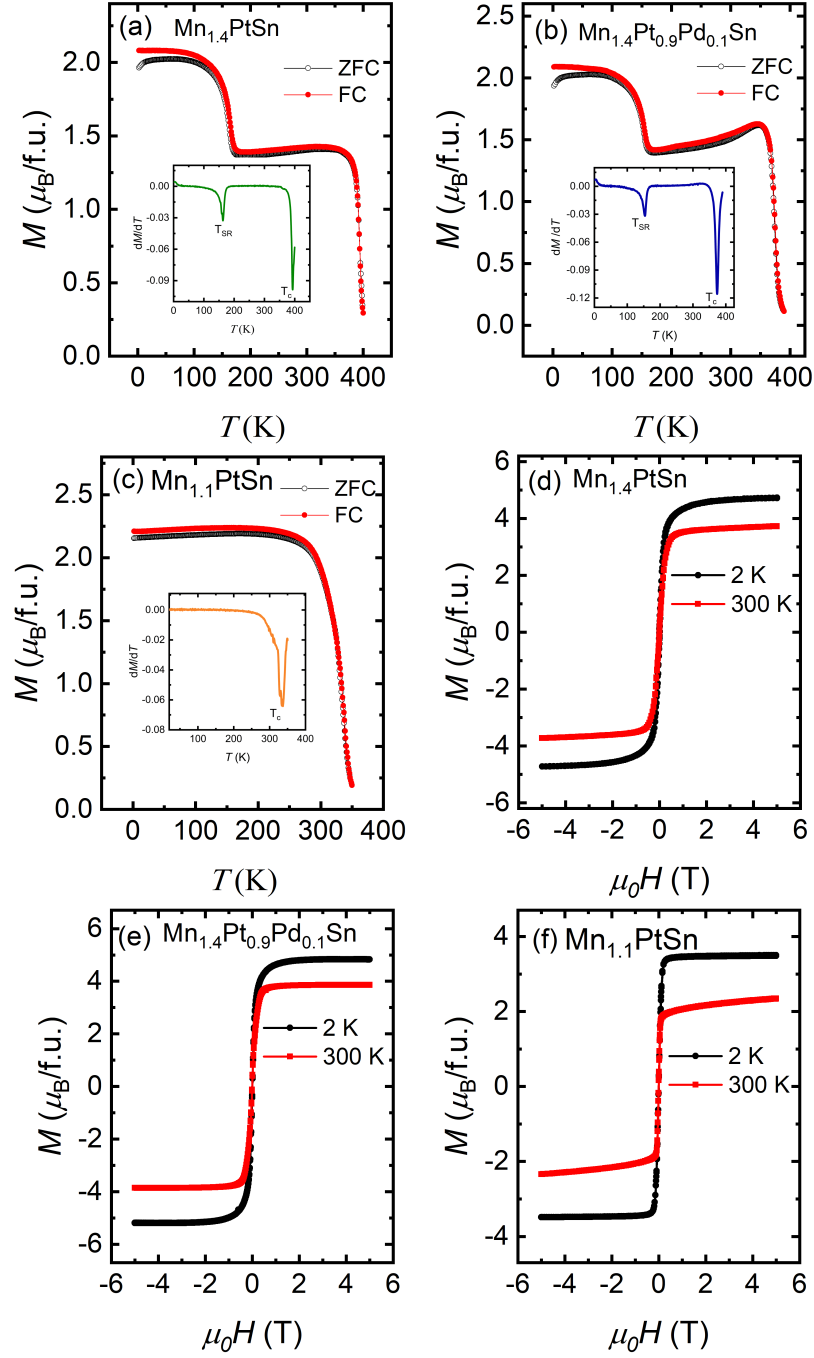


Figure 3.4: Magnetization measurements. Temperature variation of zero field-cooled (ZFC, open symbols) and field-cooled (FC, close symbols) DC magnetization curve measured with an applied field of 0.1 T for (a)  $\text{Mn}_{1.4}\text{PtSn}$ , (b)  $\text{Mn}_{1.4}\text{Pt}_{0.9}\text{Pd}_{0.1}\text{Sn}$ , and (c)  $\text{Mn}_{1.1}\text{PtSn}$ . Inset depicts the first derivative of DC magnetization with temperature. Field variation of magnetization loop at 2 K (black curve) and 300 K (red curve) for (d)  $\text{Mn}_{1.4}\text{PtSn}$ , (e)  $\text{Mn}_{1.4}\text{Pt}_{0.9}\text{Pd}_{0.1}\text{Sn}$  and (f)  $\text{Mn}_{1.1}\text{PtSn}$ .

### 3.3 Magnetic entropy measurements

In order to calculate the magnetic entropy ( $\Delta S_M$ ) change during the phase transition, isothermal magnetization measurements are conducted using SQUID VSM for all the samples at various temperatures. Figures 3.5 (a)-(c) depict the isothermal magnetization curves with a temperature interval of 5 K as is indicated in the figures. Before taking the measurements, each time the sample temperature is increased above the  $T_C$  and then back to the target temperature to take the M-H curve. This is done to remove any remnant magnetization. From the isothermal magnetization measurements, the magnetic entropy change  $\Delta S_M$  is calculated utilizing the relation 1.22. The magnetic entropy changes with the temperature at various magnetic fields are plotted in Figs. 3.5 (d)-(f) for  $\text{Mn}_{1.4}\text{PtSn}$ ,  $\text{Mn}_{1.4}\text{Pt}_{0.9}\text{Pd}_{0.1}\text{Sn}$ , and  $\text{Mn}_{1.1}\text{PtSn}$ , respectively. The change in the magnetic entropy near the  $T_C$  is negative for all three samples. This is because, at  $T_C$ , the magnetically disordered paramagnetic state undergoes the phase transition to a magnetically ordered ferromagnetic state. The magnetic entropy in the paramagnetic state is more than the ferromagnetic state. Therefore, during the paramagnetic to ferromagnetic phase transition, a negative  $\Delta S_M$  is observed. Below the  $T_C$ , a positive  $\Delta S_M$  is found for the antiskyrmion host systems  $\text{Mn}_{1.4}\text{PtSn}$  and  $\text{Mn}_{1.4}\text{Pt}_{0.9}\text{Pd}_{0.1}\text{Sn}$ . The better visualization of positive  $\Delta S_M$  can be seen in Figs. 3.5 (g)-(h). Below  $T_C$ , the helical spin texture gets stabilized for  $\text{Mn}_{1.4}\text{PtSn}$  and  $\text{Mn}_{1.4}\text{Pt}_{0.9}\text{Pd}_{0.1}\text{Sn}$ . The Application of a magnetic field transforms the helical spin textures into an antiskyrmion lattice, as previously found in the LTEM study [1]. Since the helical phase is magnetically more ordered than the antiskyrmion phase, the magnetic entropy in the antiskyrmion phase is larger than the helical phase. The positive value of  $\Delta S_M$  below the  $T_C$  implies the formation of the antiskyrmion phase from the helical phase. The positive  $\Delta S_M$  persists down to the  $T_{SR}$ , and up to a magnetic field of 0.8-0.9 T. Below the  $T_{SR}$ , the  $\Delta S_M$  becomes negative as in this region the antiskyrmion phase is not stabilized. At a higher field, the field-polarized state emerges where the magnetic entropy is less compared to the antiskyrmion phase leading to a negative value of  $\Delta S_M$ .

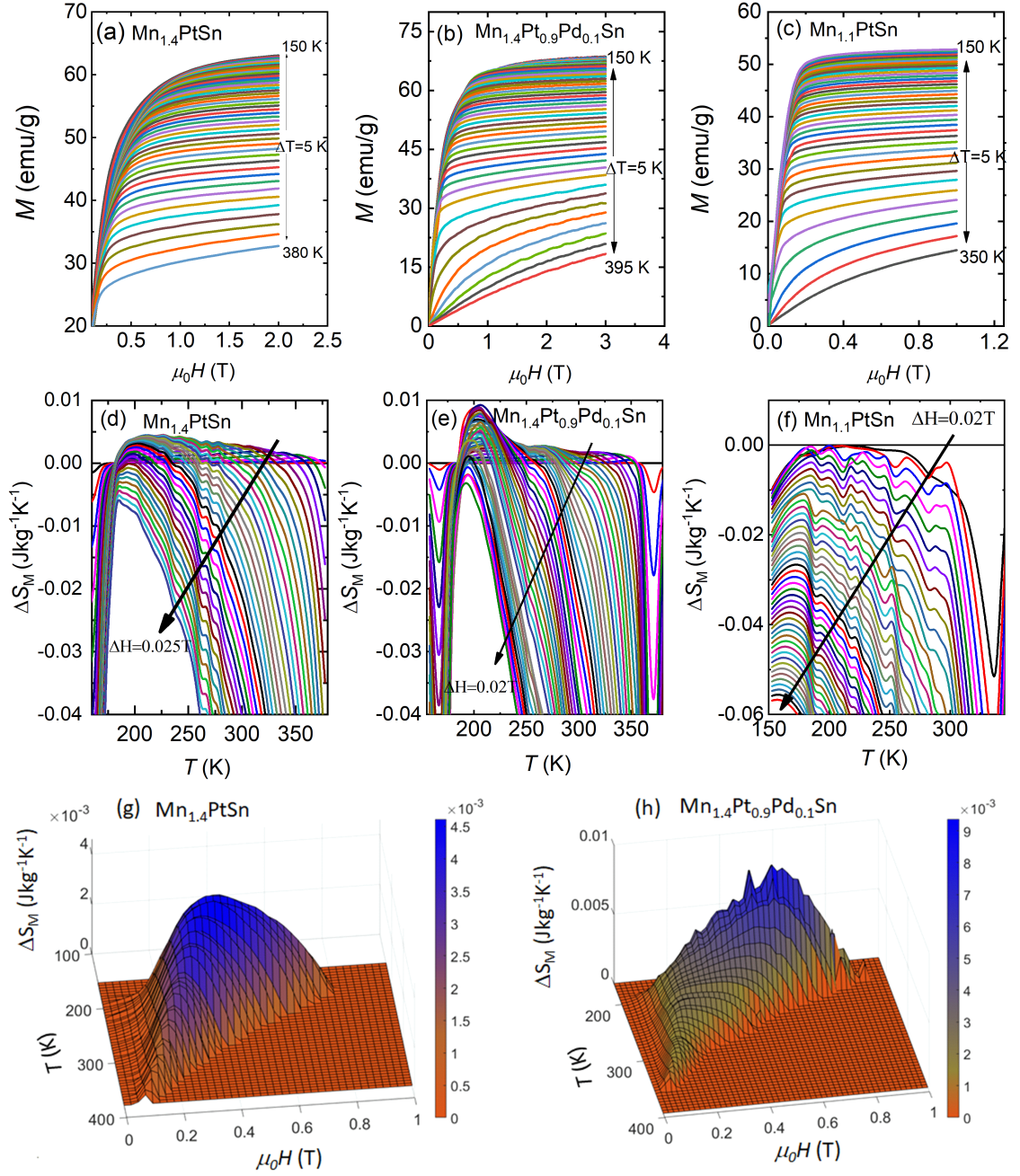


Figure 3.5: Isothermal magnetization curves as a function of the magnetic field at different temperatures for (a)  $\text{Mn}_{1.4}\text{PtSn}$ , (b)  $\text{Mn}_{1.4}\text{Pt}_{0.9}\text{Pd}_{0.1}\text{Sn}$ , and (c)  $\text{Mn}_{1.1}\text{PtSn}$ . The temperature range and the temperature interval ( $\Delta T$ ) are indicated in the figure. Change of magnetic entropy  $\Delta S_M$  as a function of temperature in a field range from 0.02 T to 1 T for (d)  $\text{Mn}_{1.4}\text{PtSn}$ , (e)  $\text{Mn}_{1.4}\text{Pt}_{0.9}\text{Pd}_{0.1}\text{Sn}$ , and (f)  $\text{Mn}_{1.1}\text{PtSn}$ . 3D illustration of positive magnetic entropy change  $\Delta S_M$  for (g)  $\text{Mn}_{1.4}\text{PtSn}$  and (h)  $\text{Mn}_{1.4}\text{Pt}_{0.9}\text{Pd}_{0.1}\text{Sn}$ .

From the magnetic entropy calculation, it is found that the positive  $\Delta S_M$  appears only in the antiskyrmion phase. For comparison, the magnetic entropy change is also calculated for the sister compounds  $\text{Mn}_{1.1}\text{PtSn}$ . In this case, only negative  $\Delta S_M$  is observed [Fig 3.5 (f)] in the whole temperature regime. The high cubic symmetry of this compound does not favor any DMI. Hence no antiskyrmion is expected for  $\text{Mn}_{1.1}\text{PtSn}$ . Thus in the whole temperature range, only negative entropy change is observed. This confirms that the positive entropy change emerges due to the formation of the antiskyrmion phase from the helical phase.

### 3.4 AC Susceptibility study

Further, to probe the antiskyrmion phase and to study their response under an AC magnetic field, the field-dependent AC susceptibility  $\chi'(H)$  measurements are performed. The AC susceptibility measurements are carried out for all three samples at different temperatures with an applied AC field of 10 Oe and frequency of 331 Hz. Figures 3.6 (a) - (g) and Figures 3.7 (a) - (f) depict the DC field variation of the real part of AC susceptibility  $\chi'(H)$  at different temperatures for  $\text{Mn}_{1.4}\text{PtSn}$  and  $\text{Mn}_{1.4}\text{Pt}_{0.9}\text{Pd}_{0.1}\text{Sn}$ , respectively. The AC susceptibility  $\chi'(H)$  at low temperature (below  $T_{SR}$ ) exhibit normal behavior as observed in a ferromagnetic system. Interestingly, above the  $T_{SR}$ , peaks/humps anomalies are observed in the  $\chi'(H)$  marked by the black arrows. These peaks/humps kind of anomalies are found in both the positive and negative field regimes. The emergence of the anomaly in  $\chi'(H)$  illustrates the presence of distinct magnetic states. The peaks/humps demonstrate the creation/annihilation of antiskyrmions during the field sweep. During the formation/annihilation of the antiskyrmion phase, the magnetic configuration in the system changes from helical or ferromagnetic arrangements to antiskyrmion phase or vice-versa, resulting in the observed peaks/humps in the  $\chi'(H)$ . The peak/hump in the low field illustrates the transition from helical to antiskyrmion phase, and at the high field, the anomaly depicts the transformation from antiskyrmions to field polarized state.

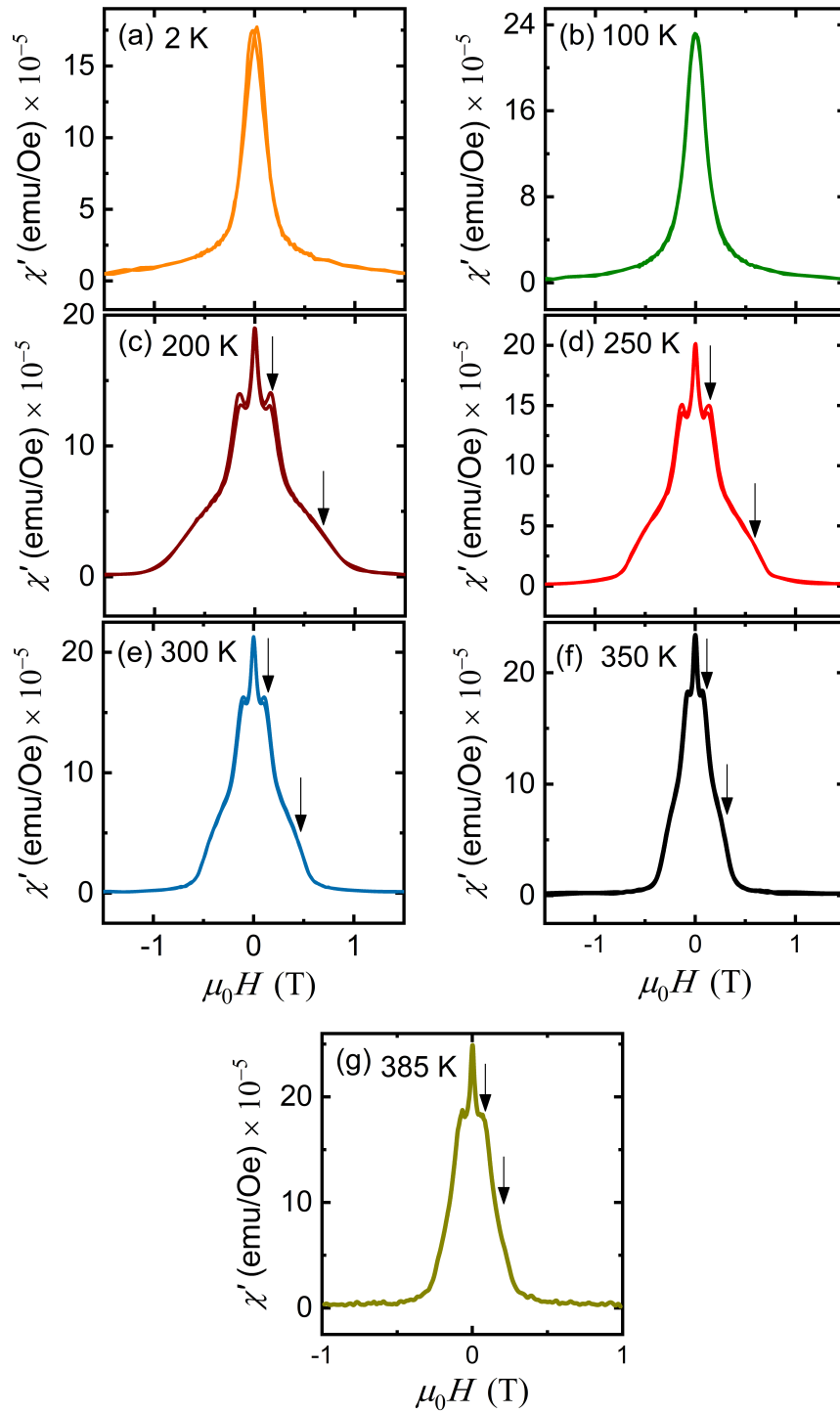


Figure 3.6: (a)- (g) Magnetic field variation of real part of AC susceptibility [ $\chi'$  (H)] at different temperatures for the  $\text{Mn}_{1.4}\text{PtSn}$ . The measurement temperatures are indicated in the figure. The black arrow depicts the anomaly peak/hump kind of feature.

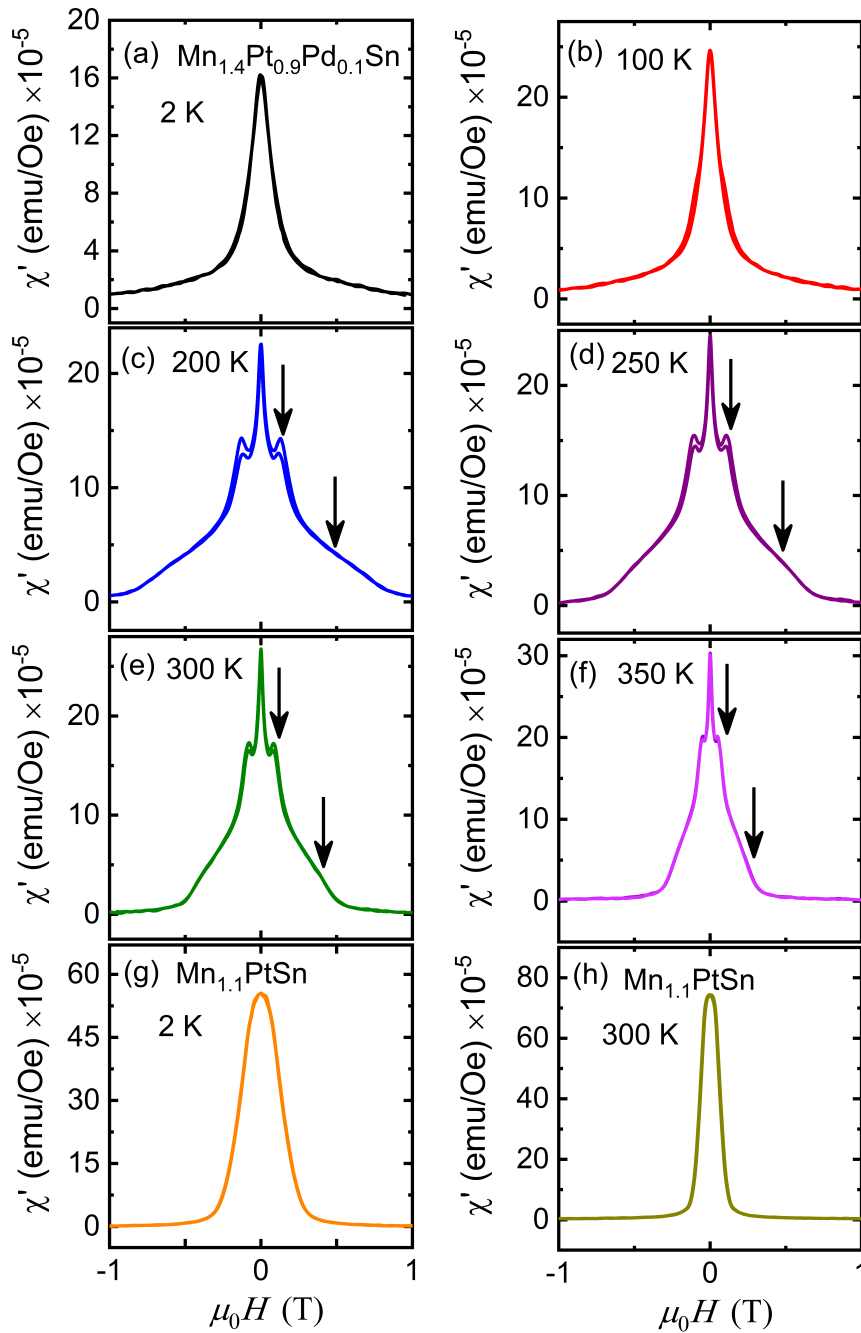


Figure 3.7: (a) - (f) Magnetic field variation of real part of AC susceptibility [ $\chi'$  (H)] at different temperatures for  $\text{Mn}_{1.4}\text{Pt}_{0.9}\text{Pd}_{0.1}\text{Sn}$ . (g)-(h) Magnetic field variation of real part of AC susceptibility [ $\chi'$  (H)] for  $\text{Mn}_{1.1}\text{PtSn}$ . The measurement temperatures are indicated in the figure. The Black arrows depict the anomaly peak/hump kind of feature.

At low field, a hysteric behavior is observed in the peak/hump. This is because the creation and annihilation field of antiskyrmions is different during field increasing

/decreasing sweep. Figures 3.7 (g) -(h) represent the  $\chi'(H)$  at 2 K and 300 K for  $\text{Mn}_{1.1}\text{PtSn}$ . In comparison to the antiskyrmion host samples, no such anomalies are observed for  $\text{Mn}_{1.1}\text{PtSn}$ . This confirms that the appearance of peaks/humps in  $\text{Mn}_{1.4}\text{PtSn}$  and  $\text{Mn}_{1.4}\text{Pt}_{0.9}\text{Pd}_{0.1}\text{Sn}$  correspond to the existence of antiskyrmions in these systems.

### 3.5 Phase diagram of Antiskyrmion state

The exhibition of positive magnetic entropy change in the magnetic entropy measurements and the emergence of the anomalies in the  $\chi'(H)$  data are utilized to construct the temperature-field ( $H - T$ ) phase diagram of the antiskyrmion state for both samples. Figures 3.8 (a) - (b) illustrate the  $H - T$  phase diagram derived from the magnetocaloric measurements. The positive magnetic entropy changes  $\Delta S_M$  or the antiskyrmion phase exist over a wide temperature-field range. At low temperature, the antiskyrmion phase stabilized to a higher field region. The antiskyrmion phase for  $\text{Mn}_{1.4}\text{PtSn}$  persists up to 0.8 T, while for  $\text{Mn}_{1.4}\text{Pt}_{0.9}\text{Pd}_{0.1}\text{Sn}$  the antiskyrmion phase exists up to 0.9 T. Furthermore, the  $H - T$  phase diagram depicted in Figures 3.8 (c)-(d) for both  $\text{Mn}_{1.4}\text{PtSn}$  and  $\text{Mn}_{1.4}\text{Pt}_{0.9}\text{Pd}_{0.1}\text{Sn}$  systems are drawn based on the AC susceptibility studies. The hump/peak in the low and high field regions are taken as the boundary for the antiskyrmion phase. The region of the antiskyrmion phase drawn from the AC susceptibility studies is identical to the phase diagram realized from the magnetic entropy measurements. The phase diagrams obtained using magnetic entropy measurements and AC susceptibility studies are in good agreement with the phase diagram constructed using the LTEM study [1]. A slight deviation in the field range between the present study with the reported one possibly arising due to the bulk sample used for the present study, whereas the LTEM measurements are carried out in a thin sample plate of about 100 nm thickness.

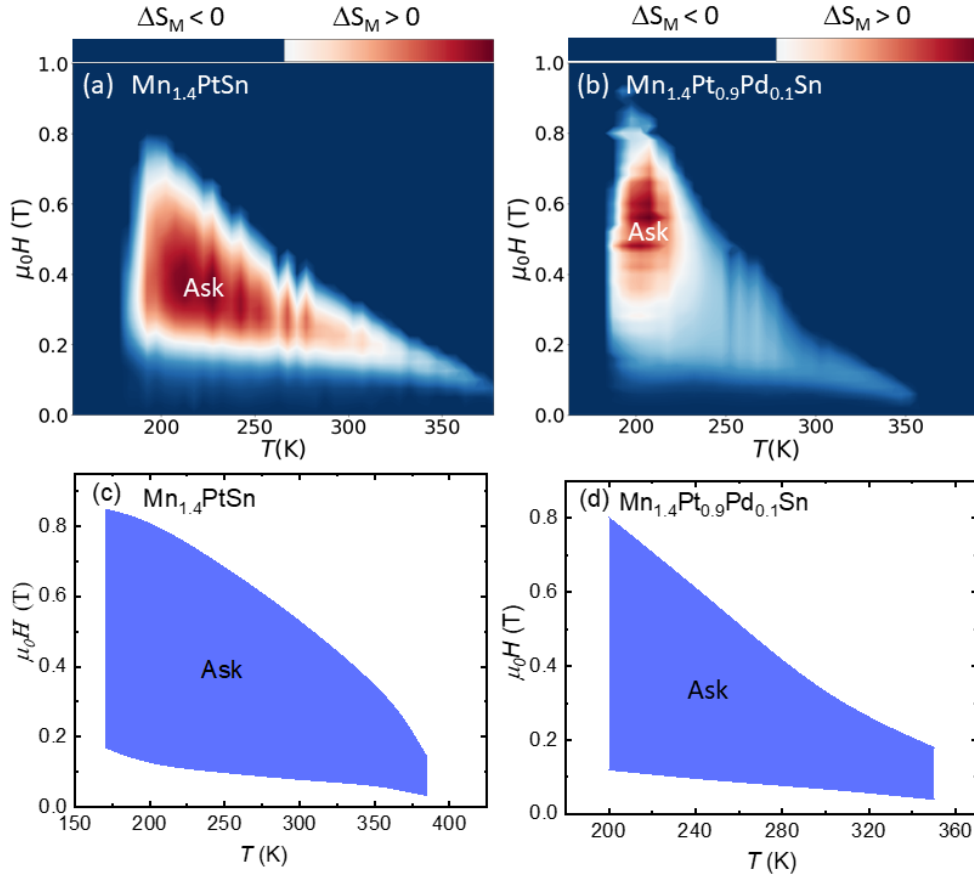


Figure 3.8: (a)-(b) Temperature - field ( $H - T$ ) phase diagram of anti-skyrmion phase constructed using the magnetic entropy change for  $\text{Mn}_{1.4}\text{PtSn}$  and  $\text{Mn}_{1.4}\text{Pt}_{0.9}\text{Pd}_{0.1}\text{Sn}$ , respectively. Negative and positive magnetic entropy changes are ( $\Delta S_M$ ) shown in the color bar. (c)-(d) Temperature-field ( $H - T$ ) phase diagram of antiskyrmion phase derives from field-dependent AC susceptibility measurements for  $\text{Mn}_{1.4}\text{PtSn}$  and  $\text{Mn}_{1.4}\text{Pt}_{0.9}\text{Pd}_{0.1}\text{Sn}$ , respectively.

### 3.6 Summary

The rapid DC magnetization measurements are performed to map the antiskyrmion phase in bulk  $\text{Mn}_{1.4}\text{PtSn}$  and  $\text{Mn}_{1.4}\text{Pt}_{0.9}\text{Pd}_{0.1}\text{Sn}$  compounds. The thermomagnetic response, such as magnetic entropy change and AC susceptibility studies, are performed to illustrate the stabilization of magnetic antiskyrmion in a bulk sample. A clear positive magnetic entropy change is observed, which is the entropic signature of transitions from a non-topological magnetic state to a topological antiskyrmion state. The magnetic entropy measurements helps us to draw clear thermodynamic

---

phase boundaries in these systems. Furthermore, the observation of anomalies in the AC susceptibility study acts as an additional tool to probe these magnetic states. In contrast, the cubic  $\text{Mn}_{1.1}\text{PtSn}$  sample does not show either a positive magnetic entropy change or anomaly in the AC susceptibility data. This again validates the present methods for the identification of skyrmion/antiskyrmion phase. The techniques employed in this study can be utilized for the rapid identification of skyrmion/antiskyrmion phases in other systems, even above room temperature, with a bulk sample.



## Chapter 4

# Stability and phase evolution of Antiskyrmions in $D_{2d}$ symmetric Mn-Ni-Ga Heusler alloy

As discussed in Chapter 1, the complex non-trivial magnetization distribution of antiskyrmion greatly influences the motion of conduction electrons moving through it. The previous chapter focused on the characterization of antiskyrmion phase in Mn-Pt(Pd)-Sn system using some special techniques. The large size of antiskyrmions in Mn-Pt(Pd)-Sn system may act as an obstacle for their implementation in high density storage medium. In recent studies, it is proposed that the polycrystalline samples of  $\text{Mn}_{2+x}\text{Ni}_{1-x}\text{Ga}$ , which possess  $D_{2d}$  symmetry, exhibit small-size antiskyrmions of about 10 nm. [2, 3]. In addition, this system exhibits a very small magnetic moment, which is critical for minimizing the dipolar field. Hence Mn-Ni-Ga system makes an appealing case for future high-density data storage devices. The present chapter focuses on the stability and phase evolution of the antiskyrmion phase by measuring the electrical transverse resistivity in the  $D_{2d}$  symmetric Mn-Ni-Ga Heusler system. The presence of magnetic skyrmion/antiskyrmion gives an additional Hall voltage in the transverse electrical signal. This additional Hall voltage is called the topological Hall effect (THE), which is the electrical footprint of

magnetic skyrmion/antiskyrmion. The topological Hall effect has been proven to be an efficient tool for identifying very smaller sizes of magnetic skyrmion/antiskyrmion in a wider temperature-field range. Additionally, it enables one to investigate the stability and phase evolution of these objects subjected to various external perturbations. The topological Hall effect has been observed in several skyrmion host systems, and their stability under an oblique magnetic field has been investigated in limited systems. In B20 materials, the skyrmion phase is easily destroyed with a small in-plane magnetic field component [98, 139]. Although the antiskyrmion textures also annihilate under an in-plane field, it is experimentally verified that a small in-plane magnetic field is necessary to stabilize the antiskyrmion in  $D_{2d}$  materials [1, 140]. This is because of the nature of anisotropic DMI present in these types of systems. After the first experimental observation of antiskyrmion, extensive efforts have been directed toward investigating the antiskyrmion phase in various systems [57, 62, 141]. However, the stability of this phase under the influence of an oblique magnetic field remains unexplored. Therefore, it is necessary to study the antiskyrmion phase under a tilted magnetic field, which will enlighten the stability of antiskyrmions in  $D_{2d}$  materials. In this context, the present study utilized micron-size devices fabricated from a single crystalline grain of polycrystalline  $D_{2d}$  symmetric Mn-Ni-Ga system. In the following chapter, the orientations of the Hall devices fabricated from a single grain, along with the observation of topological Hall and its evolution under oblique fields, are presented. In the end, the directional dependence of Hall resistivity and the micro-structural characterization are demonstrated.

## 4.1 Structural and magnetic properties of $\text{Mn}_{2+x}\text{Ni}_{1-x}\text{Ga}$

$\text{Mn}_{2+x}\text{Ni}_{1-x}\text{Ga}$  ( $x \geq 0.13$ ) system undergoes a martensite phase transition from a high-temperature cubic phase (space group  $F\bar{4}3m$ ) to a tetragonal phase (space group  $I\bar{4}m2$ ) above 750 K [3]. Below this temperature, the samples crystallize only in the tetragonal phase.

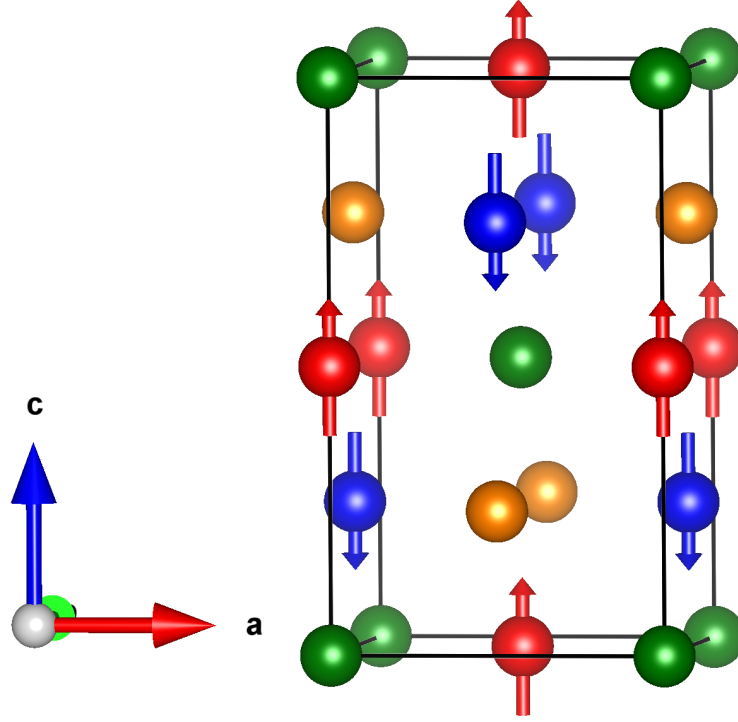


Figure 4.1: Tetragonal crystal structure of  $\text{Mn}_2\text{NiGa}$  with space group  $\bar{I}4m2$  (No. 119). MnI, MnII, Ni, and Ga atoms are represented by the red, blue, orange, and green atoms, respectively.

For  $x=0$ , the martensite transition is 350 K, and at room temperature both cubic and tetragonal phases co-exist. The unit cell of  $\text{Mn}_2\text{NiGa}$  with space group  $\bar{I}4m2$  (No. 119) is shown in Fig. 4.1. The Ga atoms (green balls) sit at  $2a$   $(0, 0, 0)$ , and Ni atoms (orange balls) occupy the position  $2d$   $(0, \frac{1}{2}, \frac{3}{4})$ . The MnI atoms (red balls) and the second MnII atoms (blue balls) prefer the  $2b$   $(0, 0, \frac{1}{2})$  and  $2c$   $(0, \frac{1}{2}, \frac{1}{4})$  positions, respectively. In the  $\text{Mn}_{2+x}\text{Ni}_{1-x}\text{Ga}$  compounds, the excess Mn atoms go to the Ni site. With increasing the Mn percentage, the martensite transition shifts to higher temperatures. The Curie temperature ( $T_C$ ) for all the samples lies above 600 K. The saturation magnetization at 3 K for  $x=0$  is  $1.43 \mu_B/f.u$  and decreases with increasing the Mn percentage [3]. In  $\text{Mn}_2\text{YZ}$ -based Heusler alloys, the Mn atoms sitting at the Mn-Z plane show a larger moment in comparison to that of the Mn atoms sitting at the Mn-Y plane [101, 142, 143]. These two Mn atoms align antiferromagnetically to give a resultant ferrimagnetic ordering in the system. In the  $\text{Mn}_{2+x}\text{Ni}_{1-x}\text{Ga}$ , the excess Mn atoms occupy the Mn-Y (Mn-Ni) plane, resulting in a

decrease in saturation magnetization. For the present work, polycrystalline sample with  $x= 0.13$  is utilized to prepare the single crystalline devices. The saturation magnetization for this sample is about  $0.9 \mu_B/f.u$  at 3 K [3].

## 4.2 Geometry of Hall devices

The observation of topological Hall signal and anomalies in the AC susceptibility study proposed the existence of possible antiskyrmion phase in the polycrystalline  $Mn_{2+x}Ni_{1-x}Ga$  system [2, 3]. A drawback associated with polycrystalline materials is the presence of multiple grains with different orientations. These grains give different anomalous Hall responses and suppress overall topological Hall signal originating from the antiskyrmion phase. The antiskyrmion phase in  $D_{2d}$  symmetric materials gets stabilized when the field is applied along [001]. The present study aims to explore the stability and phase evolution of the antiskyrmsions under an oblique field. This requires single crystalline specimens with specific crystallographic orientation. In this regard, micron-size devices with specific crystallographic orientations are fabricated using Focused Ion Beam (FIB) technique mentioned in Chapter 2. The Electron Backscatter Diffraction (EBSD) technique is used to identify the single crystalline grain from the polycrystalline sample  $Mn_{2.13}Ni_{0.87}Ga$ . Figure 4.2 (a) shows the inverse pole figure of EBSD mapping. The green color region represents the single crystalline grain of [100] orientation. The geometry of the EBSD pattern indicates that the surface perpendicular to the green region is [100]. Hall devices with two different geometry, out-of-plane and in-plane orientation, are prepared from this single grain [shown in 4.2 (b)]. Figures 4.2 (c) and (d) show the false color SEM image of the out-of-plane and the in-plane devices fabricated from areas 1 and 3, respectively, shown in Fig. 4.2 (b). For the out-of-plane device, the surface is perpendicular to [001], the length is along [010], and the breadth is along [100]. The dimension of the device is  $16 \mu m \times 3.6 \mu m \times 1.1 \mu m$ . In case of the in-plane device, the surface is perpendicular to [010], the length is along [001], and the breadth is along [100]. The dimension of the device is  $17 \mu m \times 3.3 \mu m \times 975 \text{ nm}$ . The

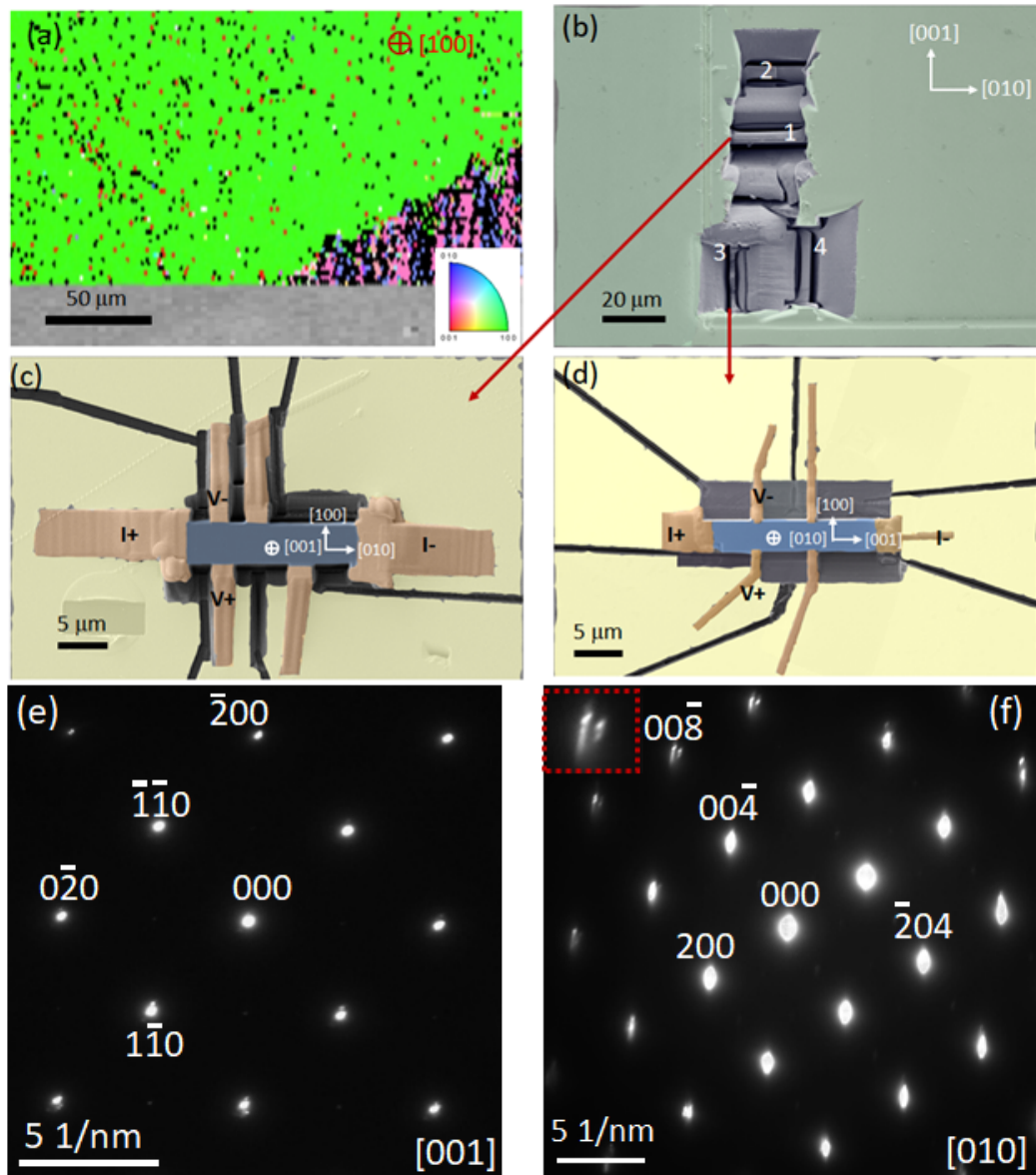


Figure 4.2: Orientation of Hall devices. (a) Electron Backscatter Diffraction (EBSD) pattern of polycrystalline  $\text{Mn}_{2.13}\text{Ni}_{0.87}\text{Ga}$ . The orientation of the green color region is  $[100]$ . (b) SEM image of the single crystalline grain ( $[100]$ ) from where the Hall bars (from areas 1 and 3) and TEM specimens (from areas 2 and 4) are prepared. (c)-(d) False-color SEM images of the out-of-plane and the in-plane devices, respectively. The crystallographic directions, current, and voltage connections are shown in the figure. The light yellow regions are the gold electrodes. (e) Selected Area Electron Diffraction (SAED) pattern collected for the sample specimen prepared from area-2 with out-of-plane orientation. (f) SAED pattern collected for the in-plane orientation with TEM sample prepared from area-4. Inset under the red dashed area shows the magnifying view of  $(00\bar{8})$  spot.

orientations of the devices are verified utilizing Selected Area Electron Diffraction (SAED) patterns. The TEM specimens are prepared from the adjacent area from where the Hall bars are fabricated, shown in Fig. 4.2 (b). The TEM samples for out-of-plane and in-plane orientations are prepared from areas 2 and 4, respectively. Figure 4.2 (e) shows the SAED pattern for the out-of-plane orientation, which confirms the normal direction of the out-of-plane device along the  $[001]$  direction. The SAED pattern corresponding to the in-plane orientation is illustrated in Fig. 4.2 (f), confirming alignment along the  $[010]$  direction. In the in-plane orientations, the diffraction spots are found to be elongated and consist of double spots (shown in the inset under the red dashed area). The presence of twin crystal structures often found in these materials give this kind of diffraction pattern. [116, 117, 118].

### 4.3 Longitudinal resistivity of out-of-plane and in-plane devices

The temperature-dependent zero-field longitudinal resistivity for both the out-of-plane  $[\rho_{xx}(T)]$  and in-plane  $[\rho_{zz}(T)]$  devices are shown in Figs. 4.3 (a)-(b). For the out-of-plane Hall geometry current is applied along the  $ab$  plane ( $I // ab$ ), and for the in-plane sample current is applied along the  $c$ -axis ( $I // c$ ). The resistivity measurements show that with decreasing temperature, the resistivity decreases for both the Hall devices, indicating the metallic nature of these samples. The resistivity for the in-plane device is slightly larger than for the out-of-plane device. This is due to the presence of twin structures in this direction. Figures 4.3 (c) and (d) depict the field-dependent longitudinal resistivity for the out-of-plane ( $\rho_{xx}(H)$ ) and in-plane ( $\rho_{zz}(H)$ ) devices. For the OP device, magnetic field is applied along the  $c$ -axis ( $H//c$ ) and current is applied in the  $ab$ -plane. In this case, the change in  $\rho_{xx}$  is negligibly small. In the case of IP device, where the magnetic field is applied along the  $[010]$  direction and current is applied along the  $c$ -axis, a small increase in the resistivity is observed with increasing the field. The change in resistance is about

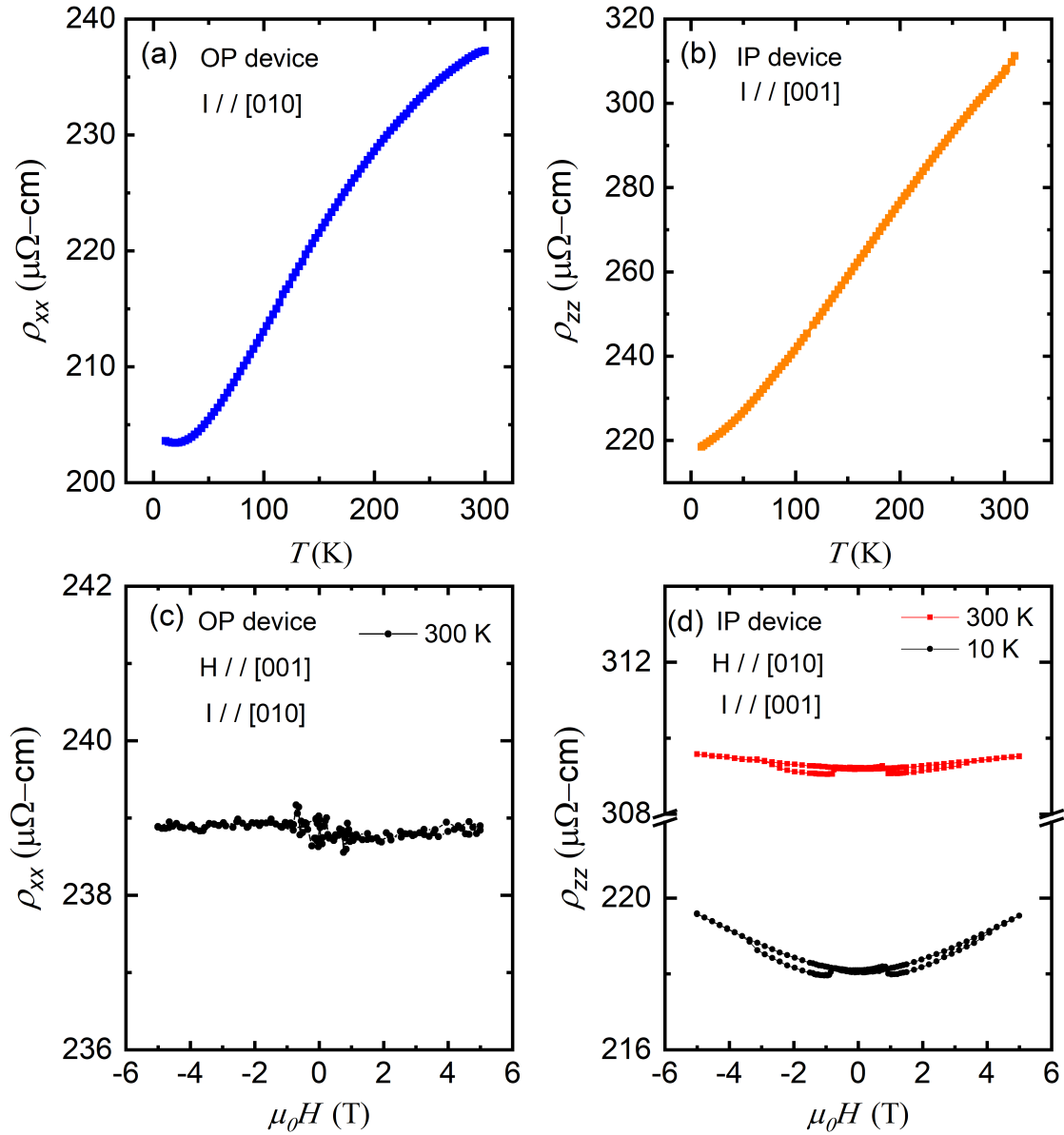


Figure 4.3: Temperature variation of longitudinal resistivity for (a) out-of-plane [ $\rho_{xx}(T)$ ] and (b) in-plane [ $\rho_{zz}(T)$ ] devices. Field-dependent longitudinal resistivity for (c) out-of-plane [ $\rho_{xx}(H)$ ] and (d) in-plane [ $\rho_{zz}(H)$ ] devices.

0.7% at 2. A small hysteretic behavior is observed during the field sweep, which can be assigned to the presence of twin domains in this direction.

## 4.4 Topological Hall effect in the out-of-plane orientation

In order to study the antiskyrmion phase, the field-dependent Hall resistivity measurements are carried out for the out-of-plane Hall device. Figures 4.4 (a)-(f) depict the field variation of Hall resistivity  $[\rho_{xy}(H)]$  at different temperatures for the out-of-plane device. In the high field regions, the Hall resistivity saturates and shows normal anomalous Hall behavior. In the low field region, dip-like anomalies are observed as marked by stars, which persist down to low temperatures. The dip-like feature in the Hall resistivity data is a signature of the topological Hall effect. The emergence of the topological Hall effect confirms the existence of non-coplanar spin textures such as antiskyrmions. The observed topological Hall signal over a wide temperature-field range suggests the presence of antiskyrmions in a broad temperature-field region. During the field sweep, at low field region, the nucleation of antiskyrmion occurs, which is associated with the modification in the local magnetization. The change in the local magnetization is manifested as the dip anomaly in the Hall resistivity. At the high field region, the antiskyrmion phase annihilates, and only the field polarized state stabilizes. The exact magnitude of the topological Hall resistivity can not be measured for the present study as it requires the magnetization measurements of the single crystalline devices. It is difficult to measure the magnetization for the micron-size sample as the volume of the sample is very small. It is observed that the coercive field in the micron-size device is higher compared to the bulk polycrystalline sample [3]. In micron-size devices, the surface-to-volume ratio increases, which enhances the surface anisotropy. This increment in the surface anisotropy results in a large coercive field often found in micron-size devices. [144, 145].

Furthermore, the stability of the antiskyrmion phase is examined by applying an oblique magnetic field with respect to the tetragonal c-axis. The application of an oblique field gives an in-plane field component, which destabilizes the antiskyrmion

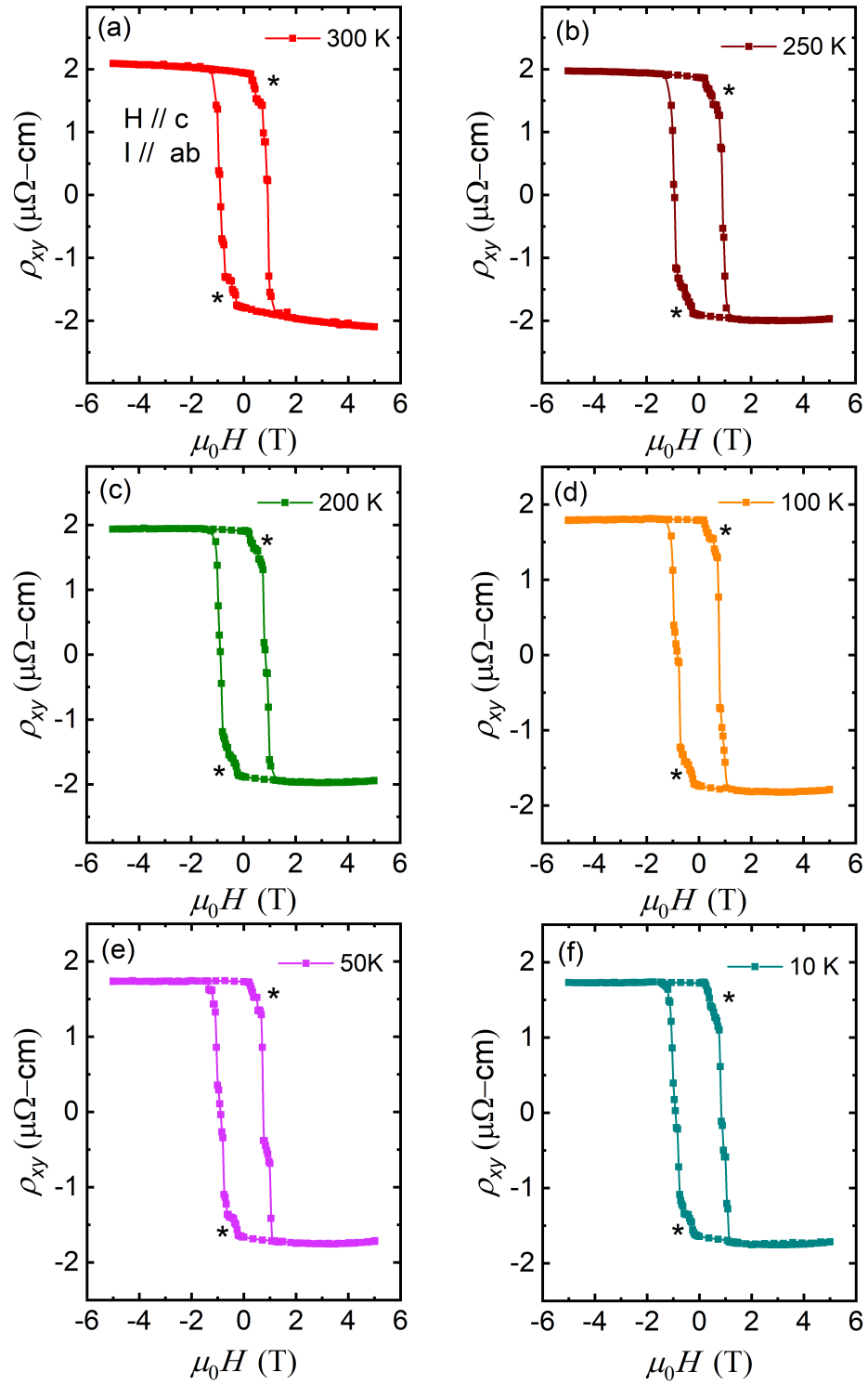


Figure 4.4: (a)-(f) Field variation of Hall resistivity  $[\rho_{xy}(H)]$  for the out-of-plane device at different temperatures. The field is applied along the c-axis ( $H // c$ ), and current is applied along the  $ab$  plane ( $I // ab$ ).

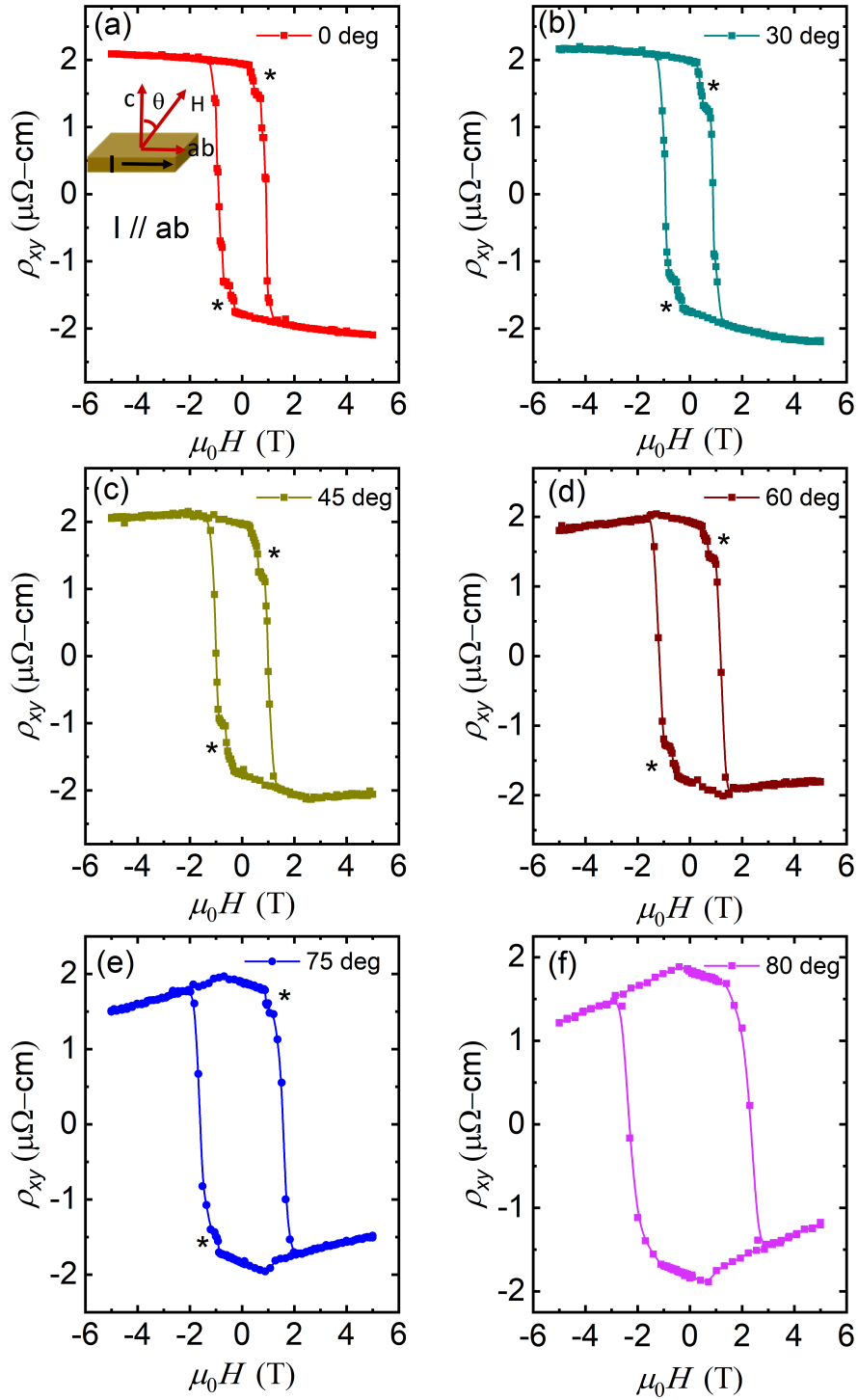


Figure 4.5: (a)-(f) Hall resistivity  $[\rho_{xy}]$  as a function of magnetic field at different tilting angles with respect to the  $c$ -axis. Inset in (a) shows the schematic of the direction of magnetic field with respect to the  $c$ -axis. The current is applied along the  $ab$  plane. The inclination angle  $\theta$  is the angle between the  $c$ -axis and the magnetic field direction.

spin textures. At sufficient in-plane field components, the antiskyrmion phase starts to collapse, resulting in the suppression of the topological Hall signal. For the present study, the oblique magnetic field is applied by rotating the sample from the normal direction using the horizontal rotator probe in the PPMS. Inset of Fig. 4.5 shows the schematic of the measurement configuration. The current is applied along the  $ab$  plane, and the magnetic field is applied at various tilting angles ( $\theta$ ) with respect to the  $c$ -axis. The Hall resistivity  $\rho_{xy}(H)$  as a function of the magnetic field at various tilting angles is shown in Figs. 4.5 (a)-(f). At small tilting angles, clear dip-like anomalies (marked by the stars) are visible. As the inclination angle ( $\theta$ ) increases, the intensity of the dip-like features starts to decrease and disappear at an angle of  $80^\circ$ . At a higher tilting angle ( $75^\circ$ ), the intensity of dip is very feeble and exists in a narrow field range. Remarkably, with increasing the tilting angle, the field range of the antiskyrmion phase decreases, as shown in Fig. 4.6. At a small tilting angle, the antiskyrmion phase is found in a large field range that becomes narrower at a higher tilting angle. The squeezing of the topological Hall effect with increasing the tilting angle demonstrates the annihilation of the antiskyrmion phase in the presence of the in-plane field component.

In principle, the application of a tilting field annihilates the skyrmion/antiskyrmion phase. However, certain theoretical studies [146] demonstrated that in the presence of an in-plane field component, the skyrmions/antiskyrmions do not annihilate instantly; instead, the spin textures are distorted from the circular structure and at a sufficient large tilting field they annihilate. Recent theoretical study [147] highlights the role of anisotropy on the stability of Neel skyrmions and antiskyrmions under an in-plane field. It is shown that the core of the skyrmion/antiskyrmion shifts under the application of an in-plane field. The presence of easy axis anisotropy in  $D_{2d}$  materials provide more stability under an in-plane field. Additionally, recent experimental result on  $\text{Mn}_{1.4}\text{PtSn}$  shows the presence of topological Hall signature due to the antiskyrmion phase at an angle larger than  $70^\circ$  [148]. The existence of the antiskyrmion phase in a large tilted magnetic field for the present system is due to the anisotropic DMI in the presence of uniaxial anisotropy.

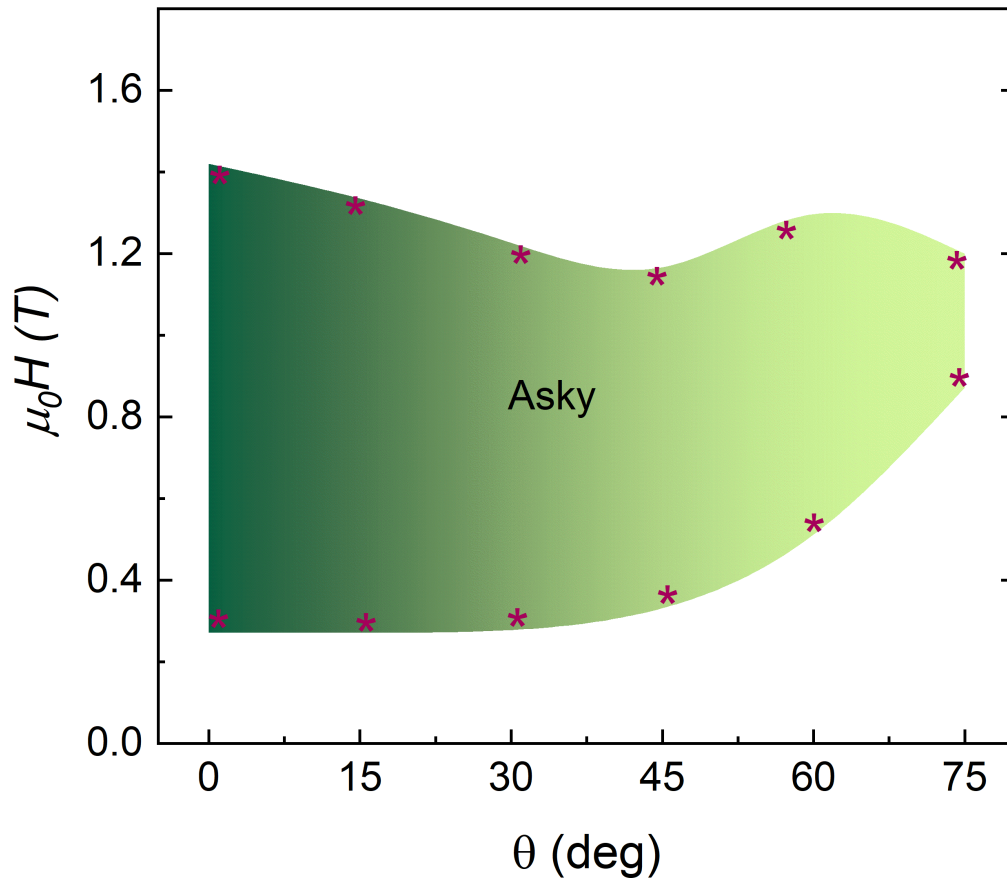


Figure 4.6: Antiskyrmion phase with the variation of tilting angle with respect to the c-axis derived from the Hall resistivity measurements.

## 4.5 Hall resistivity in the in-plane Hall device geometry

The directional dependency of Hall resistivity is measured in the in-plane device geometry. In this case, the current is applied along the c-axis ( $I//c$ ) and the field is applied along the  $ab$  ( $H//ab$ ) plane. Figures 4.7 (a)-(f) show the Hall resistivity  $[\rho_{zy}(H)]$  for the in-plane device at different temperatures. An aberrant hump kind of feature is observed in the Hall resistivity in the whole temperature range. Strikingly, the hump-like feature appears after the magnetization or anomalous Hall voltage reversal field. In the literature, the origin of this type of hump-like feature is assigned to the presence of non-collinear spin textures [149, 150]. However, some recent

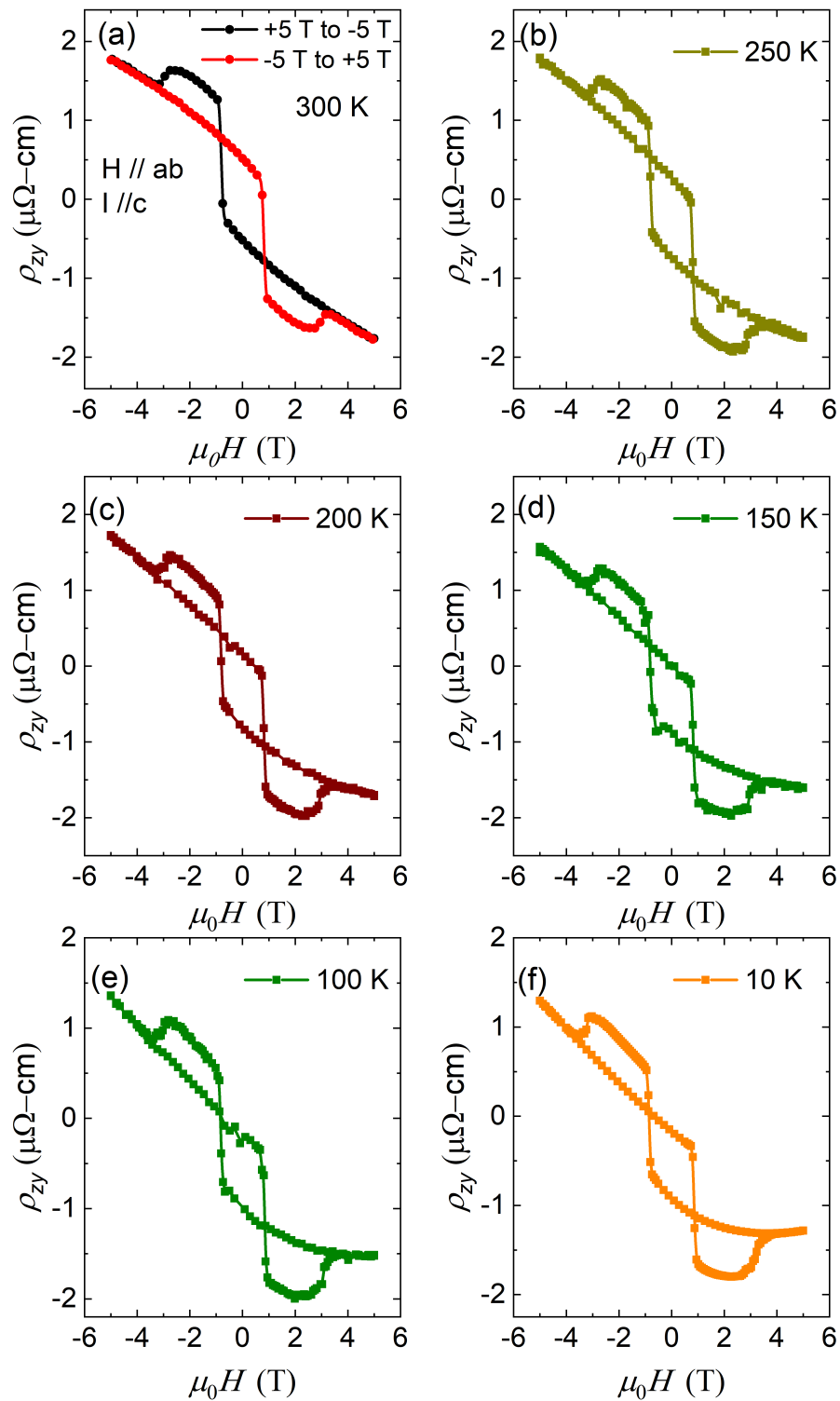


Figure 4.7: (a)-(f) Field variation of Hall resistivity for the in-plane device at different temperatures. The magnetic field is applied along the  $ab$  plane ( $H//ab$ ), and the current is applied along the  $c$ -axis ( $I//c$ ).

studies pointed out that the superposition of two-channel AHE can also give this type of hump-like feature [151, 152, 153, 154, 155]. In all of these studies, the observed hump appears after the magnetization or anomalous Hall reversal. To elucidate the root of this hump-like feature in the present system, minor loop Hall measurements are conducted as depicted in Figure 4.8 (a). The minor loop Hall measurement starts at +5 T and stops at -2 T (red curve), then the field is reversed back to +5 T (green curve). Similarly, Fig. 4.8 (b) shows the minor loop Hall measurement starting at -5 T and sweeping to +2 T (red curve), then reversing back to -5 T (green curve). In both cases, the hump-like feature does not appear in the measured Hall resistivity data. Figure 4.8 (c) shows the minor loop Hall measurement where the measurement starts at +5 T and stops at -3.2 T (red curve), and then sweeps back to +5 T (green curve). This time, the hump-like feature appears on both the sides. The minor loop measurements indicate that the emergence of hump-like feature depends on the field sweeping history. The hump-like feature on the positive field co-ordinate appears once the sweeping field at the negative side (during + 5 T to - 5 T sweeping) is swept beyond the field (i.e., -3.2 T) where the hump-like feature on the negative side completely appears.

In case the hump-like feature originates from the non-collinear spin textures, then it does not depend on the history of field sweeping. During the minor loop measurements, when the sweeping field stops before -3.2 T (during + 5 T to - 5 T sweeping), the second anomalous Hall loop (referred to as AHE 2) remains unswitched. Therefore, it does not contribute to forming the hump-like feature in the Hall resistivity. Once the field goes beyond -3.2 T, the AHE 2 switches and the hump-like feature appears. Hence, the minor loop measurements show that the hump-like feature originates from the superposition of two-component anomalous Hall loops.

The two-component anomalous Hall loop has been separated using the procedure used by Tai *et al.* [155]. Figure 4.9 (a) illustrates the decomposition procedure of two anomalous Hall loops. The red solid line (dark yellow solid line) is the Hall measurements from +5 T to -5 T (-5 T to +5 T). The solid blue line is the minor

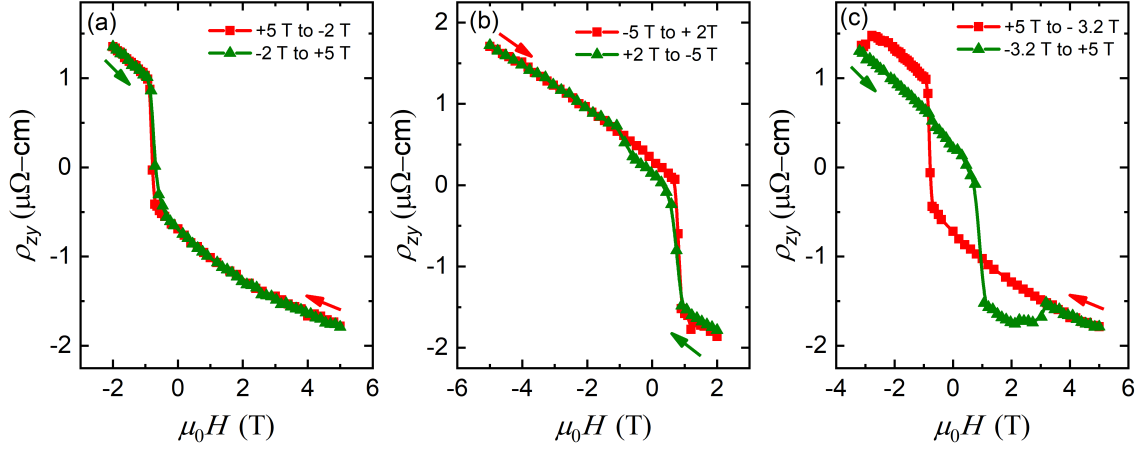


Figure 4.8: Room temperature minor loop Hall resistivity  $[\rho_{zy}]$  measurements. (a) Measurement started at +5 T and stopped at -2 T (red curve), then came back to +5 T (green curve). (b) Measurement started at -5 T and stopped at +2 T (red curve), then came back to -5 T (green curve). (c) Measurement started at +5 T and stopped at -3.2 T (red curve), then came back to +5 T (green curve). Arrows depict the direction of the field sweep.

loop Hall resistivity starts at +5 T and stopped at -2 T. The dashed dark yellow line represents the shifted Hall resistivity data measured from -5 T to +5 T. The data is shifted vertically in such a way that it aligns with the hump on the negative side and lies with the minor loop. As the minor loop stopping at -2 T does not switch the AHE 2, it contains only the AHE 1 loop. The data for the AHE 1 is taken from +5 T to some  $-ve$  field (marked by blue up arrow), and the remaining data (i.e.,  $-ve$  to -5 T) is taken from the shifted curve (marked by dark yellow down arrow). This gives one loop (i.e., +5 T to -5 T) of AHE 1. The second loop (i.e., -5 T to +5 T) is obtained using the same method. This time, the +5 T to -5 T data is shifted, and the minor loop starting from -5 T and stopping at +2 T is used. In this way, the complete loop of AHE 1 is acquired. The AHE 2 loop is extracted by subtracting the AHE 1 loop from the measured full anomalous Hall loop. Figure 4.9 (b) shows the extracted two anomalous Hall loops that exhibit different coercivity and opposite signs.

Furthermore, the Hall resistivity  $[\rho_{zy}(H)]$  for the in-plane device with an applied tilted magnetic field with respect to the  $ab$  plane is measured for various inclination angles. Figures 4.10 (a)-(f) show the room temperature Hall resistivity  $[\rho_{zy}(H)]$

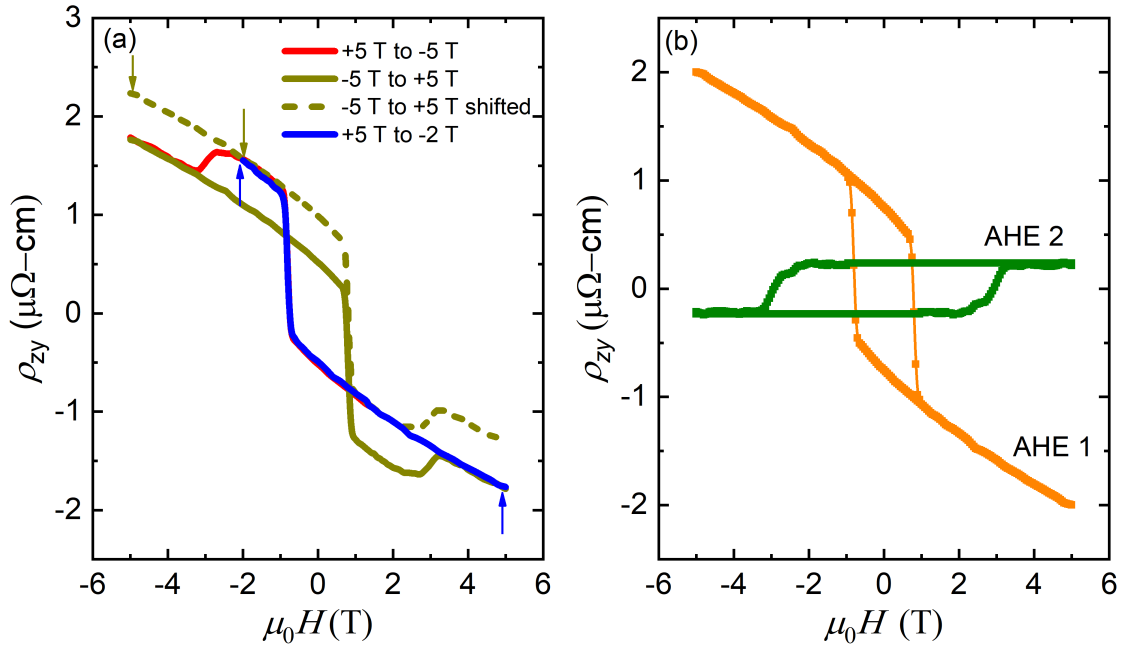


Figure 4.9: (a) Decomposition procedure of two anomalous Hall loops. Red (solid dark yellow) curve is the Hall resistivity data measured from +5 T to -5 T (-5 T to +5 T). Dashed dark yellow line is the shifted data of the solid dark yellow curve. Blue curve is the minor loop measurements with +5 T to -2 T. (b) Decomposed two anomalous Hall loops.

data for the in-plane device at different oblique fields. Different inclination angles are obtained by rotating the field from the  $ab$  plane to the  $c$ -axis. The schematic of the measurement is shown in the inset of Fig. 4.10 (a). With increasing the tilting angle away from the  $ab$  plane, the intensity of the hump-like feature starts to decrease and vanishes at an angle of  $35^\circ$ . The anomalous Hall switching field changes sign with tilting more than  $15^\circ$  as compared to the  $0^\circ$  tilting case. At a higher tilting angle of  $80^\circ$  (i.e., field towards the  $c$ -axis), no anomaly in the anomalous Hall loop is observed [Fig. 4.10 (f)]. At this tilting angle of the in-plane device, the resistivity  $[\rho_{zy}(H)]$  exhibits similar anomalous switching and coercive field with that of the out-of-plane device [i.e.,  $\rho_{xy}(H)$ ] at  $0^\circ$  tilting angle. This observation suggests that as the magnetic field rotates towards the easy axis (i.e.,  $c$ -axis) an out-of-plane component of the field arises. At angles  $45^\circ$  and  $60^\circ$ , both out-of-plane and in-plane components exist, resulting in the anomalous Hall switching field being negative. It is to be noted that during the tilting, the magnetic field is rotated from the  $ab$

plane to the  $c$ -axis (in-plane device) or from the  $c$ -axis to the  $ab$  plane (out-of-plane device), but the current direction is different in these two Hall geometry. For the out-of-plane device, the current direction is always along the  $ab$  plane, and for the in-plane device, the current direction remains along the  $c$ -axis during the tilting. Therefore, it is expected that the Hall resistivity  $\rho_{xy}(H)$  at  $0^\circ$  and  $\rho_{zy}(H)$  at  $80^\circ$  do not match exactly, although the field direction becomes the same.

The two-component anomalous Hall loops reported in the earlier studies mostly belong to the thin film systems, where the compositional inhomogeneities at the interface and defects in the film are the primary sources of the two anomalous Hall loops. In the present study, since the single crystalline Hall devices are being fabricated from a well-characterized polycrystalline sample, no such compositional inhomogeneity or defects are expected [3]. In addition, the results are reproduced using several devices prepared from the other parts of the sample. In the present case, the origin of the two-component anomalous Hall loops is understood using the microstructural study.

Figure 4.11 (a) shows the TEM image of the in-plane oriented lamella. In this orientation nano-twin crystal structures are detected (shown by the arrow) throughout the sample. The presence of the twin structure is also observed in the SAED patterns [double spot in Fig. 4.2 (f)]. In comparison, no such kind of twin microstructure is spotted in the case of the out-of-plane oriented lamella [Fig. 4.11 (b)].

Generally, in the presence of twin crystal structures, the magnetic moments reorient themselves in such a way that in the adjacent twin variants, they form  $90^\circ$  magnetic domains, while in a single variant  $180^\circ$  domain form, as shown in Fig. 4.11 (c) [117, 119, 156, 157, 158]. When a magnetic field is applied, these  $90^\circ$  magnetic domains in the twin variants experience different components of magnetic fields, which lead to the observed two-component anomalous Hall signals. Once the field is applied along the easy axis (as in the case of tilting towards the  $c$ -axis), the magnetic moments start to rotate along the  $c$ -axis. At a large out-of-plane field component (i.e., large tilting angle) all the magnetic moments align along the  $c$ -axis

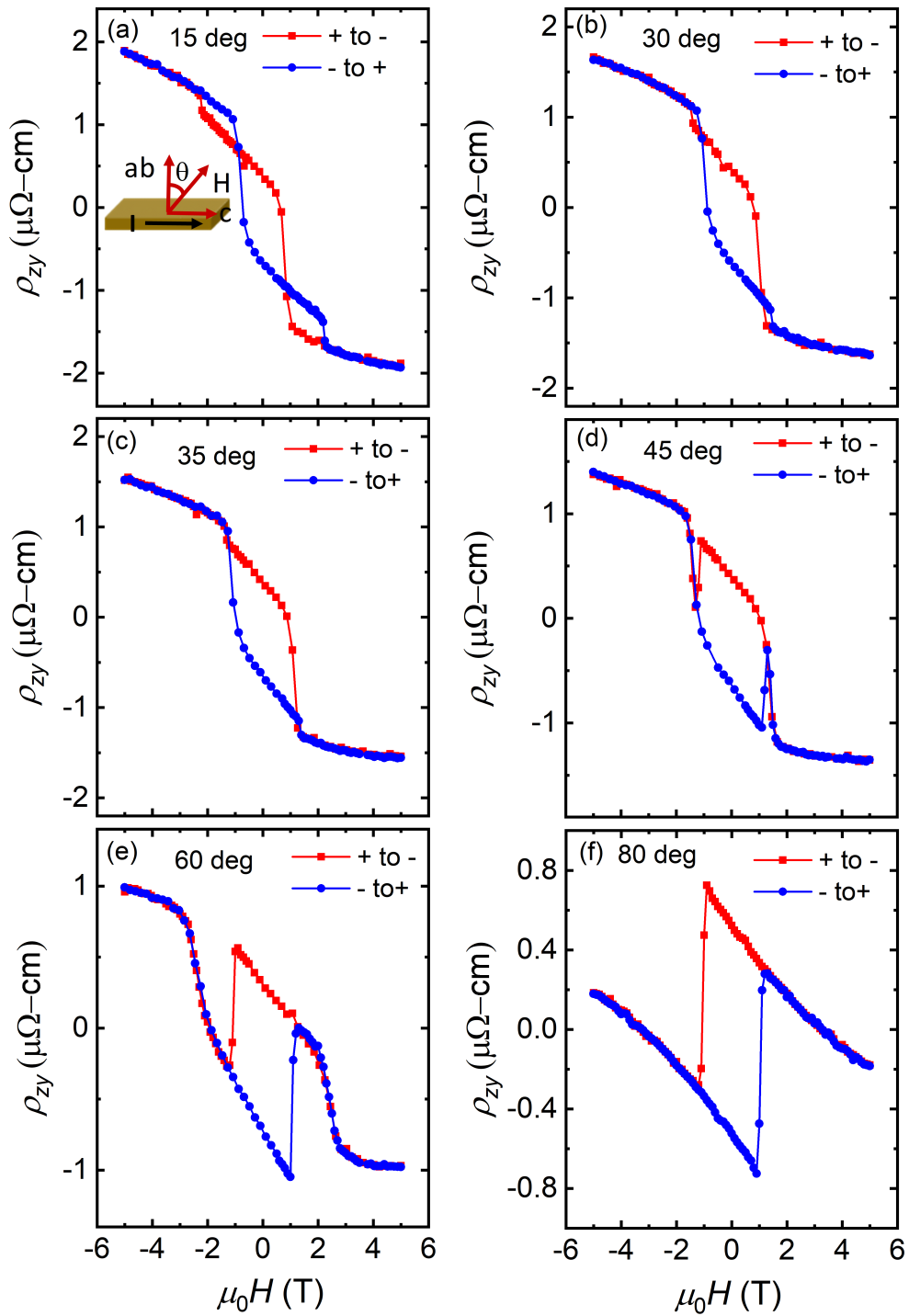


Figure 4.10: (a)-(f) Hall resistivity [ $\rho_{zy}$ ] for the in-plane device with the variation of tilted magnetic field. Inset of (a) shows the schematic of the measurement configuration. The current is applied along the  $c$ -axis. The inclination angle  $\theta$  is the angle between the  $ab$  plane and the applied magnetic field.

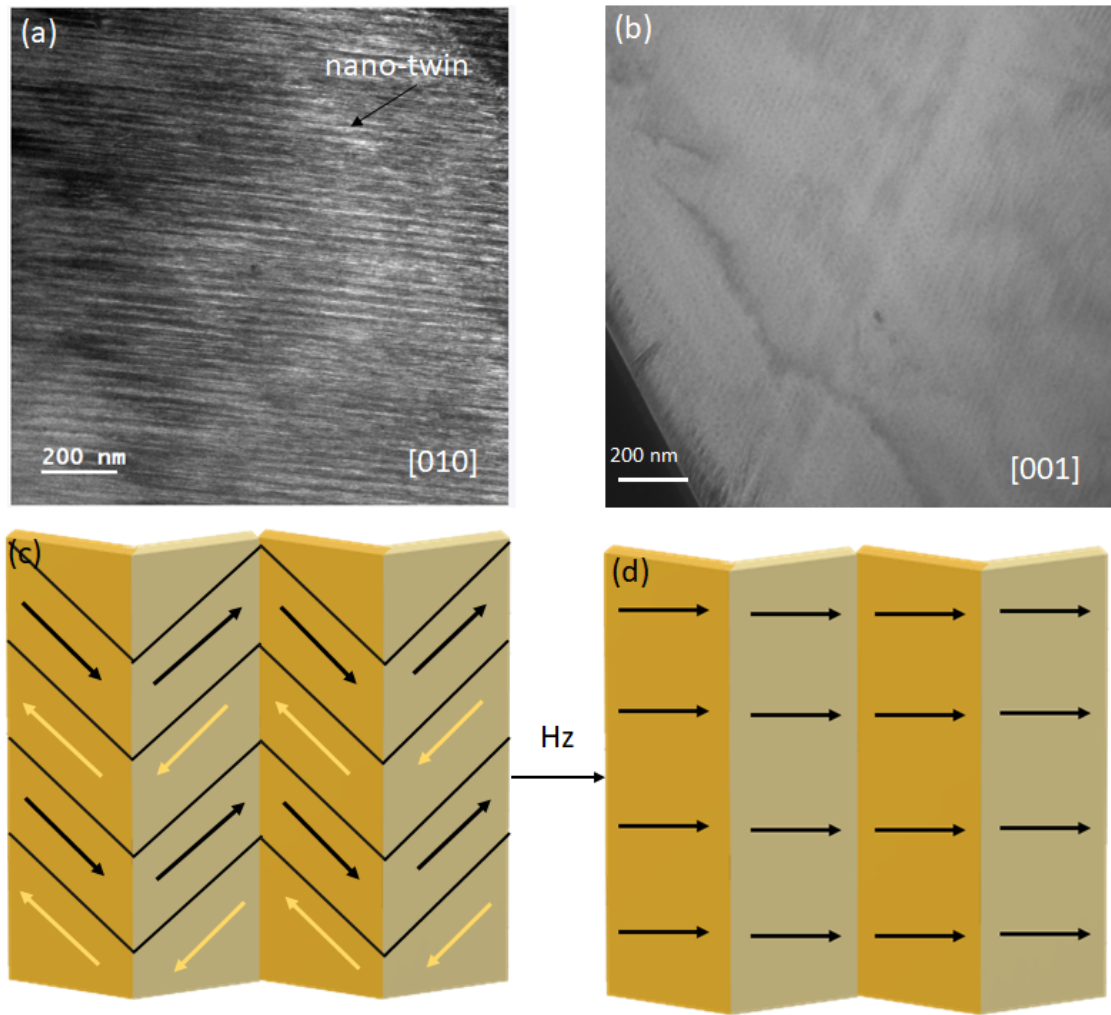


Figure 4.11: Microstructural analysis. (a) Microstructure of in-plane oriented lamella taken using TEM. The black arrow shows the nano-twin bundles. (b) TEM image of the out-of-plane oriented lamella. (c) Schematic of twin domains. Yellow and dark yellow regions represent the twin crystal domains. Black and Yellow arrows represent the magnetic moment. The magnetic moments form  $90^\circ$  domains in the adjacent twin variants and  $180^\circ$  domains in a single variant. (d) Effect on the magnetic moment by applying out-of-plane field component ( $H_z$ ). At large out-of-plane field only single magnetic domain forms.

to form a single domain, as illustrated in the schematic Fig. 4.11 (d). This results in a single anomalous Hall loop as observed in the case of  $80^\circ$  tilting case [Fig. 4.10 (f)]. The minor loop measurements and the microstructural analysis establish that the hump-like feature appears due to the superposition of two anomalous Hall loops, originating from the presence of twin crystal structures in the in-plane direction.

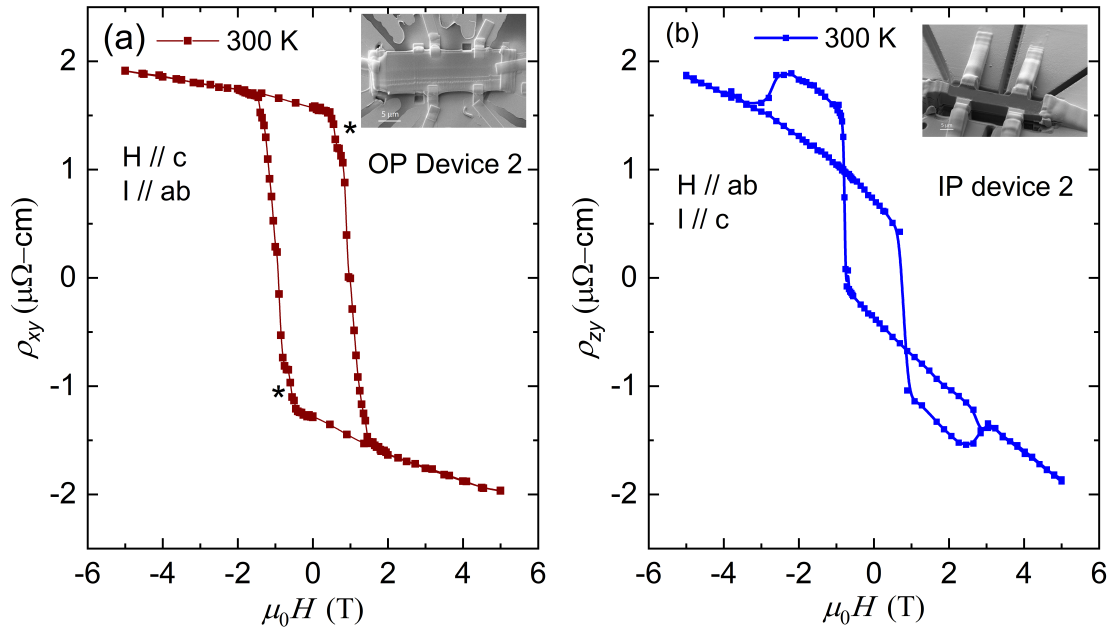


Figure 4.12: Field variation of Hall resistivity for the (a) out-of-plane  $[\rho_{xy}]$  and (b) in-plane  $[\rho_{zy}]$  device. Insets show the corresponding devices fabricated from a different region.

## 4.6 Reproducibility of the experimental results

The reproducibility of the observed anomalous Hall signals is confirmed by measuring the Hall resistivity for both out-of-plane and in-plane orientations in Hall devices fabricated from a single grain of different parts of the polycrystalline sample. Figures 4.12 (a)-(b) show the Hall resistivity  $[\rho_{xy}]$  and  $[\rho_{zy}]$  for the out-of-plane and in-plane devices, respectively, prepared from a different part of the sample. As expected, in case of the out-of-plane device, a clear dip-like feature, and an aberrant hump is observed for the in-plane device.

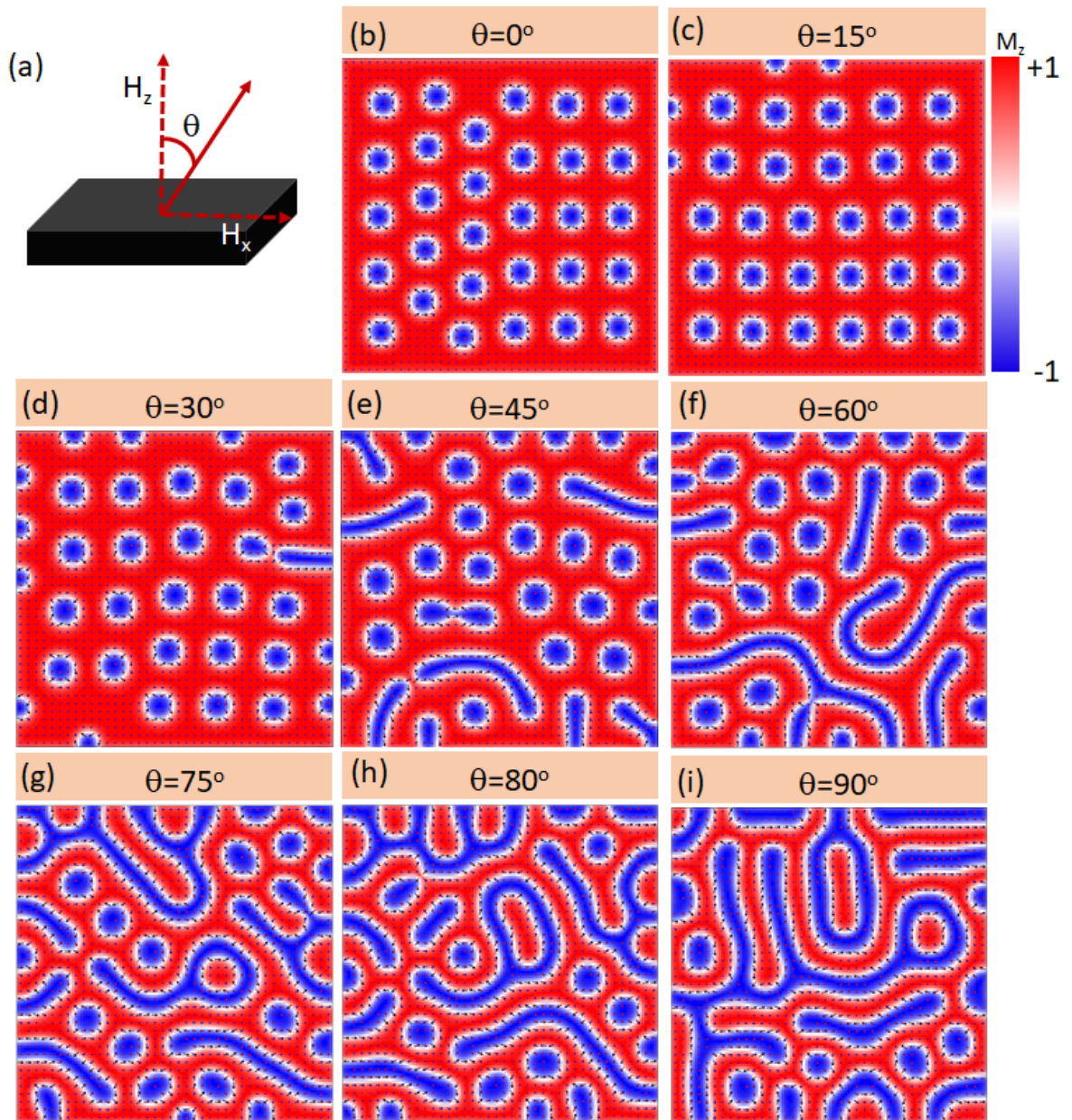


Figure 4.13: Micromagnetic simulations. (a) Schematic of field configuration in the presence of an inclined magnetic field.  $\theta$  denotes the angle between the magnetic field and the normal direction.  $H_z$  and  $H_x$  are the out-of-plane and in-plane field components, respectively. (b)-(i) Spin textures from the micromagnetic simulation results under the application of different tilted magnetic fields. The angle of inclination is mentioned in the figure. The color bar shows the out-of-plane magnetization.

## 4.7 Micromagnetic simulations

Micromagnetic simulations are performed to understand the mechanism of anti-skyrmion formation in the present system. The simulations are conducted by using Object-Oriented MicroMagnetic Framework (OOMMF) [159] code by taking the Heisenberg exchange, the DM interaction for the D2d symmetry, uniaxial magnetic anisotropy, dipole-dipole interaction and Zeeman energy terms. The slab geometry taken for the simulation is  $600 \text{ nm} \times 600 \text{ nm} \times 50 \text{ nm}$  and the mesh size is  $5 \text{ nm} \times 5 \text{ nm} \times 5 \text{ nm}$ . The simulation parameters are taken from the experimental result [3]. These parameters are exchange stiffness constant  $A = 3 \times 10^{-11} \text{ J m}^{-1}$ , DMI constant  $D = 5.5 \text{ m J m}^{-2}$ , uniaxial anisotropy constant  $K = 4.5 \times 10^5 \text{ J m}^{-3}$ , and the saturation magnetization  $M_s = 1.65 \times 10^5 \text{ A m}^{-2}$ . The simulations are carried out with a tilted magnetic field from the normal direction. For a tilted magnetic field  $H_0$  with an inclination angle  $\theta$  with respect to the normal direction, the out-of-plane field component will be  $H_z = H_0 \cos\theta$  and the in-plane field component will be  $H_x = H_0 \sin\theta$ . Simulations are performed considering both the out-of-plane and in-plane field components at different tilting angles with an applied field  $H_0 = 0.5 \text{ T}$ . Figure 4.13 (a) shows the schematic of field configuration, where  $H_z$  represents the out-of-plane field component and  $H_x$  is the in-plane field component. Figures 4.13 (b)- (i) display the magnetic spin structures obtained from the simulation under different applied tilting fields. At small tilting angles large no of antiskyrmions are stabilized, and the antiskyrmion density remains the same up to the tilting angle  $30^\circ$ . As the tilting angle increases, the antiskyrmions start to transform into a non-topological strip domains and the density of antiskyrmions decreases. At large tilting angles [Figs. 4.13 (h) -(i)], the non-topological strip domains are predominantly present. The present simulation results support the experimental observation of decreasing the topological Hall effect with increasing the tilted magnetic field. With increasing the tilting angle, the antiskyrmion density decreases, which in turn decreases the topological Hall signal. Interestingly, at large tilting angles, some distorted antiskyrmions coexist with the stripe domains, resulting in

a subtle topological Hall signature. The presence of these distorted antiskyrmions demonstrates the robustness of these objects in an anisotropic DMI environment.

## 4.8 Summary

The robustness of magnetic antiskyrmions under a tilted magnetic field with respect to the tetragonal  $c$ -axis in  $D_{2d}$  Mn-Ni-Ga system is demonstrated in the present chapter. The observation of the topological Hall effect for the out-of-plane device configuration fabricated from a single crystalline grain confirms the presence of antiskyrmion in this system. The topological Hall effect decreases as the magnetic field direction deviates from the  $c$ -axis and vanishes above  $75^\circ$ . The experimental findings are in line with the micromagnetic simulation outcomes, where it is found that with the application of an in-plane field component, the antiskyrmion density decreases, and non-topological stripe domains appear. The survival of the antiskyrmion phase against a large in-plane field demonstrates the robustness of the anisotropic DMI present in  $D_{2d}$  materials. In the in-plane device geometry, an aberrant hump kind of feature is observed in the Hall resistivity. A detailed study of minor loop Hall measurements confirms that the hump kind of feature emerges due to the superposition of two-channel anomalous Hall effect. The TEM microstructure analysis confirms the existence of a twin crystal structure in the in-plane orientation, which results in the observed two component anomalous Hall signals. The present study sheds light on the stability of the antiskyrmion phase and the presence of non-topological features in this system.



# Chapter 5

## Transition from Extrinsic to Intrinsic Mechanism of Anomalous Hall Effect in Mn-Pt(Ir)Sn Heusler alloy

The previous two chapters demonstrate the characterization of topologically non-trivial antiskyrmion state in the  $D_{2d}$  symmetric Heusler materials. The non-trivial magnetic objects are promising candidates for the development of future generation spintronics devices. In recent studies, it is found that the formation of topologically non-trivial spin textures bring about a subtle modification of the electronic band structure in the system [160, 161, 162, 163]. Any change in the band structure of a magnetic system can be electrically interpreted by the measurement of anomalous Hall effect (AHE). Nevertheless, it is also expected that any modification of the electronic band structure should alter the real-space spin texture of the system. Therefore, it is extremely important to play between the real-space spin textures and the momentum space band structure for the advancement of spintronics technology. In this context, along with the magnetic skyrmions/antiskyrmions,

the anomalous Hall effect has its own role in the spintronics devices, such as Hall sensors, etc. Beyond this, the AHE has the capability to generate dissipation-less transverse currents and can induce spin transfer torque, which can derive the magnetic antiskyrmion [34, 35]. Therefore, the tuning of anomalous Hall effect and understanding the underlying mechanisms hold utmost importance. This chapter is devoted to the understanding of the microscopic origin of AHE and its tunability by tuning the involved mechanisms.

The physical origin of the anomalous Hall effect has been the most intriguing concept that has remained controversial for a long time. The ordinary Hall effect arises due to the Lorentz force experienced by the conduction electrons, while the anomalous Hall voltage is related to the time-reversal symmetry breaking in the system. Current understanding of AHE suggests that mainly two types of mechanisms are responsible for the AHE. The first one is the intrinsic mechanism related to the band structure of the system, and the second one is the scattering-dependent extrinsic mechanism. The extrinsic mechanism depends on two types of scattering process, (i) skew scattering and (ii) side-jump. In recent times, large AHE has been observed in several materials, including antiferromagnetic systems. Some of these materials exhibit an intrinsic mechanism dominated AHE, while others display dependency on extrinsic ones. A comprehensive study on the manipulation of different mechanisms of AHE is essential for its practical applications. On this subject, the present chapter focuses on the tuning of AHE and its manipulation via tailoring different mechanisms in  $\text{MnPt}_{1-x}\text{Ir}_x\text{Sn}$  Heusler system. A series of polycrystalline samples are synthesized using the arc melting furnace. The structural characterizations are carried out using XRD, SEM, and Neutron diffraction (ND) experiments. A comprehensive magnetic and electronic transport measurements are performed to understand the dependency of AHE on the magnetic state of the present system. A thorough analysis of the AHE using scaling relation and power law fitting is carried out to extract different contributions from the extrinsic and intrinsic mechanisms.

## 5.1 Sample preparation

Polycrystalline samples of  $\text{MnPt}_{1-x}\text{Ir}_x\text{Sn}$  (with  $x = 0, 0.1, 0.2, 0.3, 0.5$ ) are prepared using the arc melting furnace in an argon atmosphere. Due to the high melting point of Ir, a much higher current is needed during the melting process that leads to the evaporation of the Mn. In order to address this issue, at first Ir and Pt elements are melted together. The mixed Ir and Pt ingots are then broken into small pieces and melted with Mn and Sn. The ingots are melted three-to-four times for proper mixing. The prepared ingots are annealed in a vacuum quartz tube at  $850^\circ\text{C}$  for one week and subsequently quenched in an ice-water mixture.

## 5.2 Characterizations

### 5.2.1 Structural and compositional characterization

The phase purity and compositional homogeneity of the samples are confirmed using XRD and SEM. Figures 5.1 (a) - (e) show the room temperature Rietveld refinement of XRD patterns for  $\text{MnPt}_{1-x}\text{Ir}_x\text{Sn}$  with  $x = 0, 0.1, 0.2, 0.3, 0.5$ . All the samples are found to be in a single phase, stabilizing in a cubic Heusler crystal structure with space group  $F\bar{4}3m$  (No. 216). The Wyckoff positions of Mn, Pt(Ir), and Sn atoms are 4b  $(\frac{1}{2}, \frac{1}{2}, \frac{1}{2})$ , 4c  $(\frac{1}{4}, \frac{1}{4}, \frac{1}{4})$  and 4a  $(0, 0, 0)$ , respectively. For  $x = 0.5$  the Rietveld refinement is performed with 10% atomic disorder between Mn/Ir atoms, as discussed in detail in the Neutron diffraction section. The refined lattice constants are found to be  $6.25\text{ \AA}$  for  $\text{MnPtSn}$  and  $6.23\text{ \AA}$  for  $\text{MnPt}_{0.5}\text{Ir}_{0.5}\text{Sn}$ . Figures 5.2 (a)-(e) show the SEM images for all the samples. The homogeneous contrast of all the samples confirm the single-phase nature of the samples. The initial stoichiometry ratios of the samples and that found from the EDS measurements match very well, as shown in Table 5.1.

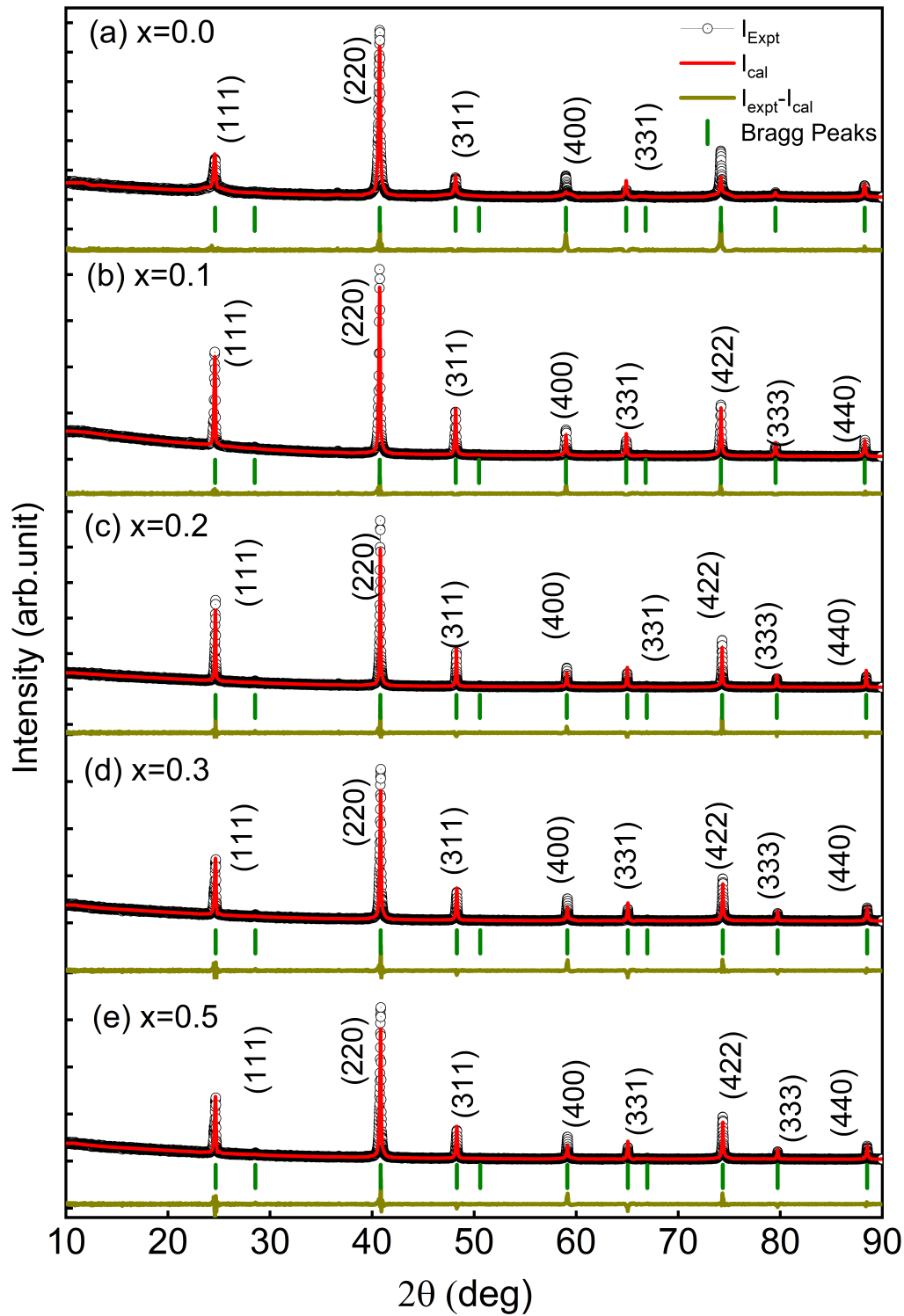


Figure 5.1: Rietveld refinement of room temperature powder XRD patterns for MnPt<sub>1-x</sub>Ir<sub>x</sub>Sn with x=0, 0.1, 0.2, 0.3, 0.5.

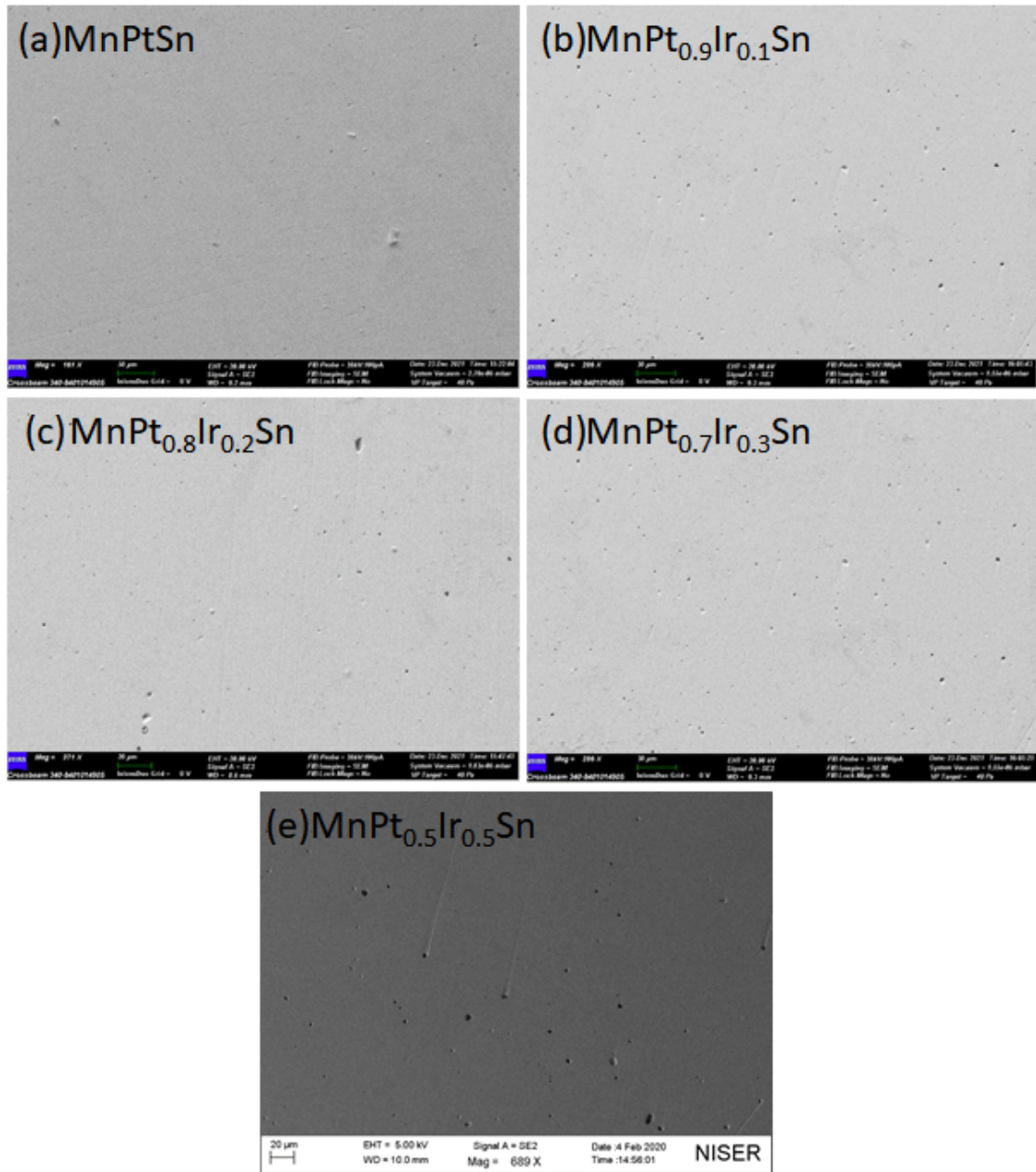


Figure 5.2: (a)-(e) Scanning electron microscopy images of MnPt<sub>1-x</sub>Ir<sub>x</sub>Sn, with x=0, 0.1, 0.2, 0.3, 0.5.

### 5.2.2 Magnetic studies

The zero field-cooled (ZFC, black open symbols) and field-cooled (FC, red closed symbols) temperature dependence of magnetization curves for all the samples are depicted in the Figures 5.3 (a) - (e). The Curie temperature ( $T_C$ ) of the samples decreases with increasing the Ir concentration, as shown in Fig. 5.3 (f). The  $T_C$  of

Table 5.1: Atomic ratios obtained from the EDS measurements

Sample	Initial atomic ratios (%)	Obtained atomic ratios (%)
MnPtSn	Mn- 33.3, Pt- 33.3, Sn- 33.3	Mn- 35.5, Pt-31.7, Sn-32.8
MnPt <sub>0.9</sub> Ir <sub>0.1</sub> Sn	Mn- 33.3, Pt-30, Ir- 3.3, Sn- 33.3	Mn- 35.9, Pt-28.7, Ir- 3.1, Sn-32.3
MnPt <sub>0.8</sub> Ir <sub>0.2</sub> Sn	Mn- 33.3, Pt-26.6, Ir- 6.7, Sn-33.3	Mn- 35.6, Pt-24.4, Ir- 6.1, Sn-33.9
MnPt <sub>0.7</sub> Ir <sub>0.3</sub> Sn	Mn- 33.3, Pt-23.3, Ir- 10, Sn-33.3	Mn- 35.2, Pt-22.8, Ir- 9.3, Sn-32.7
MnPt <sub>0.5</sub> Ir <sub>0.5</sub> Sn	Mn- 33.3, Pt-16.65, Ir- 16.65, Sn-33.3	Mn- 35.9, Pt-15.9, Ir- 15.1, Sn-33.1

MnPtSn and MnPt<sub>0.5</sub>Ir<sub>0.5</sub>Sn are 326 K and 226 K, respectively. The field variation of magnetization [ $M(H)$ ] measured at 5 K for different Ir doped samples are shown in Figures 5.4 (a) - (e). The change in the saturation magnetization ( $M_S$ ) with Ir concentration is shown in Fig. 5.4 (f). The  $M_S$  systematically decreases with increasing the Ir percentage. In the case of Cubic Heusler alloys, the total magnetic moment greatly depends on the number of valence electrons in the system. Since Ir has less valence electrons than that of Pt, the magnetization decreases with Ir doping.

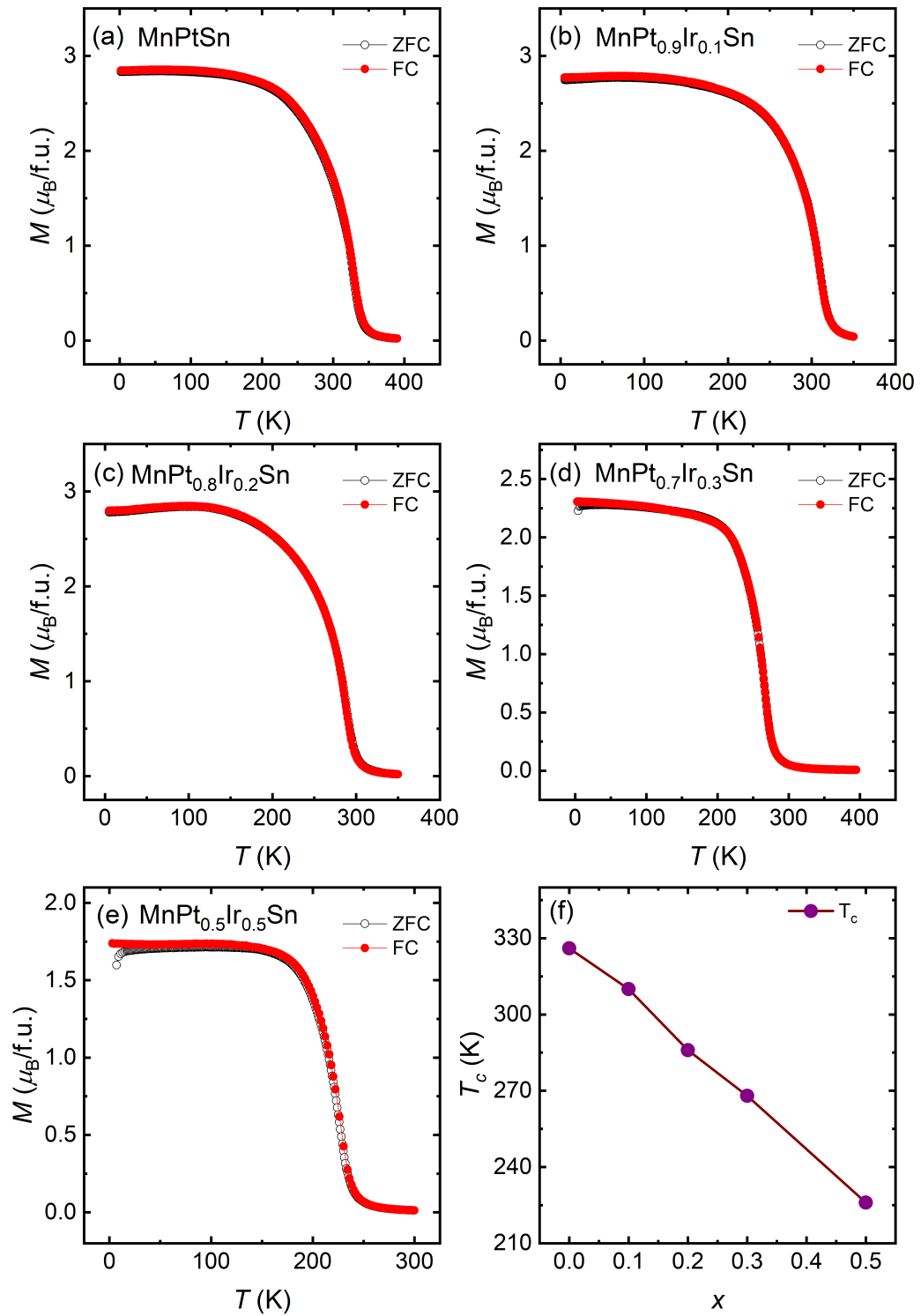


Figure 5.3: Temperature variation of zero field-cooled (ZFC) and field-cooled (FC) magnetization curve for  $\text{MnPt}_{1-x}\text{Ir}_x\text{Sn}$ , with  $x = 0, 0.1, 0.2, 0.3, 0.5$ . The applied field is 1 KOe. (f) Plot of Curie temperature ( $T_C$ ) with Ir concentration.

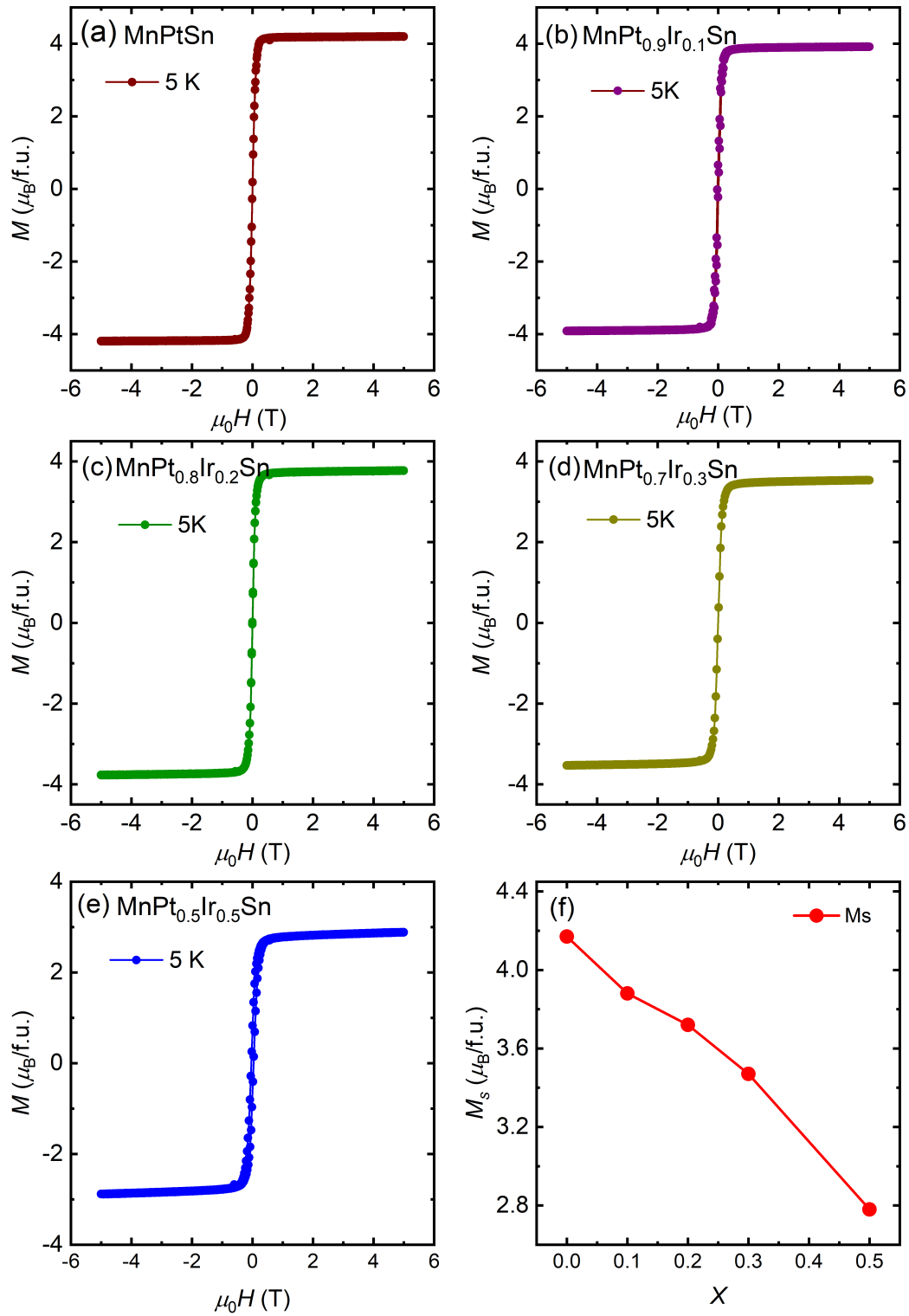


Figure 5.4: Magnetic hysteresis loops measured at 5 K for  $\text{MnPt}_{1-x}\text{Ir}_x\text{Sn}$ , with  $x=0, 0.1, 0.2, 0.3, 0.5$ . (f) Variation of saturation magnetization ( $M_s$ ) with Ir concentration.

### 5.2.3 Neutron diffraction study

To examine the effect of Ir doping on the structural and magnetic state, powder neutron diffraction (ND) measurements are carried out for MnPtSn and MnPt<sub>0.5</sub>Ir<sub>0.5</sub>Sn at different temperatures. For MnPt<sub>0.5</sub>Ir<sub>0.5</sub>Sn, the neutron diffraction data are collected at 2 K and 300 K. In the first place, 300 K data is used to find the nuclear/structural parameters. Rietveld refinement of the 300 K ND data is conducted using the FullProf Suite [164] with the Wyckoff positions Mn at 4b ( $\frac{1}{2}, \frac{1}{2}, \frac{1}{2}$ ), Pt/Ir at 4c ( $\frac{1}{4}, \frac{1}{4}, \frac{1}{4}$ ) and Sn at 4a (0, 0, 0). The simulated intensity produced using these Wyckoff positions do not match well with the experimental data, as illustrated in Fig. 5.5 (a). In Heusler alloy, the atomic disorder between different atomic positions is often observed [101, 113, 165]. The most electropositive element Mn, prefers to sit along with the most electronegative element Sn. The Ir is more electropositive than the Pt. Hence there is a possibility that Ir can go to the Mn site, and the same amount of Mn can occupy the Ir site. To account for any atomic disorder that exists in the sample, Rietveld refinements are conducted using varying degrees of atomic disorders between the Mn and Ir sites. Figures 5.5 (b)-(e) show the Rietveld refinement with atomic disorder 5%, 10%, 15% and 20%, respectively. It is found that the best fitting is possible with 10% atomic disorder. The obtained fitting parameters from the refinement results for different atomic disorders are listed in Table 5.2. The fitting parameters  $\chi^2$  and  $R_{Bragg}$  factors are minimum for 10% disorder, while these parameters increase with increasing or decreasing the disorder percentage. Hence, the Rietveld refinements of the ND data confirms that with the substitution of Ir induces atomic disorder in the system, which is about 10% for MnPt<sub>0.5</sub>Ir<sub>0.5</sub>Sn. The crystal structure of MnPtSn and MnPt<sub>0.5</sub>Ir<sub>0.5</sub>Sn are shown in Fig. 5.6.

The low-temperature powder Neutron diffraction data are used to investigate the magnetic state of the samples. Since the  $T_C$  of MnPtSn is above 300 K, it is not possible to collect ND data above 300 K for this sample. Thus, for this sample, the regular arrangement of the atomic positions is used for the Rietveld refinement [structure is shown in Fig. 5.6 (a)]. The Rietveld refinement of ND data collected

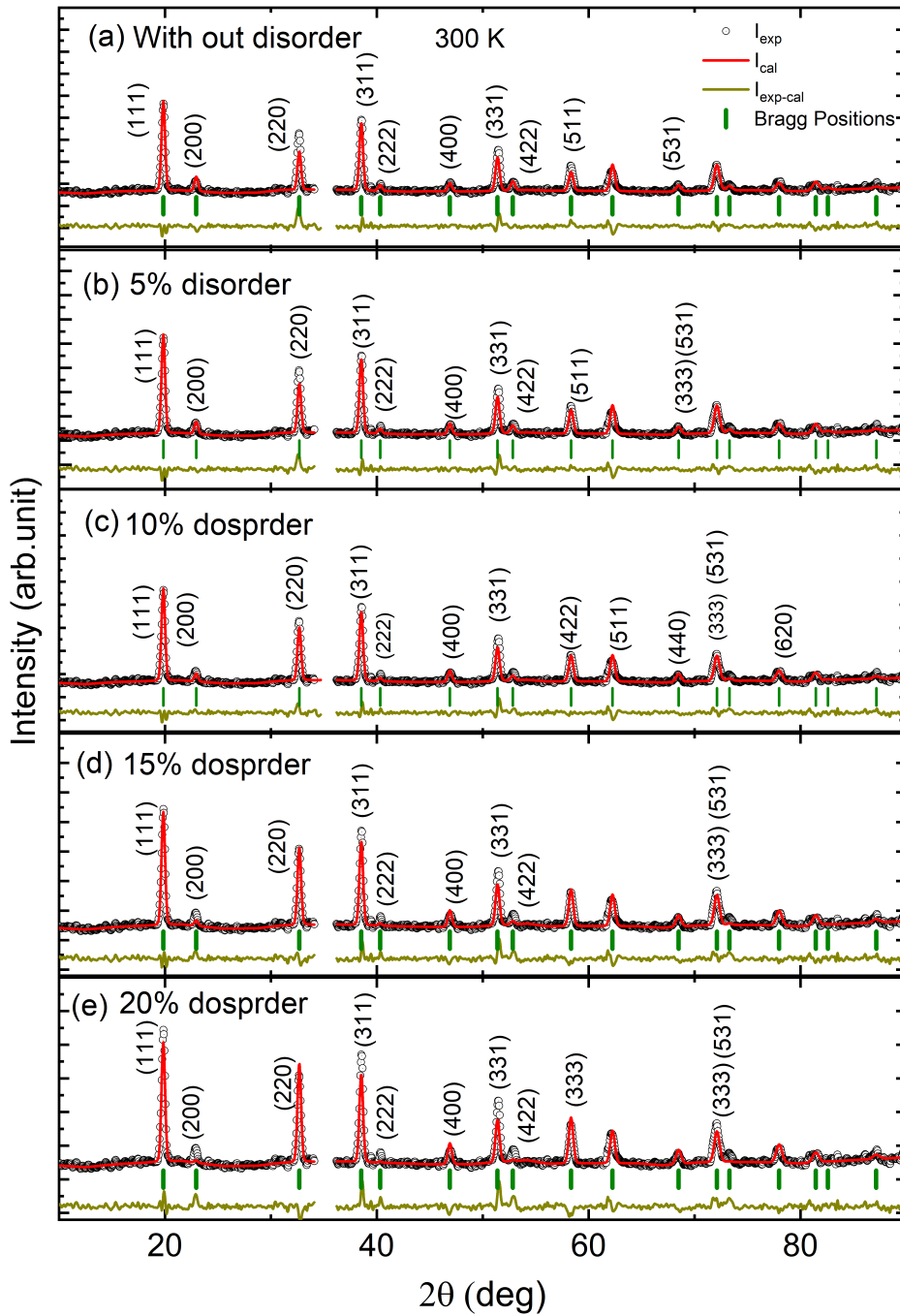


Figure 5.5: Structural Rietveld refinement of powder neutron diffraction data for  $\text{MnPt}_{0.5}\text{Ir}_{0.5}\text{Sn}$  recorded at 300 K with different atomic disorders between Mn/Ir atom. (a)-(e) Rietveld refinement of powder ND pattern with 0 %, 5 %, 10 %, 15 % and 20 % atomic disorder, respectively. The region between  $34^\circ$  to  $36^\circ$ , is clipped due to contributions from the cryostat.

at 2 K for  $\text{MnPtSn}$  and  $\text{MnPt}_{0.5}\text{Ir}_{0.5}\text{Sn}$  are shown in Figs. 5.7 (a)-(b), respectively.

The refined magnetic moment for  $\text{MnPtSn}$  is found to be  $3.52 \mu_B/f.u.$  In the case

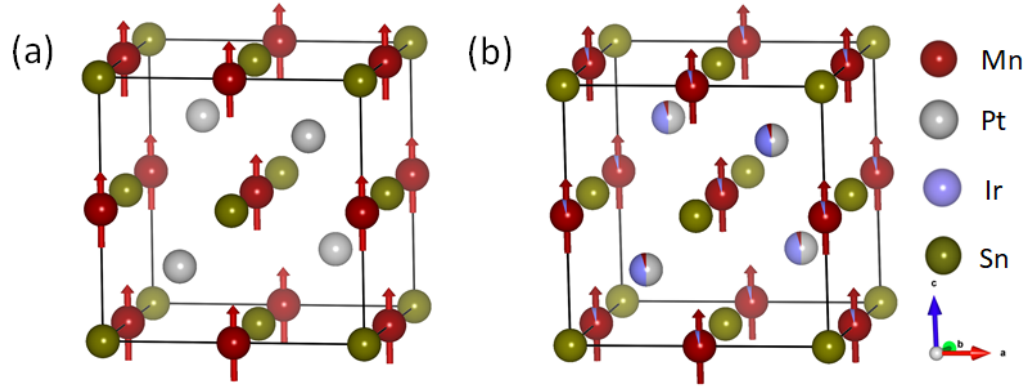


Figure 5.6: (a) Crystal structure of MnPtSn. (b) Crystal structure of MnPt<sub>0.5</sub>Ir<sub>0.5</sub>Sn with 10 % atomic disorder between Mn/Ir atoms.

Table 5.2: Site occupancies and Rietveld refinement parameters for different atomic disorder between Mn/Ir atoms for MnPt<sub>0.5</sub>Ir<sub>0.5</sub>Sn.

Atomic Disorder	Wyckoff Position	Site Occupancy (%)	$\chi^2$	$R_{Bragg}$
0.0 % Disorder	4b	100 Mn + 0 Ir	6.4	13.71
	4c	50 Pt + 50 Ir		
5% Disorder	4b	95 Mn + 5 Ir	5.96	12.06
	4c	50 Pt + 45 Ir + 5 Mn		
10% Disorder	4b	90 Mn + 10 Ir	5.96	11.62
	4c	50 Pt + 40 Ir + 10 Mn		
15% Disorder	4b	85 Mn + 15 Ir	6.42	14.32
	4c	50 Pt + 35 Ir + 15 Mn		
20% Disorder	4b	80 Mn + 0 Ir	7.45	21.08
	4c	50 Pt + 30 Ir + 20 Mn		

of MnPt<sub>0.5</sub>Ir<sub>0.5</sub>Sn, the refinement is carried out considering 10% atomic disorder between Mn/Ir atoms. Here, only the Mn atoms that occupy the 4b and 4c sites carry the magnetic moment.

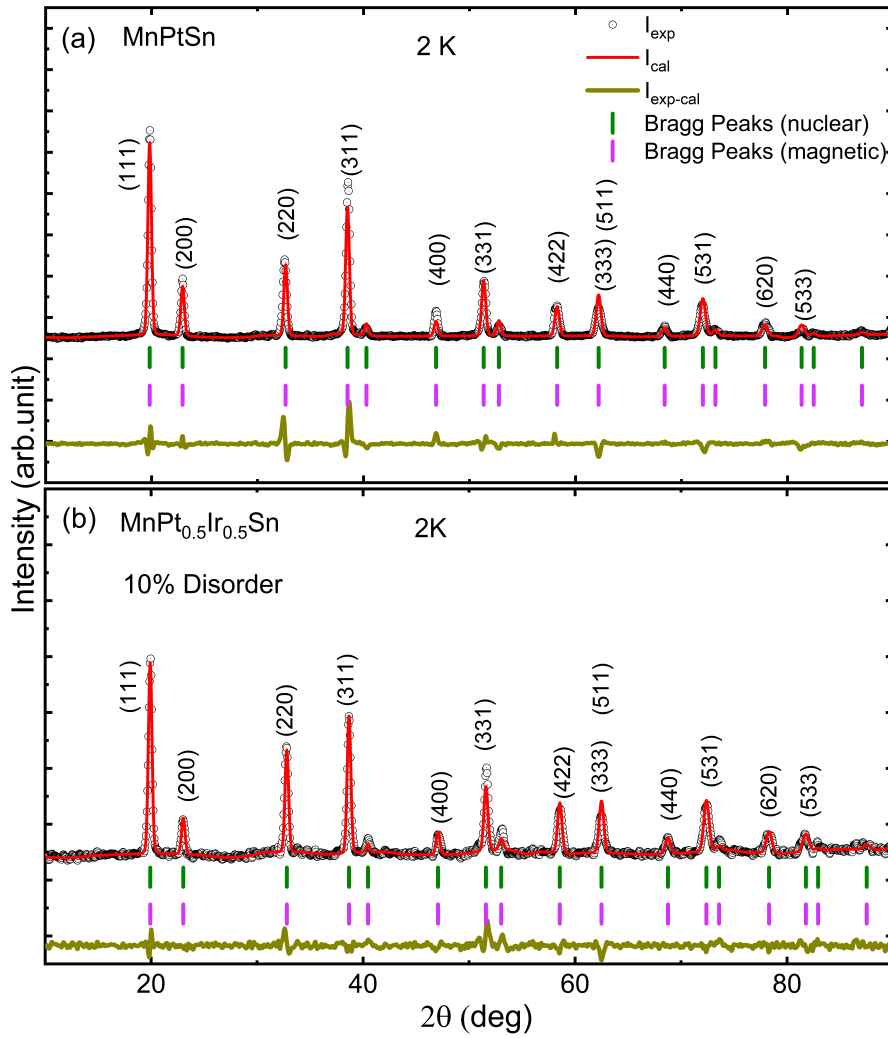


Figure 5.7: (a) Rietveld refinement of powder neutron diffraction (ND) patterns for MnPtSn collected at 2 K. (b) Rietveld refinement of powder ND pattern for MnPt<sub>0.5</sub>Ir<sub>0.5</sub>Sn collected at 2 K, with 10 % atomic disorder.

Initially, the refinement is carried out by taking into account the magnetic moments on both sites. The refined magnetic moment at the 4b site is found to be  $3.14 \mu_B$ , whereas a negligible moment is observed at the 4c site. The small moment at the 4c site is due to the presence of a small percentage of the Mn atom. Afterward, the refinement is carried out considering the moment only at the 4b site [structure is shown in Fig.5.6 (b)]. This time the magnetic moment is found to be  $3.17 \mu_B$ , which does not change the fitting parameters. The total moment comes to be about  $2.85 \mu_B/f.u.$ , which is consistent with the bulk magnetization measurement. Usually, in Heusler materials the magnetic atoms located at 4b and 4c sites exhibit

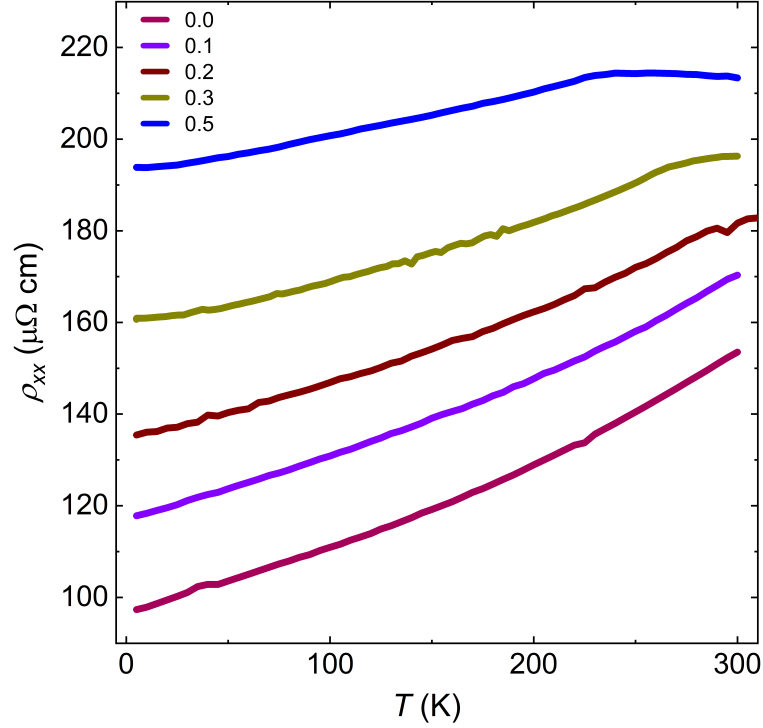


Figure 5.8: Temperature variation of longitudinal resistivity  $\rho_{xx}(T)$  for  $\text{MnPt}_{1-x}\text{Ir}_x\text{Sn}$ , with  $x=0, 0.1, 0.2, 0.3, 0.5$ .

antiferromagnetic alignment. Hence the magnetic moment in case of the Ir-doped sample decreases due to the presence of lower percentages of Mn atoms at the 4b site that antiferromagnetically align with the Mn atoms at the 4c site. The Rietveld refinement of the ND data established that the magnetic moment in the Ir-doped samples decreases due to the induced atomic disorder between Mn/Ir atom.

### 5.3 Electronic transport properties

To explore the effect of Ir doping on the electrical transport properties of the system, longitudinal and transverse resistivity data are measured for all the samples. The zero-field longitudinal resistivity data with the variation of temperature [ $\rho_{xx}(T)$ ] for all the samples are shown in Fig. 5.8. The resistivity decreases with decreasing the temperature, indicating the metallic nature for all the samples. With increasing Ir concentration, the conductivity ( $\sigma_{xx}$ ) decreases.

### 5.3.1 Hall resistivity

Both the magnetization and resistivity measurements indicate a substantial change in the physical properties of the system resulting from the introduction of Ir atoms. To further assess the effect of Ir doping in the system, a comprehensive investigation of electronic transport properties is conducted by measuring field-dependent transverse resistivity  $\rho_{xy}(H)$ . Figures 5.9 (a)-(e) depict the field variation of isothermal Hall resistivity taken at different temperatures for  $\text{MnPt}_{1-x}\text{Ir}_x\text{Sn}$ , with  $x=0, 0.1, 0.2, 0.3, 0.5$ . At the low field regime, the Hall resistivity increases linearly with the magnetic field and saturates at higher fields. The anomalous Hall resistivity  $\rho_{xy}^A$  has been determined using the zero-field extrapolation of the high field  $\rho_{xy}(H)$  data. The change in  $\rho_{xy}^A$  with Ir concentration measured at 5 K is shown in Fig. 5.9 (f). It is found that the  $\rho_{xy}^A$  enhances sharply with increasing the Ir concentration. The  $\rho_{xy}^A$  increases from  $1.62 \mu\Omega - cm$  for  $\text{MnPtSn}$  to  $5 \mu\Omega - cm$  for  $x = 0.5$  Ir-doped sample. From the magnetization and Hall resistivity measurements, it is found that with increasing the Ir concentration, the magnetic moment of the system reduces while the anomalous Hall resistivity increases [shown in 5.10 (a)]. Although there is an increment in anomalous Hall resistivity, the Hall conductivity  $\sigma_{xy}^A$  experiences a slight reduction, as shown in Fig 5.10 (b). The anomalous Hall angle (AHA), defined as  $(\frac{\sigma_{xy}^A}{\sigma_{xx}})$  is plotted in Fig. 5.10 (c). The AHA exhibits an increment with increasing the Ir concentration. The AHA signifies the percentage conversion of longitudinal current into a transverse one. In the present case, the amplification of AHA implies that the overall anomalous Hall effect increases with substituting Ir in place of Pt.

### 5.3.2 Scaling of anomalous Hall effect

To understand the origin of AHE in the present system, different contributions to the AHE are scrutinized using the universal scaling relation and power law fitting. The TYJ scaling relation equ. 1.30 is employed to disentangle different contributions of the AHE. Figures 5.11 (a)-(e) illustrate the plot of anomalous Hall resistivity ( $\rho_{xy}^A$ ) with the square of longitudinal resistivity ( $\rho_{xx}^2$ ) for all the samples. The  $\rho_{xy}^A$

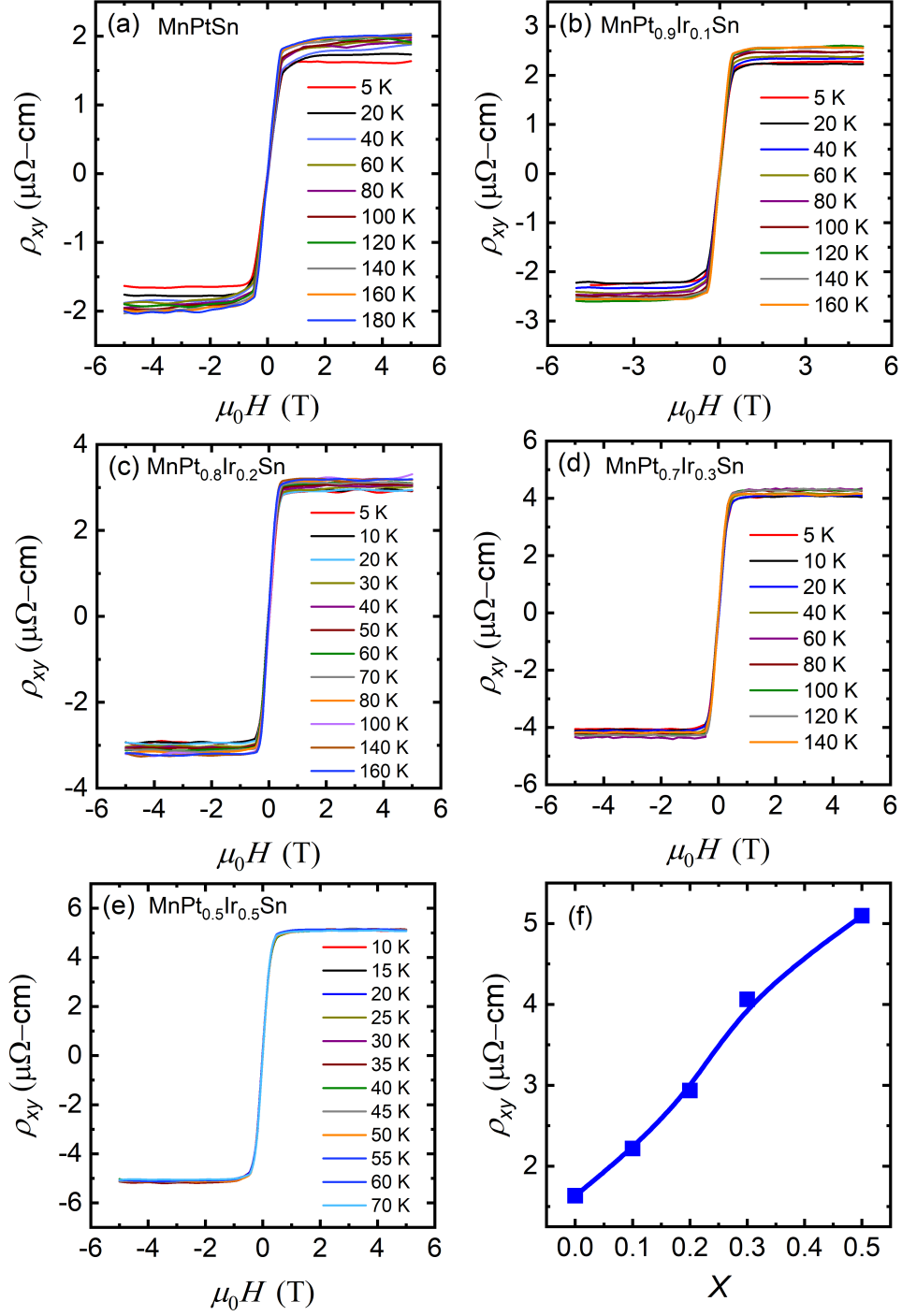


Figure 5.9: (a-e) The Hall resistivity as a function of magnetic field at different temperatures for  $\text{MnPt}_{1-x}\text{Ir}_x\text{Sn}$ , with  $x=0, 0.1, 0.2, 0.3, 0.5$ . (f) Plot of anomalous Hall resistivity ( $\rho_{xy}^A$ ) with Ir concentration at 5K .

data are acquired from the field-dependent Hall resistivity measurements at several temperatures and the corresponding  $\rho_{xx}^2$  data are collected from the temperature

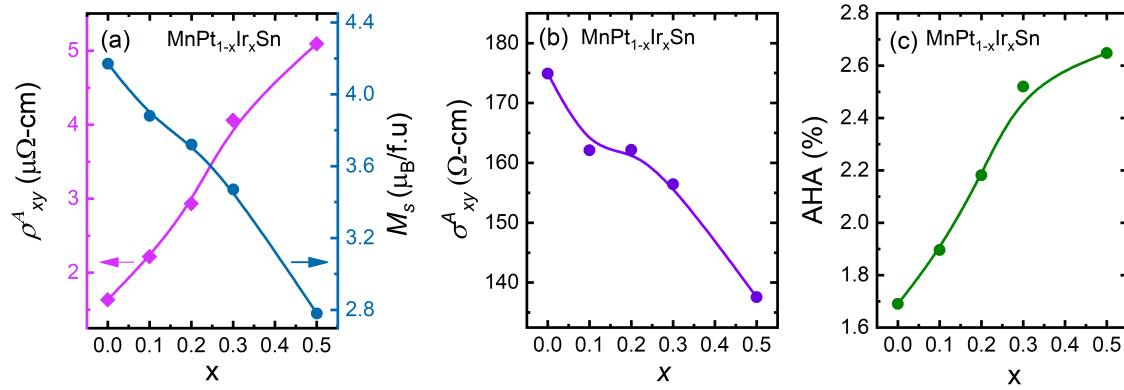


Figure 5.10: (a) Anomalous Hall resistivity ( $\rho_{xy}^A$ , magenta curve) and saturation magnetization at 5 K with Ir concentration. (b) Variation of anomalous Hall conductivity ( $\sigma_{xy}^A$ ) with Ir concentration at 5 K. (c) Plot of anomalous Hall angle (AHA) as a function of Ir percentage at 5 K.

dependent resistivity measurements. The filled circles represent the experimental data measured at different temperatures shown on the top axis. The extrinsic and intrinsic parameters are obtained by the linear fitting with the TYJ equation  $\rho_{xy}^A = a\rho_{xx0} + b\rho_{xx}^2$  (orange curve). The slope of the fitting gives the intrinsic parameter ‘b’ and the intercept at  $\rho_{xy}^A$  axis corresponds to the extrinsic contribution  $a\rho_{xx0}$ . From the known value of  $\rho_{xx0}$  the extrinsic parametric ‘a’ can be calculated. The variation of extrinsic ‘a’ and intrinsic parameter ‘b’ with Ir concentration are shown in Fig 5.11 (f). The intrinsic parameter ‘b’ increases whereas the extrinsic parameter ‘a’ decreases with increasing the Ir concentration. The scaling relation demonstrated that with increasing the Ir concentration leads to the strengthening of the intrinsic contribution, which enhances the total AHE. The extracted extrinsic contribution, intrinsic contribution, and total Hall resistivity are listed in Table 5.3.

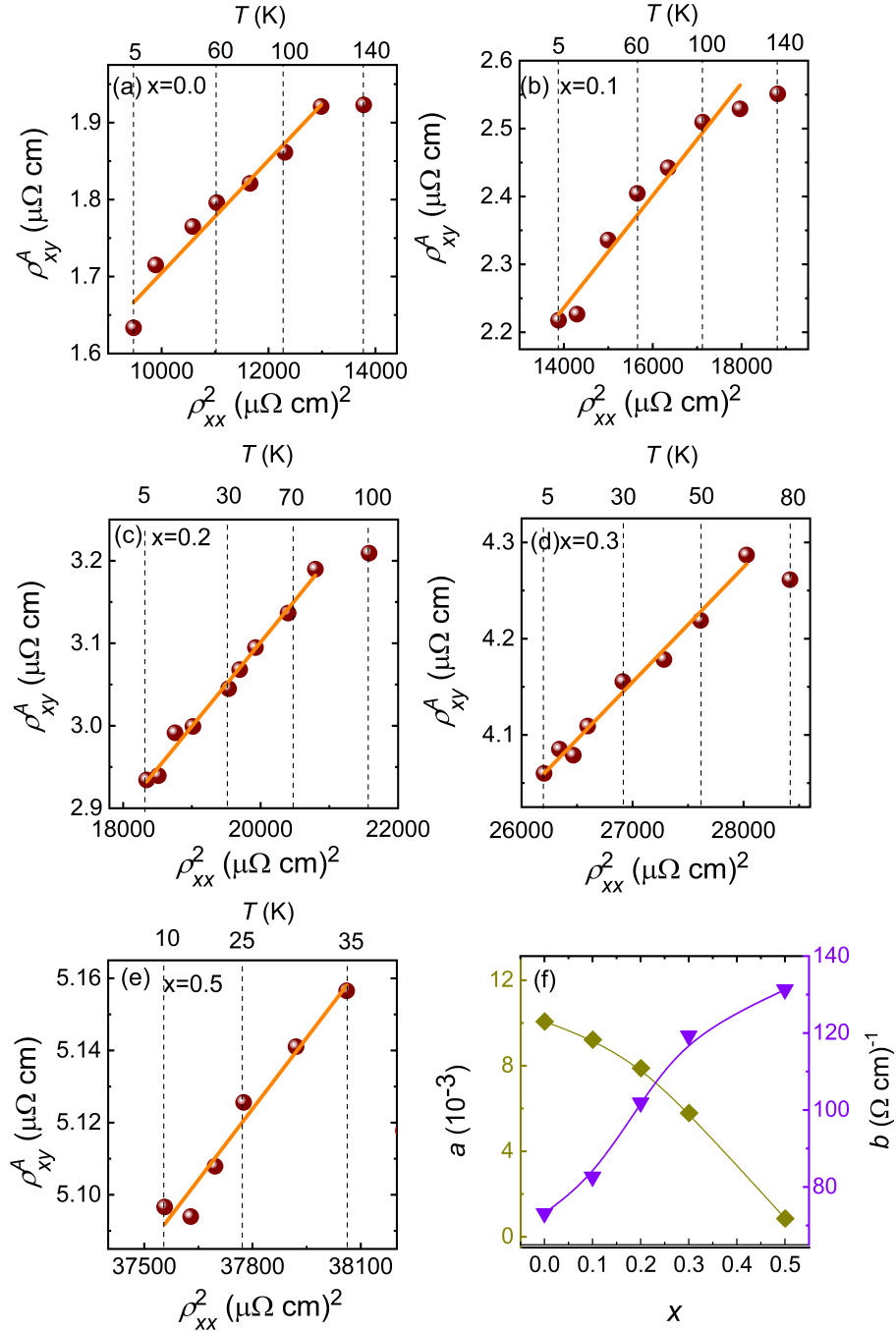


Figure 5.11: Scaling relation. (a-e) Plot of anomalous Hall resistivity ( $\rho_{xy}^A$ ) with square of longitudinal resistivity ( $\rho_{xx}^2$ ) for MnPt<sub>1-x</sub>Ir<sub>x</sub>Sn, with x= 0, 0.1, 0.2, 0.3, 0.5. The circular data points are the experimental data and the solid line is the linear fitting. Horizontal top axes illustrate the corresponding measurement temperatures. (f) The variation of extrinsic ‘a’ (square points) and intrinsic ‘b’ parameter (triangle points) with Ir concentration.

Table 5.3: Extracted values of extrinsic, intrinsic parameters, different contributions of AHE, and total Hall resistivity.

<b>x</b>	<b>a</b> $\times 10^{-3}$	<b>b</b> $(\Omega \text{ cm})^{-1}$	$\rho_{xy}^{ext}$	$\rho_{xy}^{int}$ $(\mu\Omega \text{ cm})$	$\rho_{xy}^{tot}$
0.0	10.07	73.14	0.97	0.68	1.65
0.1	9.22	82.60	1.07	1.13	2.20
0.2	7.89	101.9	1.06	1.84	2.90
0.3	5.79	119.3	0.93	3.09	4.02
0.5	0.856	131.1	0.16	4.86	5.02

Furthermore, the dominant mechanism of AHE for all the compounds are examined using the power law relation  $\rho_{xy}^A \propto \rho_{xx}^\alpha$ . The plots of  $\log \rho_{xy}^A$  vs  $\log \rho_{xx}$  is depicted in Figs. 5.12 (a)-(e). The solid orange curve is the linear fitting, and the slope gives the scaling factor  $\alpha$ . The change of  $\alpha$  with Ir concentration is shown in Fig. 5.11 (f). The scaling factor increases with increasing the Ir doping. The scaling factor  $\alpha$  for MnPtSn is 0.96, which signifies that the anomalous Hall effect in these compounds mainly originates from the extrinsic mechanism. The increment of  $\alpha$  for higher Ir-doped samples indicates the growth of intrinsic mechanism. In the case of MnPt<sub>0.5</sub>Ir<sub>0.5</sub>Sn, the value of  $\alpha$  is 1.93, suggesting the main contribution of AHE originates from the intrinsic mechanism.

In the present study, the side-jump contribution is neglected, whereas only the contribution of skew scattering to the extrinsic mechanism is considered. The side-jump contribution in bulk ferromagnetic materials is considered to be very small and can be estimated as  $\sigma_{xy}^{sj} \approx \frac{e^2}{ha} \left( \frac{\epsilon_{so}}{E_F} \right)$ , where  $\epsilon_{so}$  denotes the spin-orbit interaction energy,  $E_F$  represents the Fermi energy, and  $a$  stands for the lattice constant. For metallic ferromagnetic system  $\frac{\epsilon_{so}}{E_F} \approx 0.01$ . In the present case, the side-jump contribution is estimated using the above relation.

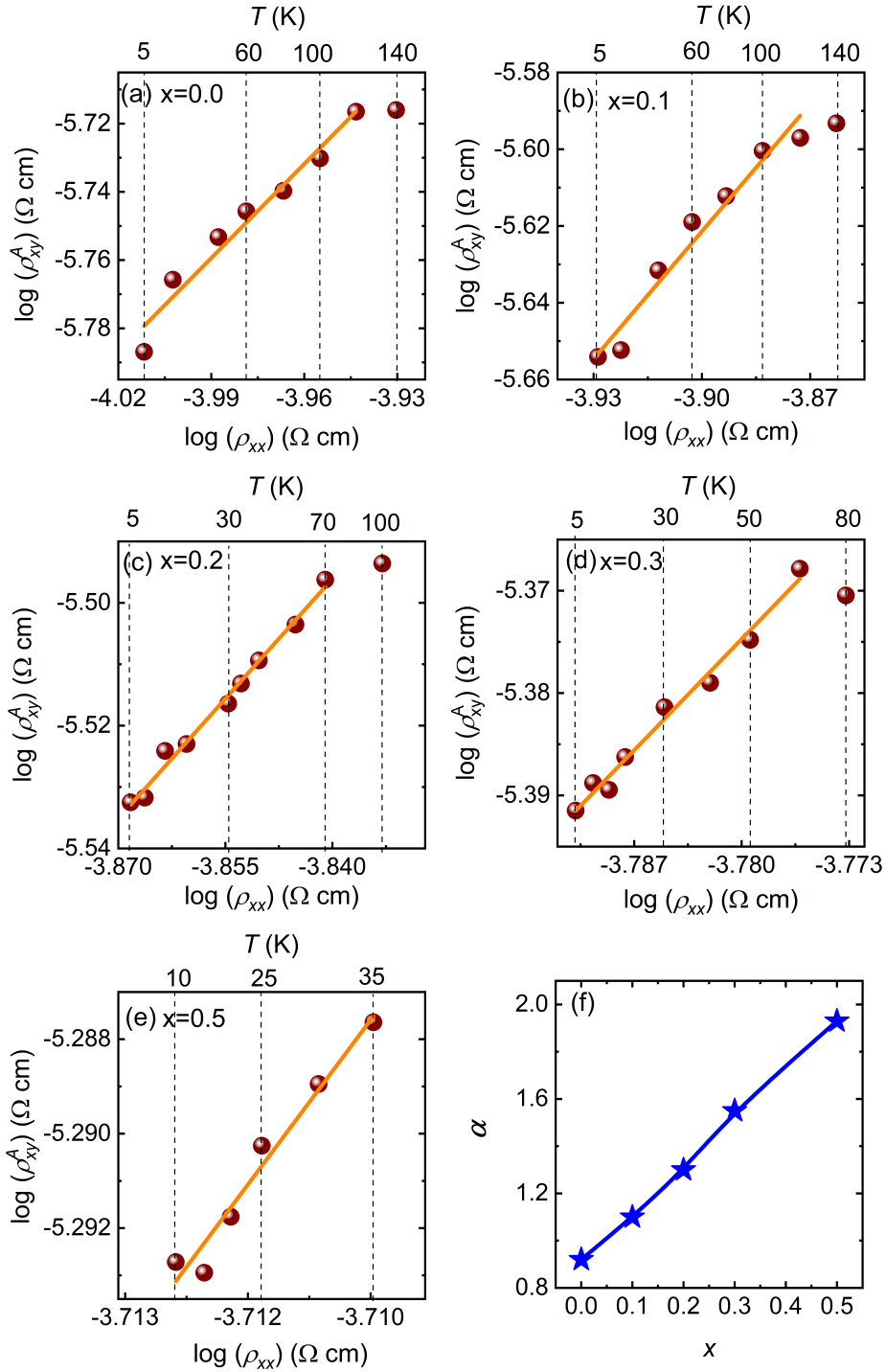


Figure 5.12: Power law fitting. (a)-(e) Plot of  $\log(\rho_{xy}^A)$  vs  $\log(\rho_{xx})$  for  $\text{MnPt}_{1-x}\text{Ir}_x\text{Sn}$ , with  $x=0, 0.1, 0.2, 0.3, 0.5$ . The circular points are the experimental data, and the solid line is the linear fitting. Horizontal top axes illustrate the corresponding measurement temperatures. (f) Variation of scaling factor  $\alpha$  with Ir concentration.

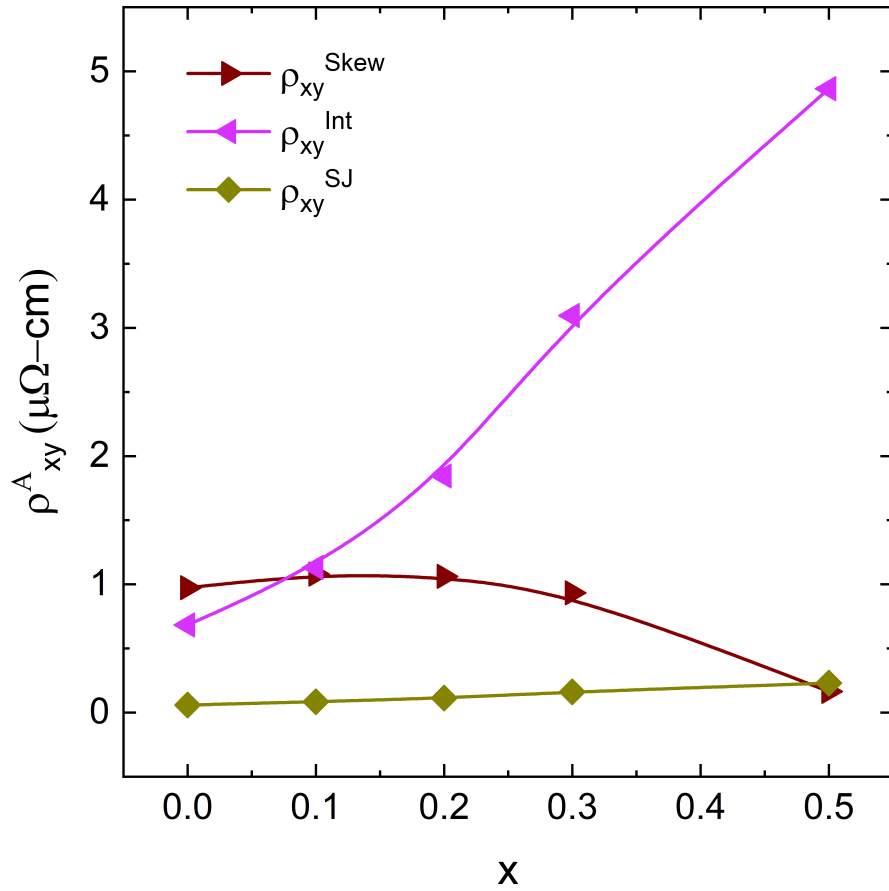


Figure 5.13: Different contributions of anomalous Hall effect as a function of Ir concentration for  $\text{MnPt}_{1-x}\text{Ir}_x\text{Sn}$ , with  $x=0, 0.1, 0.2, 0.3, 0.5$ . Left triangles represent the intrinsic contribution, right triangles represent the skew scattering contribution, and diamond symbols are used for the side jump contribution.

Figure 5.13 shows the variation of all three components of AHE with Ir concentration. The side-jump contribution is negligibly small in comparison to the dominant intrinsic or skew scattering mechanisms. For  $\text{MnPtSn}$ , the side-jump contribution is negligible compared to the extrinsic and intrinsic contributions. In the case of  $\text{MnPt}_{0.5}\text{Ir}_{0.5}\text{Sn}$ , side jump contribution is very small compared to the dominant intrinsic contribution. The comparable value of skew-scattering and side-jump contributions in this sample is due to the fact that the skew scattering contribution itself is very small for this compound. The main contribution in this compound stems from the intrinsic mechanism.

The reduction of the skew scattering contribution can be understood from the

fact that with Ir doping the longitudinal conductivity ( $\sigma_{xx}$ ) decreases. The extrinsic skew scattering contribution dominates in the clean limit and starts to decrease in the bad metallic regime. Thus as the conductivity decreases, the skew scattering starts to reduce. For the present study, with the increase of Ir concentration the conductivity decreases which decreases the skew scattering contribution.

The increase in the intrinsic contribution is understood using the theoretical calculation [please refer to the theoretical results of Phys. Rev. B 106, 184424 (2022)]. The electronic band structure calculations show that there are substantial changes occur in the density of states of Pt/Ir -5d states in the Ir-doped samples. Similar types of modification in the Pt/Ir -5d states happen with increasing the effective spin-orbit coupling (SOC). The variation of the calculated magnetic moment at the Mn site resembles the increase in Ir concentration and the spin-orbit coupling (SOC) strength. The effect of Ir doping is portrayed by calculating the magnetization density, where the spin isosurface at the Pt site for the MnPtSn gets modified when the effective SOC strength increases from 1 to 4. A Similar kind of spin isosurface at the Ir site is found in MnPt<sub>0.5</sub>Ir<sub>0.5</sub>Sn with the effective SOC strength 1. These findings suggest that with increasing the Ir concentration, the effective spin-orbit coupling (SOC) increases. The increment in the SOC enhances the Berry curvature [166], which in turn increases the intrinsic contribution in the present systems.

## 5.4 Summary

The present chapter discusses the enhancement of anomalous Hall effect and its manipulation in the Ir doped MnPtSn system. The magnetization measurements show that the Curie temperature and saturation magnetization decreases with increasing the Ir concentration. The decreases in the saturation magnetization is investigated by the neutron diffraction study. Rietveld refinement of neutron diffraction data reveal that substitution of Ir in place of Pt inherently induces an atomic disorder between Mn/Ir atoms, which reduces the magnetization. Despite the decrease in the magnetization there is a three fold increase in the anomalous Hall effect. The

increase in the anomalous Hall effect is examined using the scaling relation which indicates an growth of intrinsic contribution whereas the extrinsic contribution reduces significantly with increasing Ir concentration. The power law fitting shows that with increasing the Ir percentage the dominant mechanism of AHE becomes intrinsic in nature. A clear cross over from extrinsic to intrinsic mechanism is observed with Ir substitution. The present study demonstrates the manipulation of different mechanisms that governs the anomalous Hall effect.

# Chapter 6

## Summary and Future Aspects

The present thesis intends to investigate the non-trivial topological magnetic spin textures and electronic transport properties of some of the Mn-based Heusler materials. The primary motivation of this work is the rapid identification of non-trivial spin textures such as magnetic antiskyrmions, studying their stability, phase evolution under different external conditions, and exploiting the inter-correlation between magnetization and conduction electrons in the form of electronic transport properties. The thesis content starts with a brief discussion of various topological spin textures and their previous experimental observations using multiple techniques. Subsequently, the description of electronic transport phenomena and their correlation with the magnetic states are presented. In addition, the potential uses of Heusler materials are discussed. A separate chapter is dedicated to describing the experimental methods used in the present thesis. The main findings of the present thesis are summarized below.

In the first part of this thesis work, thermomagnetic response of topological magnetic states is utilized for a rapid identification of the antiskyrmion phase. In this context, bulk polycrystalline samples with composition  $\text{Mn}_{1.4}\text{PtSn}$ ,  $\text{Mn}_{1.4}\text{Pt}_{0.9}\text{Pd}_{0.1}\text{Sn}$ , and  $\text{Mn}_{1.1}\text{PtSn}$  are synthesized using the arc melting furnace. The assessment of phase purity and structural characterizations are conducted utilizing X-ray diffraction and scanning electron microscopy. Rietveld refinements of the X-ray diffrac-

tion patterns confirm the tetragonal crystal structure with space group  $I\bar{4}2m$  (No. 121) for  $Mn_{1.4}PtSn$  and  $Mn_{1.4}Pt_{0.9}Pd_{0.1}Sn$ , while the cubic structure is observed for  $Mn_{1.1}PtSn$  ( $F\bar{4}3m$  (No. 216)). The magnetic properties with the variation temperature and field are examined for all the three samples using SQUID-VSM. The magnetic ordering temperatures are found to be 395 K, 375 K, and 340 K for  $Mn_{1.4}PtSn$ ,  $Mn_{1.4}Pt_{0.9}Pd_{0.1}Sn$ , and  $Mn_{1.1}PtSn$ , respectively. In the tetragonal compounds, an additional spin reorientation transition is observed at lower temperatures. The existence of antiskyrmion phase in these samples is probed with the help of magneto-entropic signature. For this purpose, field variation of isothermal magnetization measurements are recorded at various temperatures for all three samples, and change in the magnetic entropy is calculated using Maxwell's relation. As expected, a negative magnetic entropy change occurs near the Curie temperature for all samples. For  $Mn_{1.4}PtSn$  and  $Mn_{1.4}Pt_{0.9}Pd_{0.1}Sn$ , a positive magnetic entropy change is found below the Curie temperature and persists up to the spin reorientation transition. In comparison, only negative magnetic entropy change is noticed for the cubic  $Mn_{1.1}PtSn$  sample in the whole magnetic ordering temperature. The positive magnetic entropy change is attributed to the formation of antiskyrmion phase. The antiskyrmion state is more disordered compared to the helical state. During the formation of antiskyrmion phase, the magnetic state transforms from a low magnetic entropic (helical phase) regime to a high entropic regime (antiskyrmion phase), leading to a positive magnetic entropy change. Furthermore, the AC susceptibility measurements are carried out to probe the antiskyrmion phase in these samples. The field variation of AC susceptibility data show peak/dip kind of anomalies in the case of  $Mn_{1.4}PtSn$  and  $Mn_{1.4}Pt_{0.9}Pd_{0.1}Sn$ . However, no such anomaly is found for the cubic  $Mn_{1.1}PtSn$  sample. The magnetic entropy change and AC susceptibility studies are used to draw temperature-field phase diagram for  $Mn_{1.4}PtSn$  and  $Mn_{1.4}Pt_{0.9}Pd_{0.1}Sn$ . The antiskyrmion phase is stabilized over a wide temperature field range and matches well with the reported phase diagrams constructed using real-space LTEM measurements. The observed negative magnetic entropy and absence of any anomaly in the AC susceptibility data for the  $Mn_{1.1}PtSn$

---

sample are well expected as the cubic symmetry does not favor the Dzyaloshinskii–Moriya interaction responsible to host antiskyrmions. Hence, in this sample the antiskyrmion phase is not stabilized below the Curie temperature. The magnetic entropy change and AC susceptibility study provide effective means of detecting the skyrmion/antiskyrmion phase even in the bulk limit over a wide temperature-field range.

The second part of the work focuses on studying the stability and phase evolution of antiskyrmions in a micron-size single crystalline Hall device. Topological antiskyrmion phase and non-topological magnetic states are detected in a single crystalline device of Mn-Ni-Ga system. The electron backscatter diffraction technique is used to map grains with single orientations in a polycrystalline  $\text{Mn}_{2.13}\text{Ni}_{0.87}\text{Ga}$  Heusler compound. Thin Hall devices of two different geometries (out-of-plane and in-plane) are fabricated from the single crystalline grain using Focused Ion Beam. In the case of out-of-plane device the surface is perpendicular to the  $c$ -axis and for the in-plane device the surface is normal to the  $ab$  plane. To verify the orientation of the Hall devices electron transparent transmission electron microscopy specimens are prepared in both the directions from the adjacent area of the Hall devices. The selected area electron diffraction patterns confirm the required orientation of the Hall devices. The Hall resistivity in the out-of-plane device geometry is measured by applying a magnetic field along the  $c$ -axis. In this orientation, a topological Hall signature is observed, confirming the presence of antiskyrmion phase in this system. The evolution of antiskyrmion state is studied by applying an oblique field with respect to the  $c$ -axis. The topological Hall signature decreases with increasing the inclination angle and vanishes at a tilting angle of  $80^\circ$ . At a higher tilting angle, the antiskyrmion phase gets stabilized in a narrow field range. The experimental observations are well supported by the micromagnetic simulation. The simulations are carried out with considering out-of-plane and in-plane field components equivalent to different tilting angles. Simulation results show that with increasing the tilting angle, antiskyrmion density decreases, and non-topological stripe domains appear. The existence of antiskyrmion phase at a large tilting angle demonstrates

the robustness of the antiskyrmion phase in the  $D_{2d}$  symmetric systems where the anisotropic Dzyaloshinskii–Moriya interaction plays the crucial role in stabilizing the antiskyrmion. In the case of the in-plane device, an aberrant hump-like feature in the Hall resistivity is observed. The origin of this hump-like feature is comprehended through minor loop Hall resistivity measurements. The presence of this feature is contingent on the history of field sweeps, affirming its non-topological origin of two-component anomalous Hall effect. The microstructure studies show that the presence of twin crystal structure in this direction gives two component anomalous Hall. In this study, the stability and existence of non-topological phases in  $D_{2d}$  symmetric system are illustrated.

In the third part, the microscopic electron transport mechanisms are studied by means of anomalous Hall effect. The enhancement of the anomalous Hall effect and the evolution of different mechanisms contributing to the AHE are elucidated. In pursuit of this objective, a series of  $\text{MnPt}_{1-x}\text{Ir}_x\text{Sn}$ , with  $x=0, 0.1, 0.2, 0.3, 0.5$  are synthesized by arc melting furnace. The structural and phase homogeneity of all the compounds are examined utilizing X-ray diffraction and scanning electron microscopy. The temperature and field variation of magnetization illustrate that with the substitution of Ir in place of Pt both the magnetic ordering temperature and the saturation magnetization decreases. Neutron diffraction measurements are conducted to comprehend the reduction of the magnetization. Rietveld refinement of the neutron diffraction data suggests that by introducing Ir in place of Pt, an atomic disorder arises between Mn/Ir atomic sites. The induced atomic disorder leads to a decrease in the magnetization. The field-dependent transverse resistivity data show a threefold increase in the Hall resistivity for the Ir doped sample compared to the undoped sample. The anomalous Hall angle rises with Ir concentration, affirming the enhancement of the anomalous Hall effect. The magnetization and Hall measurements indicate that the anomalous Hall that arises in these compounds do not depend on the sample magnetization as they show opposite behavior with Ir doping. The amplification of anomalous hall effect and the microscopic mechanisms are investigated using the scaling relation. Utilizing the scaling relation, scattering inde-

pendent intrinsic contributions and the scattering dependent extrinsic contributions are disentangled. The extracted contributions show that the intrinsic contribution increases considerably with increasing the Ir percentage, which magnifies the overall anomalous Hall effect. In comparison, the extrinsic contribution reduces with Ir doping. Further, the power law fitting exhibits the increase of the scaling factor from one to two with increasing the Ir doping. The increase of the scaling factor emphasizes the strengthening of the intrinsic mechanism. The reduction in the contribution from the extrinsic mechanism is related to the change of electrical conductivity by Ir doping, where the resistivity falls in the intrinsic contribution dominated bad metal regime. The enlargement of intrinsic mechanisms is understood with the help of theoretical calculations, which show that by introduction of Ir effectively increases the spin-orbit coupling, subsequently increasing the Berry curvature. Consequently, this leads to an increase in the scattering-independent intrinsic mechanism.

## Future Aspect

Recent interest in the applications of spintronics devices requires the detection of distinct magnetic spin-textures and a deeper understanding of electronic transport phenomena. In this direction, the present thesis work is in line with the current trends.

The first part of the thesis illustrates the identification of antiskyrmion phase using the magnetocaloric effect and AC susceptibility study. Antiskyrmion phase mapping with magneto-entropic signature and AC susceptibility study significantly contribute to the rapid discovery of non-trivial spin textures such as magnetic skyrmions/antiskyrmions. The change in the magnetic entropy and AC susceptibility investigation requires conventional DC magnetization measurements, which can be performed in a bulk limit sample over a wide temperature-field range. Therefore, these techniques allow a broader community to observe and study these topological magnetic states efficiently.

The second part of the thesis focuses on the antiskyrmion phase using topological

Hall effect measurements. Studying the antiskyrmion phase through the topological Hall effect enables one to detect the smaller size of magnetic skyrmions/antiskyrmions. It allows one to examine the emergent phenomena of the tiny magnetic textures. The topological Hall measurements with an oblique field depict the stability of the magnetic antiskyrmions in  $D_{2d}$  materials. The nature of the anisotropic Dzyaloshinskii–Moriya interaction present in these types of materials plays a crucial role in deciding the stability of the antiskyrmion phase. The present study significantly contributes toward the advancement of the fundamental understanding of antiskyrmion phase in the anisotropic Dzyaloshinskii–Moriya interaction based systems.

In the third section of this study, the manipulation of different mechanisms of anomalous Hall effect is showcased by chemical engineering. Specifically, the ability to enhance and tuning of extrinsic and intrinsic contributions with chemical substitution is demonstrated. This provides a crucial advancement in our understanding of the underlying principles governing microscopic transport phenomena, which holds promise for the development of anomalous Hall effect based spintronics devices. The enhancement of intrinsic mechanism and, at the same time, the decrease of extrinsic mechanisms with chemical substitution can be essential tools in the future to realize dissipationless transverse current.

# References

- [1] Ajaya K Nayak et al., *Nature*, **548**, 561–566 (2017).
- [2] Subir Sen et al., *Physical Review B*, **99**, 134404 (2019).
- [3] Subir Sen et al., *Physical Review Applied*, **17**, 044040 (2022).
- [4] Gordon E Moore, *IEEE solid-state circuits society newsletter*, **11**, 33–35 (2006).
- [5] M Mitchell Waldrop, *Nature News*, **530**, 144 (2016).
- [6] Igor Žutić, Jaroslav Fabian, and S Das Sarma, *Reviews of modern physics*, **76**, 323 (2004).
- [7] Albert Fert, *Reviews of modern physics*, **80**, 1517 (2008).
- [8] Dmitri E Nikonov and Ian A Young, *Proceedings of the IEEE*, **101**, 2498–2533 (2013).
- [9] Claude Chappert, Albert Fert, and Frédéric Nguyen Van Dau, *Nature materials*, **6**, 813–823 (2007).
- [10] Sasikanth Manipatruni, Dmitri E Nikonov, and Ian A Young, *Nature Physics*, **14**, 338–343 (2018).
- [11] Jongyeon Kim et al., *Proceedings of the IEEE*, **103**, 106–130 (2014).
- [12] Weisheng Zhao and Guillaume Prenat. *Spintronics-based computing*. Springer, 2015.

- 
- [13] Guillaume Prenat et al., *Spintronics-based Computing*, 145–157 (2015).
- [14] Mario Norberto Baibich et al., *Physical review letters*, **61**, 2472 (1988).
- [15] Grünberg Binasch et al., *Physical review B*, **39**, 4828 (1989).
- [16] Ching Tsang et al., *IEEE Transactions on Magnetism*, **30**, 3801–3806 (1994).
- [17] Ching H Tsang et al., *IBM journal of research and development*, **42**, 103–116 (1998).
- [18] Michel Julliere, *Physics letters A*, **54**, 225–226 (1975).
- [19] Jagadeesh Subbaiah Moodera et al., *Physical review letters*, **74**, 3273 (1995).
- [20] Ibrahim Ahmed et al., *IEEE Journal on Exploratory Solid-State Computational Devices and Circuits*, **3**, 74–82 (2017).
- [21] Luqiao Liu et al., *Science*, **336**, 555–558 (2012).
- [22] Ioan Mihai Miron et al., *Nature*, **476**, 189–193 (2011).
- [23] Stuart SP Parkin, Masamitsu Hayashi, and Luc Thomas, *Science*, **320**, 190–194 (2008).
- [24] Stuart Parkin and See-Hun Yang, *Nature nanotechnology*, **10**, 195–198 (2015).
- [25] Sebastian Mühlbauer et al., *Science*, **323**, 915–919 (2009).
- [26] XZ Yu et al., *Nature*, **465**, 901–904 (2010).
- [27] XZ Yu et al., *Nature materials*, **10**, 106–109 (2011).
- [28] Florian Jonietz et al., *Science*, **330**, 1648–1651 (2010).
- [29] XZ Yu et al., *Nature communications*, **3**, 988 (2012).
- [30] Albert Fert, Vincent Cros, and Joao Sampaio, *Nature nanotechnology*, **8**, 152–156 (2013).
- [31] Börge Göbel et al., *Scientific reports*, **9**, 12119 (2019).

- 
- [32] SA Wolf et al., *science*, **294**, 1488–1495 (2001).
- [33] Yiou Zhang, Qiang Hao, and Gang Xiao, *Sensors*, **19**, 3537 (2019).
- [34] Tomohiro Taniguchi, Julie Grollier, and Mark D Stiles, *Physical Review Applied*, **3**, 044001 (2015).
- [35] Chi Sun et al., *Physical Review Applied*, **12**, 034022 (2019).
- [36] Kentaro Nomura and Daichi Kurebayashi, *Physical review letters*, **115**, 127201 (2015).
- [37] Daichi Kurebayashi, Yasufumi Araki, and Kentaro Nomura, *journal of the physical society of japan*, **90**, 084702 (2021).
- [38] Igor Dzyaloshinsky, *Journal of physics and chemistry of solids*, **4**, 241–255 (1958).
- [39] Tôru Moriya, *Physical review*, **120**, 91 (1960).
- [40] Mathias Getzlaff. *Fundamentals of magnetism*. Springer Science & Business Media, 2007.
- [41] B Lebech, J Bernhard, and T Freltoft, *Journal of Physics: Condensed Matter*, **1**, 6105 (1989).
- [42] S Ishiwata et al., *Physical Review B*, **84**, 054427 (2011).
- [43] M Deutsch et al., *Physical Review B*, **90**, 144401 (2014).
- [44] Longmeng Xu et al., *Physical Review B*, **105**, 075108 (2022).
- [45] Matthias Bode et al., *nature*, **447**, 190–193 (2007).
- [46] P Ferriani et al., *Physical review letters*, **101**, 027201 (2008).
- [47] Stefan Heinze et al., *nature physics*, **7**, 713–718 (2011).
- [48] Niklas Romming et al., *Science*, **341**, 636–639 (2013).
- [49] Seonghoon Woo et al., *Nature materials*, **15**, 501–506 (2016).

- 
- [50] István Kézsmárki et al., *Nature materials*, **14**, 1116–1122 (2015).
- [51] Abhay K Srivastava et al., *Advanced Materials*, **32**, 1904327 (2020).
- [52] Rana Saha et al., *Nature Communications*, **13**, 3965 (2022).
- [53] S Di Napoli et al., *Physical Review B*, **70**, 174418 (2004).
- [54] Shinichiro Seki et al., *Science*, **336**, 198–201 (2012).
- [55] Tony Hilton Royle Skyrme, *Nuclear Physics*, **31**, 556–569 (1962).
- [56] Alexei N Bogdanov and DA Yablonskii, *Zh. Eksp. Teor. Fiz*, **95**, 178 (1989).
- [57] Kosuke Karube et al., *Nature Materials*, **20**, 335–340 (2021).
- [58] Naoto Nagaosa and Yoshinori Tokura, *Nature nanotechnology*, **8**, 899–911 (2013).
- [59] W Münzer et al., *Physical Review B*, **81**, 041203 (2010).
- [60] Tianping Ma et al., *Advanced Materials*, **32**, 2002043 (2020).
- [61] AS Sukhanov et al., *Physical Review B*, **106**, L140402 (2022).
- [62] Jagannath Jena et al., *Nano letters*, **20**, 59–65 (2019).
- [63] Ankit K Sharma et al., *Advanced Materials*, **33**, 2101323 (2021).
- [64] Siying Huang et al., *Physical Review B*, **96**, 144412 (2017).
- [65] XZ Yu et al., *Nature*, **465**, 901–904 (2010).
- [66] Toshiaki Tanigaki et al., *Nano letters*, **15**, 5438–5442 (2015).
- [67] XZ Yu et al., *Nature*, **564**, 95–98 (2018).
- [68] Wanjun Jiang et al., *Science*, **349**, 283–286 (2015).
- [69] Anjan Soumyanarayanan et al., *Nature materials*, **16**, 898–904 (2017).
- [70] Shawn D Pollard et al., *Nature communications*, **8**, 14761 (2017).
- [71] Gong Chen, Arantzazu Mascarague, Andreas K Schmid, et al., *Applied Physics Letters*, **106**, (2015).

- 
- [72] Emil Warburg, *Annalen der Physik*, **249**, 141–164 (1881).
- [73] Pierre Weiss and Auguste Piccard, *J. Phys. Theor. Appl.*, **7**, 103–109 (1917).
- [74] Edwin H Hall et al., *American Journal of Mathematics*, **2**, 287–292 (1879).
- [75] Edwin Herbert Hall, *The London, Edinburgh, and Dublin Philosophical Magazine and Journal of Science*, **12**, 157–172 (1881).
- [76] Robert Karplus and JM Luttinger, *Physical Review*, **95**, 1154 (1954).
- [77] T Jungwirth, Qian Niu, and AH MacDonald, *Physical review letters*, **88**, 207208 (2002).
- [78] Masaru Onoda and Naoto Nagaosa, *Physical review letters*, **90**, 206601 (2003).
- [79] Satoru Nakatsuji, Naoki Kiyohara, and Tomoya Higo, *Nature*, **527**, 212–215 (2015).
- [80] Ajaya K Nayak et al., *Science advances*, **2**, e1501870 (2016).
- [81] Yugui Yao et al., *Physical review letters*, **92**, 037204 (2004).
- [82] Qi Wang et al., *Nature communications*, **9**, 3681 (2018).
- [83] Yao Zhang et al., *npj Quantum Materials*, **6**, 17 (2021).
- [84] Peigang Li et al., *Nature communications*, **11**, 3476 (2020).
- [85] J Smit, *Physica*, **21**, 877–887 (1955).
- [86] Yuki Shiomi, Y Onose, and Y Tokura, *Physical Review B*, **79**, 100404 (2009).
- [87] Yukako Fujishiro et al., *Nature communications*, **12**, 317 (2021).
- [88] Q Zhang et al., *Physical Review B*, **94**, 024428 (2016).
- [89] Yao Zhang et al., *npj Quantum Materials*, **6**, 17 (2021).
- [90] Shigeki Onoda, Naoyuki Sugimoto, and Naoto Nagaosa, *Physical review letters*, **97**, 126602 (2006).

- 
- [91] Naoto Nagaosa et al., *Reviews of modern physics*, **82**, 1539 (2010).
- [92] Yuan Tian, Li Ye, and Xiaofeng Jin, *Physical review letters*, **103**, 087206 (2009).
- [93] LJ Zhu, D Pan, and JH Zhao, *Physical Review B*, **89**, 220406 (2014).
- [94] Dmitriy Yu Karpenkov et al., *Physical Review B*, **100**, 094445 (2019).
- [95] KK Meng et al., *Physical Review B*, **100**, 184410 (2019).
- [96] Jianlei Shen et al., *Physical Review Letters*, **125**, 086602 (2020).
- [97] A Neubauer et al., *Physical review letters*, **102**, 186602 (2009).
- [98] T Yokouchi et al., *Physical Review B*, **89**, 064416 (2014).
- [99] Friedrich Heusler, *Verhandlungen der Deutschen Physikalischen Gesellschaft*, **5**, 219 (1903).
- [100] F Heusler, W Starck, and E Haupt. *Verh. DPG, vol. 5*. 1903.
- [101] Tanja Graf, Claudia Felser, and Stuart SP Parkin, *Progress in solid state chemistry*, **39**, 1–50 (2011).
- [102] Elizabeth Decolvenaere et al., *Physical Review B*, **96**, 165109 (2017).
- [103] Sean D Harrington et al., *Physical Review Materials*, **2**, 014406 (2018).
- [104] PJ Webster and KRA Ziebeck, *Alloys and Compounds of d-Elements with Main Group Elements. Part 2*, 75–79 (1988).
- [105] Otto Heusler, *Annalen der Physik*, **411**, 155–201 (1934).
- [106] Vajiheh Alijani et al., *Journal of Physics: Condensed Matter*, **24**, 046001 (2012).
- [107] Xuefang Dai et al., *Solid state communications*, **140**, 533–537 (2006).
- [108] N Lakshmi, Anil Pandey, and K Venugopalan, *Bulletin of Materials Science*, **25**, 309–313 (2002).

- 
- [109] WY Zhang et al., *Journal of Magnetism and Magnetic Materials*, **537**, 168157 (2021).
- [110] Anil Aryal et al., *Journal of Alloys and Compounds*, **823**, 153770 (2020).
- [111] GE Bacon and JS Plant, *Journal of Physics F: Metal Physics*, **1**, 524 (1971).
- [112] C Jiang, M Venkatesan, and JMD Coey, *Solid state communications*, **118**, 513–516 (2001).
- [113] Johannes Kroder et al., *Physical Review B*, **99**, 174410 (2019).
- [114] Madhusmita Baral et al., *Journal of Magnetism and Magnetic Materials*, **475**, 675–682 (2019).
- [115] PJ Webster et al., *Philosophical Magazine B*, **49**, 295–310 (1984).
- [116] Ghazal Tadayyon et al., *Materials Characterization*, **125**, 51–66 (2017).
- [117] SP Venkateswaran, NT Nuhfer, and M De Graef, *Acta materialia*, **55**, 5419–5427 (2007).
- [118] X Liu et al., *Scientific reports*, **8**, 1–9 (2018).
- [119] Yanling Ge et al., *Journal of Applied Physics*, **96**, 2159–2163 (2004).
- [120] Davide Betto et al., *Physical Review B*, **91**, 094410 (2015).
- [121] Max Hirschberger et al., *Nature materials*, **15**, 1161–1165 (2016).
- [122] J Kübler, *Physica B+ C*, **127**, 257–263 (1984).
- [123] Lukas Wollmann et al., *Physical Review B*, **90**, 214420 (2014).
- [124] Olga Meshcheriakova et al., *Physical review letters*, **113**, 087203 (2014).
- [125] E Şaşıoğlu, LM Sandratskii, and P Bruno, *Physical Review B*, **77**, 064417 (2008).
- [126] KEHM Hanssen and PE Mijnders, *Physical Review B*, **34**, 5009 (1986).
- [127] GL Bona et al., *Solid state communications*, **56**, 391–394 (1985).

- 
- [128] SK Clowes et al., *Physical Review B*, **69**, 214425 (2004).
- [129] WR Branford et al., *Journal of Magnetism and Magnetic Materials*, **272**, E1399–E1401 (2004).
- [130] Feng Wu et al., *Applied Physics Letters*, **94**, (2009).
- [131] Clemens Schindler et al., *Physical Review B*, **101**, 125119 (2020).
- [132] Kaustuv Manna et al., *Nature Reviews Materials*, **3**, 244–256 (2018).
- [133] Satya N Guin et al., *NPG Asia Materials*, **11**, 16 (2019).
- [134] CE Ekuma et al., *Physical Chemistry Chemical Physics*, **23**, 11876–11885 (2021).
- [135] SJ Youn and BI Min, *Physical Review B*, **51**, 10436 (1995).
- [136] Daigo Shimizu et al., *ACS Applied Nano Materials*, **5**, 13519–13528 (2022).
- [137] W Akhtar et al., *Physical Review Applied*, **11**, 034066 (2019).
- [138] MN Potkina et al., *Physical Review B*, **102**, 134430 (2020).
- [139] N Kanazawa et al., *Physical Review B*, **91**, 041122 (2015).
- [140] Jagannath Jena et al., *Science Advances*, **6**, eabc0723 (2020).
- [141] Rana Saha et al., *Nature communications*, **10**, 5305 (2019).
- [142] GD Liu et al., *Physical Review B*, **74**, 054435 (2006).
- [143] Ajaya K Nayak et al., *Nature materials*, **14**, 679–684 (2015).
- [144] Avia Noah et al., *Physical Review B*, **105**, 144423 (2022).
- [145] Yangkun He et al., *Acta Materialia*, **226**, 117619 (2022).
- [146] Shi-Zeng Lin and Avadh Saxena, *Physical Review B*, **92**, 180401 (2015).
- [147] AO Leonov and István Kézsmárki, *Physical Review B*, **96**, 214413 (2017).
- [148] Moritz Winter et al., *Communications Materials*, **3**, 102 (2022).

- 
- [149] Daisuke Kan et al., *Physical Review B*, **98**, 180408 (2018).
- [150] Lorenzo Vistoli et al., *Nature Physics*, **15**, 67–72 (2019).
- [151] Alexander Gerber, *Physical Review B*, **98**, 214440 (2018).
- [152] Ting Fu et al., *Physical Review B*, **103**, 064432 (2021).
- [153] Yao Zhang and Simon Granville, *Physical Review B*, **106**, 144414 (2022).
- [154] Graham Kimbell et al., *Communications Materials*, **3**, 19 (2022).
- [155] Lixuan Tai et al., *ACS nano*, **16**, 17336–17346 (2022).
- [156] Andreas Neudert et al., *Advanced Engineering Materials*, **14**, 601–613 (2012).
- [157] Anett Diestel et al., *Journal of Physics: Condensed Matter*, **25**, 266002 (2013).
- [158] O Perevertov, O Heczko, and R Schäfer, *Physical Review B*, **95**, 144431 (2017).
- [159] Michael Joseph Donahue and Donald G Porter. *OOMMF user’s guide, version 1.0*. 1999.
- [160] Akira Matsui, Takuya Nomoto, and Ryotaro Arita, *Physical Review B*, **104**, 174432 (2021).
- [161] Su Do Yi et al., *Physical Review B*, **80**, 054416 (2009).
- [162] Jonathan Gaudet et al., *Nature materials*, **20**, 1650–1656 (2021).
- [163] Yoshihiro D Kato et al., *Nature Communications*, **14**, 5416 (2023).
- [164] Juan Rodríguez-Carvajal, *Physica B: Condensed Matter*, **192**, 55–69 (1993).
- [165] AK Nayak et al., *Physical Review B*, **90**, 220408 (2014).
- [166] Di Xiao, Ming-Che Chang, and Qian Niu, *Reviews of modern physics*, **82**, 1959 (2010).